

AD-A107 201

AIR FORCE INST OF TECH WRIGHT-PATTERSON AFB OH SCHOO--ETC F/G 20/4  
PREDICTION OF AERODYNAMIC FORCES ON A CIRCULAR CYLINDER AND A T--ETC(U)  
JUN 79 J E MARSH

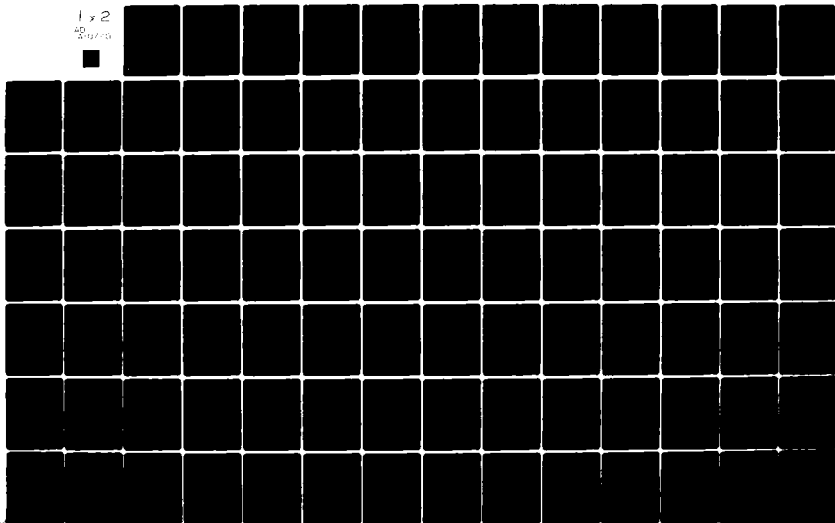
UNCLASSIFIED

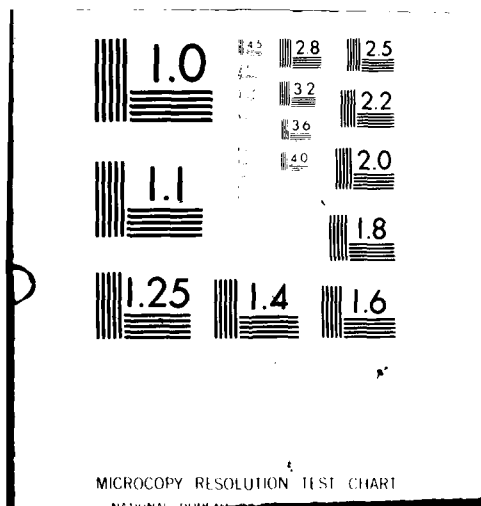
AFIT/DS/AA/79M-1

AFIT-CI-79-216D

NL

1 x 2  
20/4





REPORT DOCUMENTATION PAGE		READ INSTRUCTIONS BEFORE COMPLETING FORM
1. REPORT NUMBER 79-216D	2. GOVT ACCESSION NO. AD-A107201	3. RECIPIENT'S CATALOG NUMBER
4. TITLE (and Subtitle) Prediction of Aerodynamic Forces of a Circular Cylinder and a Thin Airfoil in a Transonic Airstream by the Finite Element Method.		5. TYPE OF REPORT & PERIOD COVERED THESIS/DISSERTATION
7. AUTHOR(s) Captain James E. Marsh		6. PERFORMING ORG. REPORT NUMBER
9. PERFORMING ORGANIZATION NAME AND ADDRESS AFIT STUDENT AT: School of Engineering, AFIT		8. CONTRACT OR GRANT NUMBER(s)
11. CONTROLLING OFFICE NAME AND ADDRESS AFIT/NR WPAFB OH 45433		10. PROGRAM ELEMENT, PROJECT, TASK AREA & WORK UNIT NUMBERS
14. MONITORING AGENCY NAME & ADDRESS (if different from Controlling Office) AFIT DCI-79-216D		12. REPORT DATE 5 June 1979
15. SECURITY CLASS. (of this report) UNCLASS		13. NUMBER OF PAGES 171
16. DISTRIBUTION STATEMENT (of this Report) APPROVED FOR PUBLIC RELEASE; DISTRIBUTION UNLIMITED AFIT/DS/AA/79M-1		15a. DECLASSIFICATION/DOWNGRADING SCHEDULE
17. DISTRIBUTION STATEMENT (of the abstract entered in Block 20, if different from Report) 22 OCT 1981		DTIC ELECTE NOV 6 1981
18. SUPPLEMENTARY NOTES APPROVED FOR PUBLIC RELEASE: IAW AFR 190-17		H Fredric C. Lynch FOR THE CLINTON, Major, USAF Director of Plans & Admin AFIT/DS/AA/79M-1
19. KEY WORDS (Continue on reverse side if necessary and identify by block number)		
20. ABSTRACT (Continue on reverse side if necessary and identify by block number) ATTACHED		

AD A107201

DTIC FILE COPY

AFIT/DS/AA/79M-1

PREDICTION OF AERODYNAMIC FORCES  
ON A CIRCULAR CYLINDER AND A THIN  
AIRFOIL IN A TRANSONIC AIRSTREAM  
BY THE FINITE ELEMENT METHOD

DISSERTATION

Presented to the Faculty of the School of Engineering  
of the Air Force Institute of Technology  
Air University  
in Partial Fulfillment of the  
Requirements for the Degree of  
Doctor of Philosophy

by

James E. Marsh, B.S., M.S.

Captain

USAF

Approved for public release; distribution unlimited

AFIT/DS/AA/79M-1

PREDICTION OF AERODYNAMIC FORCES  
ON A CIRCULAR CYLINDER AND A THIN  
AIRFOIL IN A TRANSONIC AIRSTREAM  
BY THE FINITE ELEMENT METHOD

by

James E. Marsh, B.S., M.S.

Captain

USAF

Approved:

<u>Franklin Elstner</u> Chairman	<u>27 Apr 79</u>
<u>John R. Shea, Jr.</u>	<u>3 May 79</u>
<u>Stephen J. Koob</u>	<u>10 May 79</u>
<u>John Louis Jr.</u>	<u>7 May 79</u>
<u>David D. Hardin</u>	<u>21 May 79</u>

Accepted:

<u>J. S. Premianicki</u> Dean, School of Engineering	<u>5 June 79</u>
---	------------------

### Acknowledgments

I would like to express my gratitude to Professor Franklin E. Eastep for suggesting a topic which proved to be interesting and self motivating, for convincing me to pursue the topic in spite of my doubts about being able to solve the mixed (transonic) problem by the finite element method, and most of all for giving his devoted guidance and support during the course of this study. Thanks goes to Professors John Jones, Stephen Koob, and John Shea for their valuable suggestions and interest in the topic. Thanks also goes to Dr. James Olson of the Air Force Flight Dynamics Laboratory for sponsoring the study and supplying computer resources.

I especially want to express my deepest appreciation to my wife, Retta, and two sons, Derrick and Darren, for their loving support and encouragement. A special thanks to Shirley McCumber, my sister, for spending her weekends and evenings typing this report.

James E. Marsh

## Contents

	Page
Acknowledgments . . . . .	ii
List of Figures . . . . .	vi
List of Tables . . . . .	ix
Abstract . . . . .	x
I. Introduction . . . . .	1
Previous and Recent Works. . . . .	2
Objective. . . . .	6
The Finite Element Method (Background) . . . . .	8
II. Problem Description . . . . .	10
Circular Cylinder/Incompressible Flows . . . . .	10
Thin Airfoil . . . . .	14
Circular Cylinder/Compressible Flow. . . . .	18
III. Analysis of the Cylinder Problem. . . . .	20
Flowfield Discretization . . . . .	20
Incompressible Flow. . . . .	21
Superposition . . . . .	21
Finite Element Solution . . . . .	26
Trial Functions . . . . .	29
Symmetric Flow. . . . .	29
Flow With Circulation . . . . .	31
Compressible Symmetric Flow. . . . .	32
IV. Analysis of Flow Over a Thin Airfoil . . . . .	36
Flowfield Discretization . . . . .	36
Iterative Approximation. . . . .	39
Finite Element Solution. . . . .	40
Mixed Flow . . . . .	44
Reported Convergence Difficulties . . . . .	44
Formulation Adjustments . . . . .	45
New Upwinding Technique . . . . .	48

V.	Results of Flow Over a Circular Cylinder. . . . .	53
	Incompressible Flow Without Circulation. . . . .	53
	Geometry. . . . .	53
	Comparison of Three Sector Elements . . . . .	54
	Discretization Effects. . . . .	56
	Incompressible Flow With Circulation . . . . .	62
	Compressible Flow . . . . .	65
VI.	Results of Flow Over Nonlifting Airfoils. . . . .	73
	Discretization Effects . . . . .	73
	Farfield Boundary Location. . . . .	74
	Farfield Boundary Conditions. . . . .	78
	Element Refinement. . . . .	83
	Incompressible Results . . . . .	89
	Compressible Subsonic Results. . . . .	93
	Convergence of Iterative Scheme . . . . .	93
	Comparison of Results . . . . .	95
	Transonic Flow . . . . .	101
	Iterative Behavior of Solution Scheme . . . . .	101
	Upwinding Techniques. . . . .	104
	Comparison of Results . . . . .	112
VII.	Summary, Conclusions and Recommendations. . . . .	124
	Circular Cylinder. . . . .	124
	Thin Airfoil . . . . .	126
	Recommendations for Future Work. . . . .	129
	Problem Formulations. . . . .	129
	Higher Order Elements . . . . .	131
	Boundary Conditions . . . . .	131
	Arbitrary Thin Airfoil Shapes . . . . .	132
	New Elements. . . . .	132
	Shock Elements. . . . .	133
	Singularities . . . . .	133
	Unsteady Analysis . . . . .	134
	Bibliography. . . . .	135
Appendix A:	Shape Functions and Elemental Equations for Sector Element (1) . . . . .	140
	Shape Functions . . . . .	140
	Elemental Equations . . . . .	144
	Velocity Distribution . . . . .	148
Appendix B:	Shape Functions and Elemental Equations for Sector Element (2) . . . . .	149



Shape Functions . . . . .	149
Elemental Equations . . . . .	150
Velocity Distribution . . . . .	152
Appendix C: Shape Functions and Elemental Equations for Sector Element (3) . . . . .	153
Shape Functions . . . . .	153
Elemental Equations . . . . .	153
Incompressible Flow. . . . .	153
Compressible Flow. . . . .	156
Velocity Distribution . . . . .	161
Appendix D: Finite Element Equations for Flow Over an Airfoil for a Bilinear Rectangular Element. . . . .	162
Shape Functions . . . . .	162
Elemental Equations . . . . .	162
Pressure Distribution . . . . .	169
Mach Number . . . . .	170
Vita. . . . .	171

## List of Figures

Figure		Page
1	Flowfield for the Circular Cylinder. . . . .	11
2	Flowfield for the Airfoil. . . . .	15
3	Sector Element Geometry. . . . .	22
4	Discretization of Flowfield for Flow Over a Circular Cylinder without Circulation. . . . .	23
5	Discretization of Flowfield for Flow Over a Circular Cylinder with Circulation . . . . .	24
6	Initial Flowfield Discretization for Flow Over a Symmetric Nonlifting Airfoil. . . . .	38
7	Comparison of Tangential Velocity Distributions for Incompressible Flow Over a Circular Cylinder . . . .	55
8	Convergence of Tangential Velocity for Sector Element (2) for Refinement of $\beta$ Alone . . . . .	57
9	Convergence of Tangential Velocity for Sector Element (3) for Refinement of $\beta$ Alone . . . . .	58
10a	Perturbation Velocity Distribution from Sector Element (2) for Discretization (2), Table IV . . . . .	66
10b	Perturbation Velocity Distribution from Sector Element (3) for Discretization (2), Table IV . . . . .	67
11a	Perturbation Velocity Distribution from Sector Element (2) for Discretization (3), Table IV . . . . .	68
11b	Perturbation Velocity Distribution from Sector Element (3) for Discretization (3), Table IV . . . . .	69
12	Tangential Velocity Distribution on the Cylinder Surface Without Circulation (Compressible Flow). . . . .	72
13	Typical Discretization of Flowfield for Flow Over a Symmetric Nonlifting Airfoil . . . . .	75
14	Farfield Boundary Location Effects for $Y_{\max} = 1.5$ . . .	76
15	Farfield Boundary Location Effects for $X_{\max} = 1.5$ . . .	77
16	Convergence Behavior of $C_p$ (1/4-chord) as a Function of $M_{\infty}$ and $X_{\max}$ . . . . .	79

Figure		Page
17	Convergence Behavior of $C_p$ (1/4-chord) as a Function of $M_\infty$ and $Y_{\max}$ . . . . .	79
18	Convergence Behavior of $C_p$ (midchord) as a Function of $M_\infty$ and $Y_{\max}$ . . . . .	80
19	Convergence Behavior of $C_p$ (midchord) as a Function of $M_\infty$ and $Y_{\max}$ . . . . .	80
20	Effect of Varying the Strength of the Farfield Boundary Condition. . . . .	82
21	Effect of Uniform Element Refinement on the Solution for Pressure Coefficient. . . . .	85
22	Effect of Refining Discretization Parameter NDXA Only. . . . .	87
23	Effect of Refining Discretization Parameter NDX Only . . . . .	88
24	Effect of Refining Discretization Parameter NDY Only . . . . .	90
25	Pressure Coefficient for 6%-Thick Parabolic-Arc Airfoil for $M_\infty = 0$ . . . . .	91
26	Comparison of Results for a 6%-Thick Parabolic-Arc Airfoil for $M_\infty = 0$ . . . . .	92
27	Convergence of Solution Algorithm as a Function of Free-Stream Mach Number . . . . .	94
28	Convergence Behavior of Potential Function at the Midchord as Function of Free-Stream Mach Number. . . . .	96
29	Mach Effects on $C_p(y = 0)$ for a 6%-Thick Parabolic-Arc Airfoil. . . . .	98
30	Comparison of Results for a 6%-Thick Parabolic-Arc Airfoil at $M_\infty = 0.707$ . . . . .	99
31	Comparison of Results for a 6%-Thick Parabolic-Arc Airfoil at $M_\infty = 0.80$ . . . . .	100
32	Convergence Behavior of Iterative Solution Scheme for $M_\infty = 0.84$ . . . . .	102
33	Divergence Behavior of Iterative Solution Scheme for $M_\infty = 0.86$ . . . . .	102

Figure		Page
34	Further Iterative Behavior (Continued from Figure 33) for $M_\infty = 0.86$ . . . . .	103
35	Effect of Upwinding Parameter U for a 6%-Thick Parabolic-Arc Airfoil at $M_\infty = 0.908$ and $R = 0$ . . . . .	106
36	Effect of Upwinding Parameter U for a 6%-Thick Parabolic-Arc Airfoil at $M_\infty = 0.908$ and $R = 0.20$ . . . . .	107
37	Effect of Upwinding Parameter U for a 6%-Thick Parabolic-Arc Airfoil at $M_\infty = 0.92$ and $R = 0.20$ . . . . .	108
38	Effect of Parameter R for a 6%-Thick Parabolic- Arc Airfoil at $M_\infty = 0.908$ and $U = 0.20$ . . . . .	109
39	Effect of Parameter R for a 6%-Thick Parabolic- Arc Airfoil at $M_\infty = 0.92$ and $U = 0.20$ . . . . .	110
40	Finite Element Solutions, $R = 0.25$ and $U = 0.70$ . . . . .	114
41	Finite Element Solutions, $R = 0.25$ and $U = 0.50$ . . . . .	115
42	Effect of Element Fitting Near the Weak Shock. . . . .	117
43	Comparison of Results for a 6%-Thick Parabolic-Arc Airfoil for $M_\infty = 0.908$ . . . . .	120
44	Comparison of Two Finite Element Results for a 6%-Thick Parabolic-Arc Airfoil for $M_\infty = 0.908$ . . . . .	121
45	Finite Element Solutions, $R = 0.20$ and $U = 0.40$ . . . . .	123
46	Rectangular Element. . . . .	163

### List of Tables

Table		Page
I	Point-wise Error for Conforming Sector Elements with Radial Refinement. . . . .	59
II	Point-wise Error for Conforming Sector Elements with Angular Refinement. . . . .	61
III	Error in Circulation for Sector Element (3) for Stagnation Point $\Theta = -\pi/6$ . . . . .	63
IV	Error in Circulation for Conforming Sector Elements with Stagnation Point $\Theta = -\pi/6$ Located at the Optimum Point. . . . .	64
V	Comparison of Critical Mach Numbers . . . . .	70
VI	Domain Discretization Parameters, for $M_\infty = 0.908$ . . .	113

### Abstract

The finite element method was used to solve the nonlinear, small-disturbance, transonic, velocity-potential equation for problems of steady flow over a circular cylinder and over a thin-airfoil in a uniform steady airstream. The governing differential equation is valid for inviscid, irrotational, isentropic flow of a perfect gas to include weak shocks providing airflow separation does not occur. For compressible subsonic and transonic flows the nonlinear small-disturbance equation was expressed in iterative form as a sequence of linear equations which was solved iteratively until the difference between two successive solutions became arbitrarily small. For analysis purposes the infinite flowfield was replaced by a finite but sufficiently large domain that was discretized with sector elements for the cylinder problem and rectangular elements for the airfoil problem. The finite element equations were obtained from Galerkin's Method of Weighted Residuals. Boundary conditions of the Neumann type were imposed along the surface contour of the cylinder and along an approximate boundary in accordance with classical thin-airfoil theory for the airfoil. For both problems Dirichlet conditions were imposed along the farfield boundary from an asymptotic solution which satisfies the actual infinity condition and is valid in the farfield.

Three sub-problems were investigated for the circular cylinder. First, three different types of trial functions were investigated to approximate the solution for the velocity potential function for the case of incompressible flow without circulation. The three trial functions were: (1) a trigonometric approximation resulting in a

non-conforming element, (2) a bilinear polynomial (conforming element) typical of elements used in finite element analyses, and (3) a rational approximation resulting in a new conforming element. Convergence properties of each element were studied as a function of discretization refinement (element size). The new element proved to have superior properties for the problem solved.

The second subproblem for the cylinder was to use the two conforming elements to obtain solutions for incompressible flow with circulation. Superposition was used to split the total problem into two elementary component problems. The value of circulation was determined by enforcing the stagnation or Kutta condition after each component solution was found. An optimum way to select and refine the discretization was discovered to insure that the error in circulation was kept to a minimum.

The third subproblem for the cylinder was to solve the compressible flow problem without circulation using the new element. In the strict sense, the small-disturbance equation is not valid for compressible potential flow over a cylinder; however, the problem is mathematically well-posed with its use. The iterative solution scheme converged rapidly for subsonic flows, but failed to converge for transonic flows when the supersonic zone engulfed one or more complete elements. Predictions of the critical Mach number and subsonic velocity distributions are compared with known results.

Convergence of iterative finite element solution schemes for transonic (mixed-elliptic-hyperbolic) flows was investigated for the airfoil problem. An examination was made of the divergence behavior of solution schemes reported by other investigators who have used

finite element formulations similar to those used in this study. As a result of this examination an iterative solution procedure was developed which permitted convergence of solution schemes for mixed (transonic) flows. The procedure includes a new "upwinding" technique that accounts for the proper zone of influence for elements in the supersonic (hyperbolic) region. Governed by two parameters, the new technique alters the finite element formulation to exclude the influence of iterative downwind forces on the solution at upwind nodes. The "upwinding" technique not only "arrests" the divergence behavior of the solution scheme, but also "captures" the weak compression shock which forms automatically without the use of shock elements.

Known results from experimental data, classical solutions, finite difference solutions, and other finite element solutions are compared with the finite element solutions obtained in this study. Comparisons of velocity and pressure distributions are given for cases of incompressible flow and compressible subsonic and transonic flows.



PREDICTION OF AERODYNAMIC FORCES ON A CIRCULAR CYLINDER  
AND A THIN AIRFOIL IN A TRANSONIC AIRSTREAM  
BY THE FINITE ELEMENT METHOD

I Introduction

Analysis of transonic flow is one of the most challenging problems in potential aerodynamics today due to the nonlinear nature and mixed character of the flow. Transonic flow may occur with modern aircraft during flight maneuvers, encounters with atmospheric turbulence or wind gusts, and during accelerations to supersonic speeds. Many fighter aircraft, for example, often endure extensive portions of their mission profile at transonic speeds. During these periods violent oscillatory motion may occur which could pose a hazard to flight. Thus, the need is evident for accurate and reliable methods of analysis to predict aerodynamic loads at transonic speeds.

A renewed interest in transonic flow is manifest by the rather large volume of technical papers that have appeared in the literature within the last fifteen years. Several methods of analysis have been developed, but perhaps those most extensively used today are finite difference methods. The majority of these methods are devoted to two-dimensional potential flow analysis, although the flow is more complex in nature. This simplifying position is justifiable to some degree since selection of suitable section shapes has always been one of the stages in the design process for aircraft wings and helicopter blades.

For design purposes, and for many other problems of engineering interest, the flow about a body may be adequately described by potential aerodynamics and small disturbance theory (Ref 1). Consequently, a large portion of the technical papers on transonic flow adopt this simplifying position. The assumptions of two-dimensional, inviscid, irrotational, isentropic flow drastically simplify the coupled basic equations of fluid mechanics. Introducing a velocity potential produces a single, governing, second-order, nonlinear, partial differential equation which is valid for flows with weak shocks. Small disturbance approximations provide further reduction in analytical complexity. Errors in pressure distributions resulting from these assumptions are not severe except at stagnation points, at large angles of attack, or when extensive airflow separation occurs.

Within the last eight years a relatively new method of analysis has been used to solve potential aerodynamics problems. This new method was originally developed by structural engineers and is known as the Finite Element Method (FEM). Its application to airfoil analysis is currently being investigated by both the aircraft industry and governmental agencies.

#### Previous and Recent Works

Perhaps the first paper to propose the use of finite elements for field problems involving Laplace and Poisson equations was by Zienkiewicz and Cheung in 1965 (Ref 2). It was three years later before the FEM was used to solve an aerodynamics problem. Martin (Ref 3) used linear triangular elements and a variational principle to solve for the stream function for incompressible flow over a circular cylinder located

between parallel walls. Within a year Norrie and deVries (Ref 4-8) developed finite element techniques to solve incompressible problems for flow over single and cascading airfoils. They formulated the problem in terms of the velocity potential and used linear triangular elements along with a variational principle to obtain the finite element equations. They also made liberal uses of the superposition principle. For example, the problem of lifting flow over an airfoil was divided into thickness and lifting parts, each of which was solved by the FEM. The solutions were linearly combined and the Kutta condition applied to specify the circulation. Unfortunately, they were not able to present many computational examples due to computer limitations.

Shen (Ref 9) published an interesting paper with intent to "bring the maximum amount of a priori information theoretical and analytical, so as to minimize the chore that must be done numerically in the Finite Element Method." He formulated the problem of incompressible flow over a lifting airfoil in terms of the stream function and used a variational principle. Shen modeled the infinite domain with an inner and outer patching technique similar to that used in finite difference relaxation schemes (Ref 10). The infinite domain was divided into two super-elements or patches. The inner patch contained the airfoil and a portion of the flow field extending from the airfoil to some arbitrary but sufficiently large distance from it. The outer patch completed the infinite flowfield within which an analytically obtained asymptotic solution with undetermined parameters was used. The FEM was used to obtain the solution only in the inner patch. Globally the two solutions were matched along the common boundary separating the two patches. Shen presented some results for the circular cylinder and

Joukowski airfoils using linear triangular elements, but stated, "in actual implementation of the finite element method for the inner patch, many details remain that affect the accuracy of the results."

For steady, compressible, potential flow over an arbitrary body additional difficulties appear. The exact governing equation is non-linear, and when the free stream Mach number becomes large enough, bubbles of supersonic flow may appear over a portion of the body. For totally subsonic flow Periaux (Ref 11) was successful in using linear and quadratic triangular elements combined with an iterative solution algorithm to solve for potential flow over airfoils. Solutions were obtained from both velocity potential and stream function formulations by minimization of functionals. Shen and Habashi (Ref 12) noted that solutions derived from variational principles would not converge for supercritical Mach numbers. They proposed a local linearization of the problem which could be formulated in terms of either the stream function or the velocity potential function. The local governing differential equation for the local perturbation velocity potential  $\phi'$  was shown to be the linear small-disturbance equation  $(1 - M_e^2)\phi'_{\eta\eta} + \phi'_{\xi\xi} = 0$ . The elemental Mach number  $M_e$  was taken to be constant in element  $e$  and was calculated from the previous iteration. Coordinates  $(\xi, \eta)$  were aligned parallel and normal to the previous iteration of the streamlines. They then used linear triangular elements and the Prandtl-Glauert transformation to solve for compressible flow over a circular cylinder without circulation. Flowfields for airfoil problems were discretized by a mapping procedure using the inverse Joukowski transformation. Their results converged for compressible flow to include a small supersonic bubble, but were valid only for

Mach numbers near the critical values.

To date the most extensive application of the FEM for airfoil analysis was done by Chan and Brashears (Refs 13-17). In their initial work the small-disturbance velocity potential equation was solved for the cases of: incompressible flow about a lifting airfoil, steady compressible subsonic and transonic flows about a nonlifting airfoil, and unsteady transonic flow about an airfoil that is harmonically oscillating about a nonlifting mean state. The finite element solution was obtained with cubic triangular elements using Galerkin's method of weighted residuals. For steady compressible flow the governing differential equation was cast into an equation of the Poisson type for which finite element equations were constructed and solved by iterative algorithms. The infinite domain was divided into two sub-domains or patches as described previously. A solution was obtained in the inner patch by finite element techniques with farfield boundary conditions specified by the farfield expressions of Klunker (Ref 18). The unsteady transonic flow problem was treated as a sum of two problems after Landahl (Ref 19): (1) the non-linear transonic flow problem about a mean steady position, and (2) a linear oscillation problem about the mean steady position. Generally speaking, velocity and pressure distributions compared well with other analytical or experimental data for nonlifting subsonic flows. For steady transonic flow, the iterative Galerkin formulation failed to converge and was abandoned in later efforts. For lifting cases the finite element solutions did not compare as well with known results as solutions did for nonlifting flows. The major difficulties encountered were determining correct values of circulation and accurate estimates of the pressure distributions near

the leading and trailing edges. Predictions of pressure distributions for unsteady flows were only quantitatively comparable with experimental results.

In later works Chan and Brashears (Refs 15-17) abandoned the Galerkin formulation used in their earlier work. They tried several techniques to eliminate the improper downwind influences upon the solution at upwind supersonic nodes, but were unsuccessful when the Galerkin method was used. They, instead, adopted the least squares method of weighted residuals, but unfortunately used elements which were not compatible with the new formulation.

Recently, alternative implicit velocity formulations for small-disturbance theory have been suggested by Wellford & Hafez (Refs 20-21), Ecer (Ref 22), and Aziz (Ref 23). In order to make solutions converge, Wellford suggested adding time dependent and explicit artificial viscosity terms to the governing differential equations, expressed in terms of the velocity perturbations. Akay (Ref 24) presents a finite element model for the full, two-dimensional, potential equations using variational principles. Solutions for subcritical flows showed good agreement with experimental data, but failed for mixed flows. The use of artificial viscosity, both explicit and implicit, was introduced in the analysis to prevent divergence of solutions. The addition of viscosity caused an oscillation about some solution in the solution algorithm used, but it did not provide convergence in the absolute sense.

### Objective

The purpose of this work was to use the finite element method (FEM) to predict surface pressure distributions for two-dimensional,

potential flow over bodies in an infinite uniform flowfield for incompressible and compressible flows that include the transonic regime with weak shocks. The Galerkin method of weighted residuals, abandoned by Chan and Brashears, was used with appropriate conforming "lower" order elements. The principle objective of this study was to make as many simplifying assumptions as possible in both the flow model and the numerical approximation procedure, and determine whether a "simple" Galerkin approach is acceptable for solving a rather complicated, non-linear, mixed-flow problem in an unbounded region where discontinuities and singularities may exist.

This study was divided into two parts, flow over a circular cylinder and flow over a thin airfoil. One of the original intents of the study was to examine some of the characteristics of the FEM's application to potential flow problems. Although this intent was modified, it was accomplished, in part, with the circular cylinder problem. Three different elements were used, representing conforming and non-conforming elements. Trial solutions for bilinear, rational, and trigonometric approximations were examined. Properties of flow field discretization and application of boundary conditions were examined.

The numerical procedure for solving the velocity potential equation for transonic flows was confined to the airfoil problem. Small disturbance theory and approximations from classical thin-airfoil theory were used. The purpose for examining the transonic regime was to investigate convergence problems reported by other investigators, and attempt to develop a technique to account for the proper zone of influence in the supersonic region. If an adequate

method could be developed to exclude the downwind influence on the solution at upwind supersonic nodes, then the Galerkin procedure would not have to be abandoned as concluded by Chan and Brashears.

The Finite Element Method (Background Information). The finite element method was developed about 25 years ago by structural engineers to analyze complex structural systems. An engineering structure can be thought of as a collection of discrete elements that are inter-connected at a finite number of locations. For example, a simple pin-connected truss can be modeled by axial-rod elements. For a given static loading, the enforcement of global equilibrium (force balance) is sufficient to determine the tensile or compressive loading of each element. In a continuum, whether it be structural or otherwise, the number of connections becomes infinite. For such problems the continuum must be divided into a finite number of conveniently shaped elements and transformed into a discretized finite assemblage of nodal parameters.

In the earlier stages of finite element development static force balance formed the theoretical foundation of the method. Later, energy principles, which form a significant part of structural analysis, were used. The finite element method provided a way to approximate the global strain energy of a continuous structural system in terms of the ensemble of energies in local, discretized subsystems or elements. Nodal displacements are determined from admissible assumed displacement distributions by minimizing the strain energy functional.

In the mid-1960s the FEM was examined for possible application to non-structural problems, such as fluid flow. Successful application led to further development of the theory. It has since been generalized



to solve linear and nonlinear partial differential equations for boundary and initial value problems in many fields of engineering and mathematical science. Recently, several mathematicians have contributed to the Finite Element development and have established it as an important branch of approximation theory. Close relationships exist between finite element analysis and the classical variational concept of the Rayleigh-Ritz method in problems where variational principles apply. Unfortunately, variational principles cannot be found in all engineering problems, particularly when governing differential equations are not self-adjoint. However, for such problems the weighted residual methods, such as least squares, collocation, or the well-known Galerkin method apply. The Galerkin method is perhaps the most convenient weighted-residual method for FEM analysis.

## II Problem Descriptions

Two steady, potential flow problems are considered in this study. The first is flow about a circular cylinder and the second is flow over a thin symmetric airfoil at zero angle of attack.

### Circular Cylinder/Incompressible Flow

First consider the problem of steady, incompressible, inviscid, irrotational flow about a unit circular cylinder (i.e. radius = 1) placed in a uniform steady airstream of infinite extent. Let the free-stream be directed in the positive  $x$ -direction with coordinate systems attached to the center of the cylinder as shown in Fig 1. Let  $\Omega$  denote the infinite flowfield domain composed of points  $(r, \theta)$ . The boundary of  $\Omega$  (denoted  $\partial\Omega$ ) is composed of all points  $(r, \theta)$  on the cylinder surface (denoted  $\partial\Omega_c$ ) and the boundary at infinity (denoted  $\partial\Omega_\infty$ , i.e. points  $(r, \theta)$  as  $r \rightarrow \infty$ ). For flow with circulation a branch cut is placed in  $\Omega$  as shown in Fig 1. The purpose of the cut is discussed in a subsequent section.

Governing Equation. The governing differential equation for incompressible potential flow is the Laplace equation given by

$$\nabla^2 \Phi(r, \theta) = 0 \quad \text{for } (r, \theta) \text{ in } \Omega \quad (1)$$

where  $\Phi$  is the velocity potential function. Since the equation is linear, the potential function can be expressed as  $\Phi = U_\infty(x + \phi)$ . The term  $U_\infty x$  is the potential of the free-stream with velocity  $U_\infty$  and  $\phi$ , the perturbation velocity potential. Substituting this expression into eq 1 gives

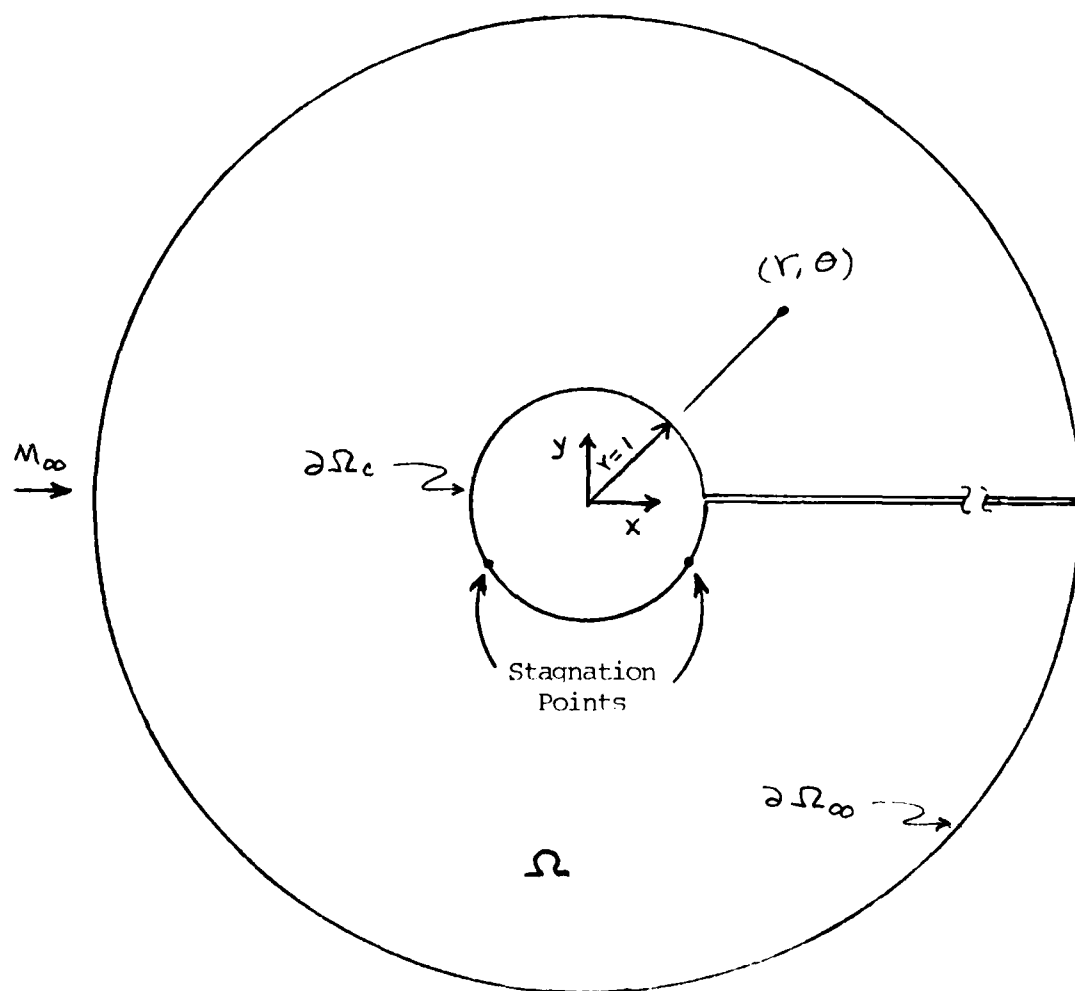


Figure 1 - Flowfield for the Circular Cylinder

$$\nabla^2 \phi(r, \theta) = 0 \quad \text{for } (r, \theta) \text{ in } \Omega \quad (2)$$

which is the governing equation for  $\phi$ .

Boundary Conditions. For the problem to be well posed, boundary conditions must be specified on the surface of the cylinder and at infinity. At infinity the disturbance velocities must vanish

$$\nabla \phi \rightarrow \vec{0} \quad \text{as } r \rightarrow \infty \quad (3)$$

The tangential condition applied along the surface of the cylinder is

$$\nabla \phi \cdot \vec{n} = 0 \quad \text{for } (r, \theta) \text{ in } \partial\Omega_c \quad (4)$$

where  $\vec{n}$  is a unit vector pointing outward from the surface. This condition reduces to

$$\phi_{,r} + \cos \theta = 0 \quad \text{for } (r, \theta) \text{ in } \partial\Omega_c \quad (5)$$

For flow with circulation the stagnation condition must be enforced at the down-stream stagnation point, which corresponds to enforcing the Kutta condition at the trailing edge of an airfoil. This condition is given by

$$\nabla \phi = \vec{0} \quad \text{at } (r, \theta) = (1, -\beta_0) \quad (6)$$

Since  $\phi_{,r} = 0$  from the tangential condition, then the stagnation or Kutta condition is satisfied by

$$\left. (\phi_{,\theta} - r \sin \theta) \right|_{(r, \theta) = (1, -\beta_0)} = 0 \quad (7)$$

In order to keep  $\phi$  single valued, a branch cut is placed in the flow-field as previously mentioned. It can be shown that the jump in potential across the cut ( $\phi^+ - \phi^-$ ) is equal to the circulation defined by

$$\Gamma = \oint_{\partial\Omega_c} \vec{v} \cdot d\vec{s} \quad (8)$$

$\vec{v}$  is the tangential velocity and  $d\vec{s}$  is tangent to the cylinder. Thus, across the cut the condition

$$\Gamma = \phi^+ - \phi^- \quad (9)$$

must be enforced. The actual value of  $\Gamma$  is unknown, but can be determined by enforcing the stagnation condition. The numerical procedure for doing this is described in the next chapter.

When the entire domain  $\Omega$  is not discretized, then an additional boundary condition is needed when symmetric flow (no circulation) is considered. The problem of flow without circulation can be solved in the upper-half space defined by  $y \geq 0$  (denoted  $\Omega_{1/2}$ ). This is possible due to symmetry. Actually, any quadrant of  $\Omega$  would be sufficient to solve for  $\phi$  in all of  $\Omega$ . In the half-space the additional boundary condition imposed along the axis  $y=0$  for all points  $r \geq 1$  (denoted  $\partial\Omega_0$ ) is

$$\phi_{,y} = 0 \quad \text{along } \partial\Omega_0 \quad (10)$$

This condition is enforced from symmetry considerations and is not a physical boundary condition.

### Thin Airfoil

Consider the problem of steady, inviscid, irrotational, isentropic flow about a thin airfoil placed in a steady, uniform airstream of infinite extent. Let the free stream be directed in the positive  $x$ -direction with the airfoil chord aligned with the  $x$ -axis. Let  $\Omega$  denote the infinite flowfield domain composed of points  $(x, y)$ . The boundary of  $\Omega$  (denoted  $\partial\Omega$ ) is composed of all points  $(x, y)$  on the airfoil surface (denoted  $\partial\Omega_A$ ) and the boundary at infinity (denoted  $\partial\Omega_\infty$ , i.e. points  $(x, y)$  as  $r \rightarrow \infty$ ), as depicted in Fig 2. For cases involving lift a cut is placed in the flowfield leading from the trailing edge to the boundary at infinity. The reasons for the cut are essentially the same for the airfoil as for the cylinder with circulation, which has been previously described.

Governing Differential Equation. For a thin airfoil, small-perturbation theory can be used to describe the disturbances in the free-stream velocity caused by the presence of the airfoil. The governing differential equation for such a problem is the well-known small-disturbance equation for the non-dimensional velocity potential function  $\phi(x, y)$  (Ref 19:4). The equation is

$$[1 - M_\infty^2 - M_\infty^2(1 + \gamma)\phi_x] \phi_{xx} + \phi_{yy} = 0 \quad (11)$$

for all points  $(x, y)$  in  $\Omega$ .  $M_\infty$  is the free stream Mach number and  $\gamma$  the ratio of specific heats ( $\gamma = 1.4$  for air). The dimensionless variables  $(\phi, x, y)$  are related to the physical ones  $(\bar{\phi}, \bar{x}, \bar{y})$  by the relations:  $x = \bar{x}/c$ ,  $y = \bar{y}/c$ ,  $\phi = \bar{\phi}/U_\infty c$

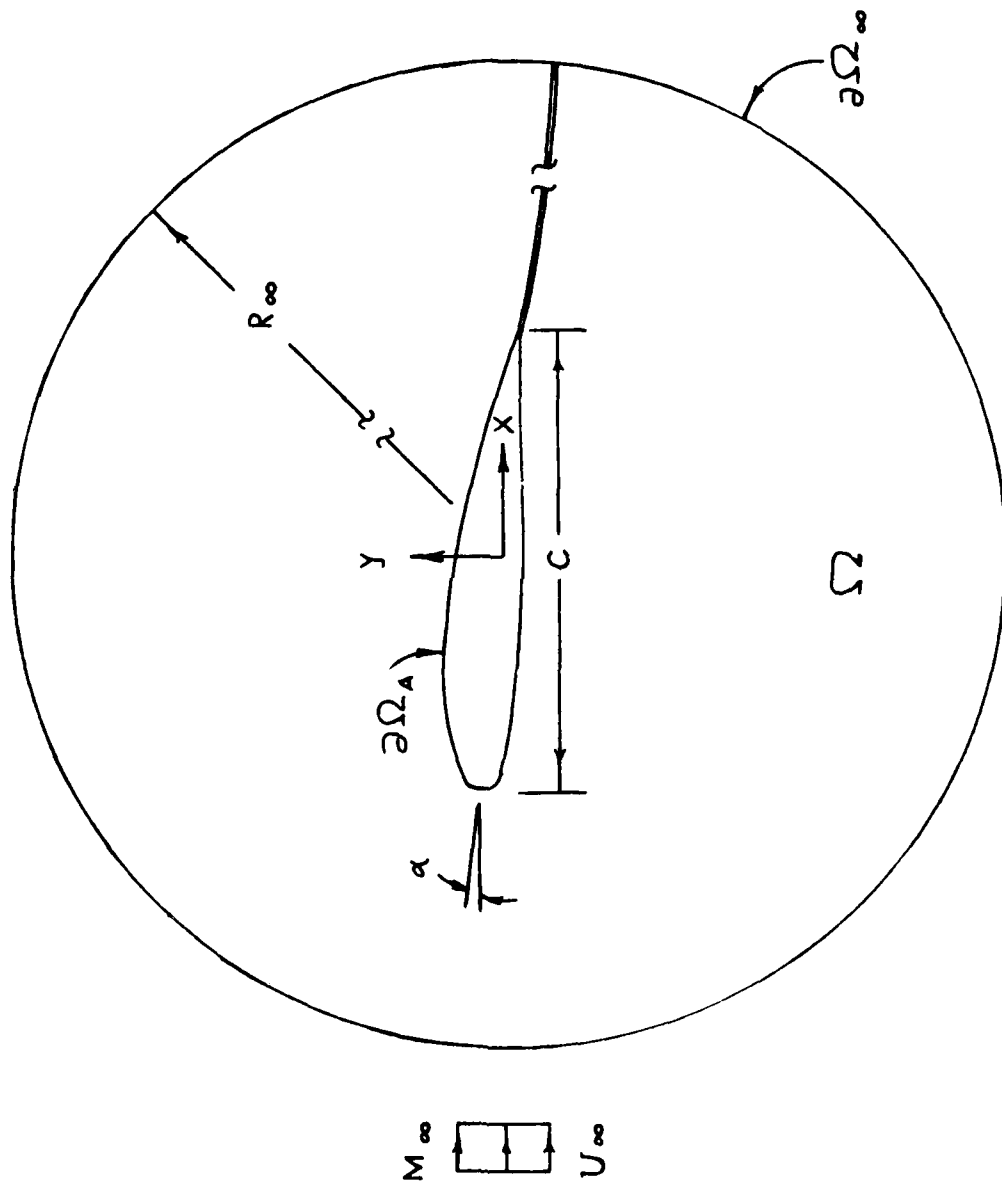


Figure 2 - Flowfield for the Airfoil

where  $c$  is the airfoil chord length and  $U_\infty$ , the free stream velocity. When considering strictly transonic flow over an airfoil with a given thickness ratio, slightly different transformations relating  $y$  and  $\bar{y}$  are used (Ref 10). In the strict sense, eq 11 is valid only for isentropic flow, but it is a good approximation for flows with weak shocks (Ref 19:2).

For incompressible flow ( $M_\infty = 0$ ), eq 11 reduces to the Laplace equation which is valid for bodies of arbitrary shape (e.g. the circular cylinder). For low subsonic flow (i.e.  $0 < M_\infty < 0.5$ ) the nonlinear term  $\phi_x \phi_{xx}$  is often assumed small compared to the other terms and dropped, as done in linear theory. However, for flows in the transonic range, the nonlinear term becomes important and must be kept to model the mixed subsonic-supersonic flow regime accurately. In this study the nonlinear term is retained even for low subsonic flow.

Equation 11 is a nonlinear, second-order, partial differential equation of mixed type. The mixed character is caused by a change in sign of the  $\phi_x \phi_{xx}$  coefficient. For subsonic, free-stream Mach numbers the sign change is caused by the behavior of the nonlinear term. For subcritical values of  $M_\infty$  the variable coefficient of  $\phi_x \phi_{xx}$  is positive and eq 11 is elliptic everywhere in  $\Omega$ . When  $M_\infty$  is increased slightly beyond some critical value, the coefficient becomes negative in a region in the vicinity of the maximum thickness point of the airfoil. Equation 11 is hyperbolic in this region while it remains elliptic in the remainder of  $\Omega$ . Along the line which separates these mixed flow regions, the coefficient is zero and the equation is parabolic. Unfortunately, the position of the parabolic or sonic line is not known a priori. In addition, the existence of the nonlinear



term permits solutions which have discontinuous first derivatives. These discontinuities are associated with the presence of weak compression shocks which separate the downstream side of the hyperbolic and elliptic regions. These shocks permit the supersonic flow in the hyperbolic region to return to subsonic flow in the elliptic region over very small distances.

Boundary Conditions. For the problem to be well posed, a boundary condition must be specified on the surface of the airfoil and at infinity. At infinity the disturbance velocity must vanish, i.e.

$$\nabla \phi \rightarrow 0 \quad \text{as} \quad \vec{r} \rightarrow \infty \quad (12)$$

The impervious or tangential condition for flow along the airfoil surface is given by

$$\phi_{,y} = (1 + \phi_{,x}) \frac{df}{dx} \quad \text{for } (x, y) \text{ in } \partial \Omega_A \quad (13)$$

where  $F(x, y) = y - f(x) = 0$  describes the surface of the airfoil. To be consistent with linear small-perturbation theory, the  $\phi_{,x}$  term in the tangential boundary condition is normally neglected compared to unity. This boundary condition is not enforced on the surface  $F(x, y) = 0$ . Instead, it is applied along the axis  $y = 0^+$ , in accordance with classical thin-airfoil theory (Ref 58).

For nonlifting thin airfoils the solution can be obtained in the upper half-space. From symmetry considerations the condition

$$\phi_{,y} = 0 \quad (14)$$

must be applied for all points along the axis  $y = 0$  which lie beyond the leading and trailing edges of the airfoil. For more discussion

about this condition refer to the description of the circular cylinder.

#### Circular Cylinder/Compressible Flow

The description of the compressible flow problem for the cylinder was purposely placed after that of the airfoil. The problem of symmetric, steady, potential flow over a circular cylinder can be formulated in half-space (denoted  $\Omega_{1/2}$ ), as described for the incompressible problem. The governing equation when compressibility is considered is no longer the Laplace equation, but is highly nonlinear and of mixed type (Ref 24). The exact potential equation is

$$\begin{aligned} (\Phi_{,x} - \alpha^2) \Phi_{,xx} + 2 \Phi_{,x} \Phi_{,y} \Phi_{,xy} \\ + (\Phi_{,y} - \alpha^2) \Phi_{,yy} = 0 \end{aligned} \quad (15)$$

where

$$\alpha^2 = \alpha_\infty^2 + \frac{\gamma-1}{2} \left[ \mathcal{V}_\infty^2 - (\Phi_{,x}^2 + \Phi_{,y}^2) \right]$$

This equation is a nonlinear, second-order, mixed elliptic-parabolic-hyperbolic, partial differential equation. It reduces to the Laplace equation for incompressible flow and to the small-disturbance velocity potential equation (i.e. eq 11) for flow over slender bodies. Instead of using the exact governing equation for the compressible problem, the small-disturbance potential equation for transonic flow was selected as the governing differential equation. From a physical viewpoint eq 11 does not accurately model the flow over the cylinder since the velocity

perturbations become large. From a mathematical perspective it can be solved for the cylinder when appropriate boundary conditions are specified. The physical validity of the solution can be evaluated by comparison with solutions of the exact potential equation. Thus, the assumed governing differential equation for compressible flow over the cylinder is given by eq 11

$$\left[1 - M_\infty^2 - M_\infty^2 (1 + \gamma) \phi_x\right] \phi_{xx} + \phi_{yy} = 0 \quad (11)$$

The cylinder radius is used in place of the chord length to nondimensionalize eq 11 for the cylinder problem.

The boundary conditions for the symmetric compressible problem are described in a previous section. They are given by eqs 3, 5, and 10:

$$\nabla \phi \rightarrow \vec{0} \quad \text{as } r \rightarrow \infty \quad (3)$$

$$\phi_{,r} + \cos \theta = 0 \quad \text{for } (r, \theta) \text{ in } \partial \Omega_c \quad (5)$$

$$\phi_{,\theta} = 0 \quad \text{for } (r, \theta) \text{ in } \partial \Omega_c \quad (10)$$

### III Analysis of the Cylinder Problem

#### Flowfield Discretization

A finite element solution of the governing differential equation for the cylinder problem requires that the flowfield be discretized by a finite number of elements. Two techniques are possible; for each technique domain  $\Omega$  is replaced by a finite domain  $\Omega_f$ . First of all, one could take  $\Omega_f$  to be very large, and require that the actual gradient boundary conditions, expressed by eq 3, be enforced along the farfield boundary. Since these boundary conditions and also those specified on the airfoil surface are of the Neumann type, then the solution of the governing differential equation can only be determined to within an arbitrary constant. If this technique was used, then one must specify the value of  $\phi$  at some point, preferably at a nodal point along the farfield boundary, so the solution can be uniquely determined everywhere.

The second possible technique is to impose along the farfield boundary ( $\partial\Omega_f$ ) the condition  $\phi = \phi_{FF}$ . The expression for  $\phi_{FF}$  should be an asymptotic solution which satisfies the infinity condition and is valid in the farfield of  $\Omega$  (Ref 18). This approach is commonly adopted by investigators using finite difference methods (Refs 1, 10, 40). It is also employed by others using finite element methods (Refs 9, 12, 13) and will be used in the present analysis. Generally speaking, a relatively smaller domain  $\Omega_f$  is required for the second technique than for the first. This means for a desired degree-of-accuracy fewer degrees-of-freedom are needed to solve the problem, which translates into lower computational costs.

A number of different elements can be used to discretize domain  $\Omega_f$ . When triangles (Ref 3) or quadrilaterals (Ref 13) are used, the shape of domain  $\Omega_f$  is altered since the discretization does not exactly describe the boundary shape. This approximation may not introduce significant error in the solution unless large elements are used near the boundaries. The isoparametric quadrilaterals described by Raju (Ref 27) or those developed in this study will exactly discretize domain  $\Omega_f$ . For this reason, the element shown in Fig 3 will be used for the cylinder problems considered. Figures 4 and 5 show the discretization of  $\Omega_f$  for problems of symmetric flow and flow with circulation, respectively.

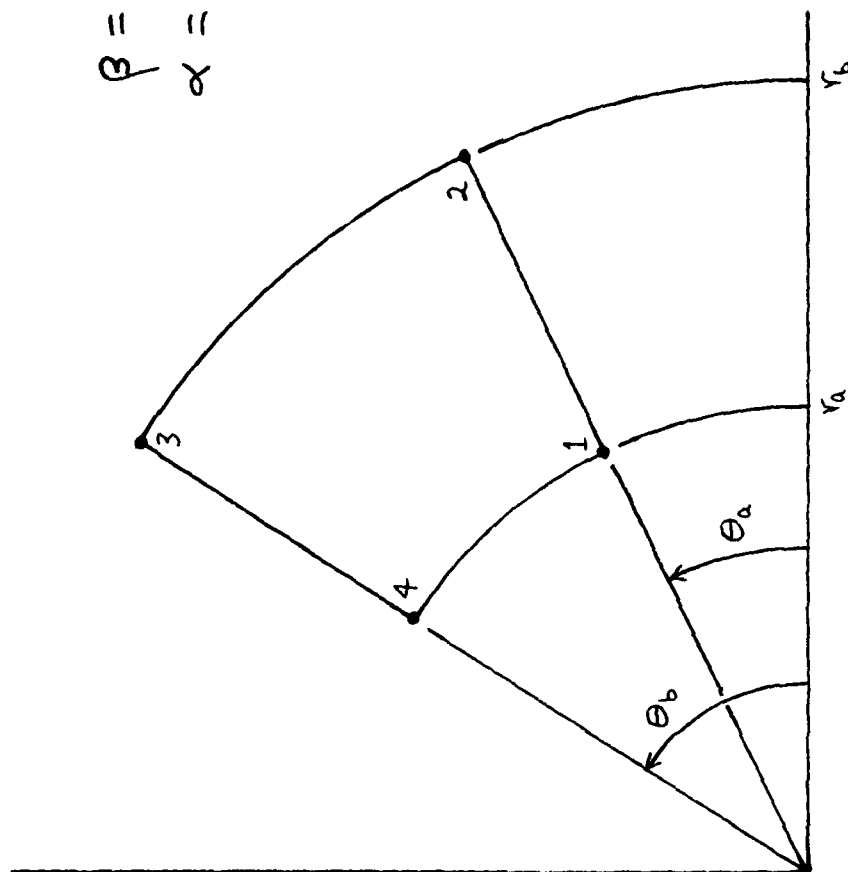
#### Incompressible Flow

Before describing the finite element analyses of this problem, a further simplification will be discussed.

Superposition. When incompressible flow with circulation is considered, the velocity potential function may be represented by two simpler component functions. Since the governing differential equation and boundary conditions are linear, then the perturbation potential function can be expressed as

$$\phi = \phi_t + \Gamma \phi_l \quad (16)$$

This superposition of solutions will produce two problems, each of which can be solved without concern about what the value of circulation should be or how it should be handled numerically. The function  $\phi_t$  is the solution for the thickness or symmetric problem, and  $\phi_l$  the solution of the lifting problem with unit circulation. The actual



$$\beta = \theta_b - \theta_a$$

$$\alpha = r_b / r_a$$

Figure 3 - Sector Element Geometry

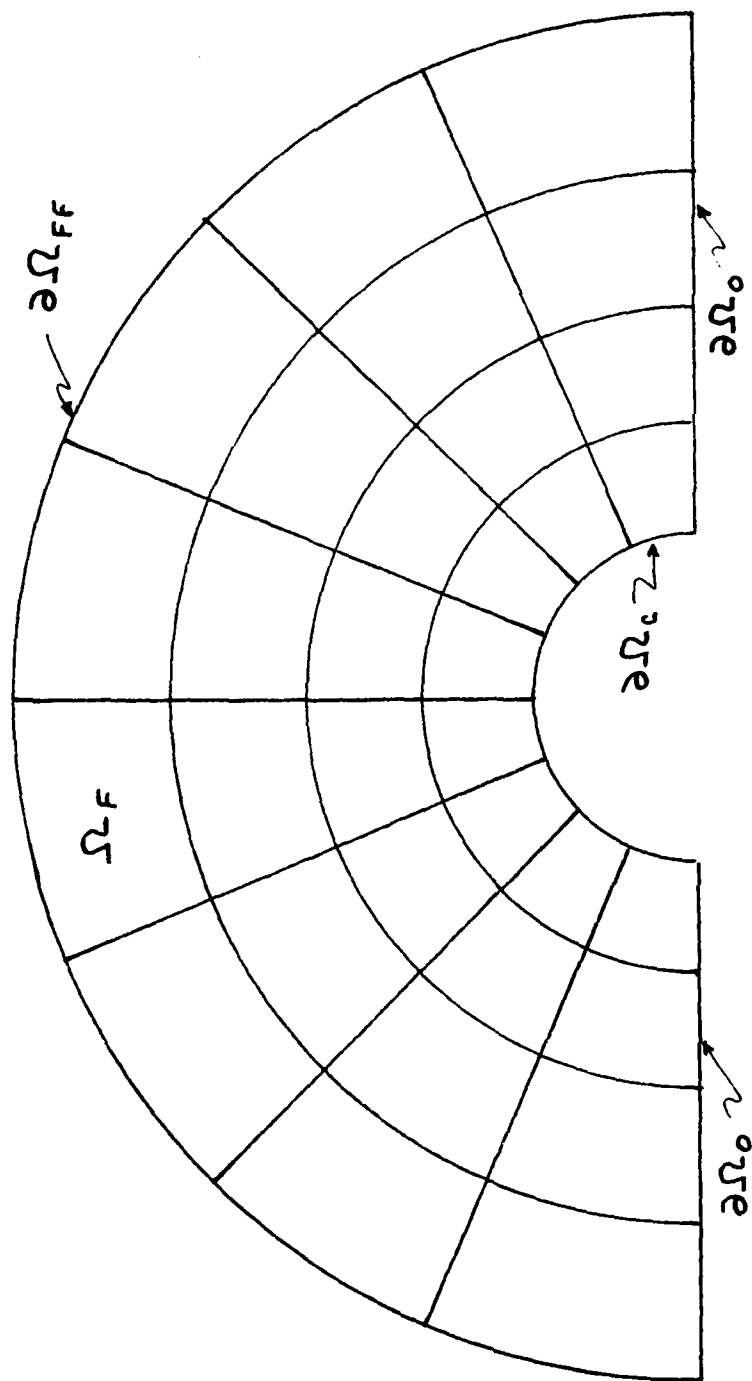
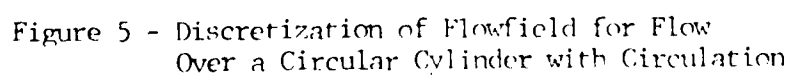


Figure 4 - Discretization of Flowfield for Flow Over  
a Circular Cylinder without Circulation





value of circulation ( $\Gamma$ ) is determined from the stagnation condition, eq 7, after each of the two component solutions are known.

Substituting eq 16 into the governing differential equation and boundary conditions one obtains two problems. First, the symmetric or thickness problem is defined by

$$\underline{\text{DE:}} \quad \nabla^2 \phi_t(r, \theta) = 0 \quad \text{for } (r, \theta) \text{ in } \Omega_F \quad (17)$$

$$\underline{\text{BC's:}} \quad \phi_{t,r} + \cos \theta = 0 \quad \text{for } (r, \theta) \text{ in } \partial\Omega_c \quad (18)$$

$$\phi_{t,\theta} = 0 \quad \text{for } (r, \theta) \text{ in } \partial\Omega_o \quad (19)$$

$$\phi_t = \phi_s \quad \text{for } (r, \theta) \text{ in } \partial\Omega_{FF} \quad (20)$$

Secondly, the lifting problem is defined by

$$\underline{\text{DE:}} \quad \nabla^2 \phi_l(r, \theta) = 0 \quad \text{for } (r, \theta) \text{ in } \Omega_F \quad (21)$$

$$\underline{\text{BC's:}} \quad \phi_{l,r} = 0 \quad \text{for } (r, \theta) \text{ in } \partial\Omega_c \quad (22)$$

$$\phi_l = \phi_v \quad \text{for } (r, \theta) \text{ in } \partial\Omega_{FF} \quad (23)$$

$$\phi_l^+ - \phi_l^- = 1 \quad \text{for } (r \geq 1, \theta = 0^\pm) \quad (24)$$

The functions  $\phi_s$  and  $\phi_v$  are farfield expressions for the thickness and lifting problems, respectively. They represent velocity potentials for a source and vortex of unit strength. After  $\phi_c$  and  $\phi_l$  are known,  $\Gamma$  is determined from eq 7. Substituting eq 16 into eq 7 and

solving for  $\Gamma$  gives

$$\Gamma = \frac{r \sin \theta - \phi_{t,\theta}}{\phi_{l,\theta}} \quad (25)$$

$(r, \theta) = (1, -\beta_0)$

Finite Element Solution. Suppose  $\Omega_F$  is discretized by a total of  $E$  elements with a total of  $N$  system nodes. The approximate solution of the Laplace equation, which governs each of the two problems described, is obtained from the method of weighted residuals as expressed by

$$\iint_{\Omega_F} \nabla^2 \phi(r, \theta) \psi_i(r, \theta) dA = 0 \quad (26)$$

for  $i = 1, \dots, N$ . Functions  $\psi_i(r, \theta)$  are weight functions that will be specified later by the Galerkin method. Integration by parts or using Green's Theorem gives

$$\iint_{\Omega_F} \nabla \phi \cdot \nabla \psi_i dA - \int_{\partial \Omega_F} \nabla \phi \cdot \vec{n} \psi_i dS = 0 \quad (27)$$

The functions  $\phi$  and  $\psi_i$  are chosen from a class of functions so that eq 27 is integrable. When  $\Omega_F$  is discretized by finite elements, then  $\phi$  and  $\psi_i$  must be continuous across inter-element boundaries and have measurable first derivatives throughout  $\Omega_F$ . This means that  $\phi$  and  $\psi_i$  cannot be piecewise constants, but they can be piecewise linear or bilinear functions, providing continuity is enforced across inter-element boundaries.

The Galerkin method of weighted residuals is used to obtain the finite element solution. Piecewise trial functions are chosen to

approximate  $\phi$  which satisfy both the continuity requirements and the essential boundary conditions (i.e. boundary conditions for which  $\phi$  is specified). Within each sector element, denoted  $e$ , the trial function can be expressed as

$$\phi^e(r, \theta) = N_j(r, \theta) \phi_j^e \quad (28)$$

for  $j=1, \dots, 4$ . The repeated index  $j$  indicates summation over the range of the index.  $N_j(r, \theta)$  are basis or shape functions and  $\phi_j^e$  are the unknown nodal values of the potential function. For Galerkin's method the weight functions  $\psi_i$  are set equal to the shape functions  $N_i(r, \theta)$ . Since the basis functions are chosen to be continuous across inter-element boundaries, then eq 27 can be written for each element as

$$\iint_{\Omega_e} \nabla \phi^e \cdot \nabla N_i dA - \int_{\partial \Omega_e^*} \nabla \phi \cdot \vec{n} N_i dS = 0 \quad (29)$$

for  $i=1, \dots, 4$ . The star  $*$  notation on the boundary term signifies that the term can be non-zero only for elements  $e$  that border the boundary of  $\Omega_F$ . For all other elements the boundary integral is zero. Substituting eq 28 into eq 29, and also putting the actual gradient boundary conditions into the boundary term, produces elemental equations of the form

$$K_{ij}^e \phi_j^e = f_i^e \quad (30)$$

The matrix  $K_{ij}^e$  is referred to as the elemental stiffness matrix and

is given by

$$K_{ij}^e = \iint_{\Omega_e} \left( N_{i,r} N_{j,r} + \frac{1}{r^2} N_{i,\theta} N_{j,\theta} \right) dA \quad (31)$$

The form of vector  $f_i^e$  depends on the gradient boundary conditions for the problem being considered and will be specified in later sections.

The essential boundary conditions, which are imposed on the trial functions, are enforced after the assembly of elemental equations. Thus,  $\psi_i$  in the boundary term of eq 27 is selected to be zero along segments of  $\partial\Omega_F$  where  $\phi$  is specified (i.e. the farfield boundary,  $\partial\Omega_{FF}$ ). The usual assembly procedure is used to transform all of the elemental equations into a global system of equations which can be expressed as

$$K_{ij} \phi_j = F_i \quad (i, j = 1, \dots, N) \quad (32)$$

Global expressions  $K, \phi, F$  are the counterparts of elemental expressions  $K^e, \phi^e, f^e$  respectively. Equation 32 is reduced to the final set of system equations by enforcing the essential boundary conditions along  $\partial\Omega_{FF}$ . First, eq 32 is partitioned as follows

$$\begin{bmatrix} K_{aa} & K_{ab} \\ K_{ba} & K_{bb} \end{bmatrix} \begin{Bmatrix} \phi_a \\ \phi_b \end{Bmatrix} = \begin{Bmatrix} f_a \\ f_b \end{Bmatrix} \quad (33)$$

Vector  $\{\phi_b\}$  is composed of the  $L$  nodal values of  $\phi_{FF}$  which lie along  $\partial\Omega_{FF}$  and is computed from the farfield expression  $\phi = \phi_{FF}$ . Vector  $\{\phi_a\}$  is composed of the remaining  $M = N - L$  unknown nodal values of  $\phi$ , which is determined from eq 33 by inverting matrix

$[K_{aa}]$  to give

$$\{\phi_a\} = [K_{aa}]^{-1} (\{f_a\} - [K_{ab}]\{\phi_b\}) \quad (34)$$

The assembly and reduction procedure just described will be followed throughout this report.

Trial Functions. Three trial functions were chosen to approximate the solution of  $\phi$  within the sector element shown in Fig 3. They are:

$$(1) \quad \phi^e(r, \theta) = a_1 + b_1 \frac{\sin \theta}{r} + c_1 \frac{\cos \theta}{r} + d_1 \theta \quad (35)$$

$$(2) \quad \phi^e(r, \theta) = a_2 + b_2 r + c_2 \theta + d_2 r \theta \quad (36)$$

$$(3) \quad \phi^e(r, \theta) = a_3 + b_3 r^{-1} + c_3 \theta + d_3 r^{-1} \theta \quad (37)$$

Constants ( $a_k, \dots, d_k$ ) can be expressed as functions of the unknown nodal value of  $\phi^e$  and the geometric parameters of the element.

When the constants are evaluated, each of the trial functions can be written in the form expressed by eq 28

$$\phi^e(r, \theta) = N_j(r, \theta) \phi_j^e, \quad (j=1, \dots, 4) \quad (28)$$

The expressions for  $N_j(r, \theta)$  are given in Appendices A-C for each of the above trial functions. Throughout the remainder of this report the superscript  $e$  will be omitted when it is clearly understood that elemental quantities are being considered.

Symmetric Flow. First, consider the problem of symmetric flow. This problem can be formulated by either considering all of domain

$\Omega_F$  or half of it. Typical discretizations are shown in Figs 4 and 5. Using Galerkin's method eq 27, as expressed by eq 29, can be written for element  $e$  as

$$\iint_{\Omega_e} (\nabla N_i \cdot \nabla N_j) dA \phi_j^e = \int_{\partial\Omega_e^*} \nabla \phi \cdot \vec{n} N_i dS \quad (38)$$

for  $(i, j = 1, \dots, 4)$ . The star  $*$  notation on the boundary term signifies that the term is present only for elements which intersect  $\partial\Omega_c$  and  $\partial\Omega_o$ . When eq 18, the boundary condition, is substituted into eq 38, the results can be written as

$$K_{ij}^e \phi_j^e = f_i^e \quad (30)$$

where stiffness matrix  $K_{ij}^e$  is given by eq 31. The only non-zero values for  $f_i^e$  comes from elements which contact the cylinder surface and is defined by

$$f_i^e = \int_{\theta_a}^{\theta_b} N_i \cos \theta r |d\theta \quad (39)$$

$r = r_a = 1$

The symmetric problem was solved using the three sector elements described in Appendices A-C. The derivations of  $K_{ij}^e$  and  $f_i^e$  are also presented in these appendices. The assembly, reduction, and solution procedure described in the previous section was followed. The expression for the farfield potential, needed to reduce the assembled equations, is given by

$$\phi_{FF} = \phi_s = \cos/r \quad \text{for } (r, \theta) \text{ in } \partial\Omega_{FF} \quad (40)$$

where  $r = R_{FF}$  is the radius of  $\partial\Omega_{FF}$ .

Flow With Circulation. When circulation or lift is present the entire domain  $\Omega_F$  must be discretized as shown in Fig 5. Along the branch cut, nodes are placed at pair-points located on opposite sides of the cut. The difference in potential between pair-point nodes must be equal to the value of circulation.

A convenient way to consider flow with circulation is to use the superposition technique previously described. The thickness or symmetric problem has already been discussed. The lifting problem, described by eqs 20-24, is formulated numerically in a similar manner. The elemental stiffness matrix  $K_{ij}^e$  is the same as for the thickness problem, since the governing differential equation for both problems is the Laplace equation.

There are four minor formulation differences between the two problems. First, the vector  $f_i^e$  equals zero for every element  $e$  for the lifting problem. This is due to the boundary condition specified along  $\partial\Omega_c$ , eq 22. Secondly, the farfield expression is given by

$$\phi_{FF} = \phi_v = \frac{-\theta}{2\pi} \quad \text{for } (r, \theta) \text{ in } \partial\Omega_{FF} \quad (41)$$

Thirdly, the required jump in potential across the branch cut must be enforced. This is done by setting the nodal values of  $\phi_1^+ = 0$  and  $\phi_2^- = -1$  for nodes along the cut. This choice is consistent with

the farfield expression as  $r \rightarrow R_{FF}$  and satisfies the requirement specified by eq 24. This choice also forces  $\phi_{\theta,r} = 0$  for points along the cut. Since this condition is true everywhere for purely circulatory flow, then no generality is lost by its use. It should be pointed out, that this choice would not be possible if the superposition principle were not used to divide the total problem into two simple problems. When the total problem is formulated without superposition, then nodal values of potential along both the upper or lower sides of the cut must be left unspecified. This will insure that the  $\phi_{\theta,r}$  is not forced to be zero, which it is not for the thickness problem. The fourth difference occurs in the reduction procedure. Since the nodal values are specified along the cut, then they have to be included with the nodes along the farfield boundary when the assembled equations are reduced. Once solutions for  $\phi_t$  and  $\phi_r$  are determined, then the circulation defined by eq 25 can be calculated.

The problem of flow with circulation was solved using sector elements (2) and (3). Appendices B and C present derivations of the elemental equations.

#### Compressible Symmetric Flow

The problem of compressible flow without circulation is formulated in the half-space shown in Fig 4. The governing differential equation for this problem is given by eq 11, and the boundary conditions by eqs 3, 5, and 10.

Discretization. The solution of this problem by the finite element method is obtained in the finite half-space  $\Omega_F$ , as described for the incompressible problem. Domain  $\Omega_F$  is discretized as shown



in Fig 4 by a total of  $E$  elements with  $N$  global nodes. Since the governing equation for this problem is the same as the equation for the airfoil problem, then the asymptotic solution used as a boundary condition along the farfield boundary ( $\partial\Omega_{FF}$ ) is given by eq 50 described in Chapter IV.

Finite Element Solution. From the method of weighted residuals, eq 11 can be expressed as

$$\iint_{\Omega_F} \left\{ [1 - M_\infty^2 - M_\infty^2(1+\gamma)\phi_x] \phi_{xx} + \phi_{yy} \right\} \psi_i dA = 0 \quad (42)$$

for  $i = 1, \dots, N$ . For appropriately chosen weight functions this expression can be integrated by parts to give

$$\begin{aligned} & \iint_{\Omega_F} \left[ \nabla\phi \cdot \nabla\psi_i - M_\infty^2 \left( \phi_x + \frac{1+\gamma}{2} \phi_x^2 \right) \psi_{i,x} \right] dA \\ & - \int_{\partial\Omega_F^*} \left[ \nabla\phi \cdot \vec{n} - M_\infty^2 \left( \phi_x + \frac{1+\gamma}{2} \phi_x^2 \right) n_x \right] \psi_i ds = 0 \end{aligned} \quad (43)$$

The finite element approximation for  $\phi$  in each element is given by eq 28 as

$$\phi(r, \theta) = N_j(r, \theta) \phi_j \quad (28)$$

for  $j = 1, \dots, 4$ . For Galerkin's method the weight functions  $\psi_i$  are set equal to the shape functions  $N_i$ . When shape functions are chosen to insure integrability of eq 43, then it can be written for every element and assembled as previously described. The elemental form of eq 43 can be written in iterative form and expressed symbolically as

$$[K_{ij} + L_{ij}(\phi^n)] \phi_j^{n+1} = f_i + g_i(\phi^n) \quad (44)$$

for  $i, j = 1, \dots, 4$ . The elemental matrix  $K_{ij}$  and vector  $f_i$  are the same as those defined for the incompressible symmetric problem. The new expressions  $L_{ij}(\phi^n)$  and  $g_i(\phi^n)$  come from the nonlinear term and are functions of the solution itself. The superscript  $n$  is associated with the iterative solution procedure which is briefly described below and discussed in more detail in Chapter IV. The superscript  $n$  should not be confused with the vector  $\vec{n}$  which is the unit outward normal along the cylinder surface.

The iterative form of the elemental equations comes from the way the governing equation is solved. The nonlinear term,  $\phi_{,x}^2$  in eq 43, is written iteratively as  $\phi_{,x}^n \phi_{,xx}^{n+1}$ . Essentially, the potential function  $\phi$  is replaced by a sequence of functions  $\{\phi^0, \phi^1, \dots, \phi^n, \phi^{n+1}\}$ , which generate a sequence of equations expressed by eq 44. These equations are solved for each iteration until the sequence of potential functions converges. Convergence is assumed when

$$\left| \frac{\phi^{n+1} - \phi^n}{\phi^n} \right| \leq \epsilon \quad (45)$$

for some small  $\epsilon$ .

An additional approximation is made to simplify the integrations required by eq 43. In the nonlinear term the derivative  $\phi_{,x}^n$  is assumed to be a constant in each element. The constant chosen is the average value of  $\phi_{,x}^n$  computed from

$$K_e^n = \frac{1}{A_e} \iint_{\Omega_e} (\phi_{,x}^n)^e dA \quad (46)$$

This approximation is made only for the cylinder problem. The non-linear term is not locally linearized in this sense for the airfoil problem, but is treated in a more exact manner. For this approximation matrix  $L_{ij}(\phi^n)$  can be expressed in two parts as  $L_{ij}(\phi^n) = L_{ij}^D(\phi^n) + L_{ij}^C(\phi^n)$ . These expressions are given by

$$\begin{aligned} L_{ij}^D(\phi^n) = & -M_\infty^2 [1 + K_e^n (1+\gamma)] \iint_{\Omega_e} \left[ \cos^2 \theta N_{i,r} N_{j,r} \right. \\ & - \frac{\sin \theta \cos \theta}{r^2} (N_{i,r} N_{j,\theta} + N_{i,\theta} N_{j,r}) \\ & \left. + \frac{\sin^2 \theta}{r^2} N_{i,\theta} N_{j,\theta} \right] r dr d\theta \end{aligned} \quad (47)$$

and

$$L_{ij}^C(\phi^n) = -M_\infty^2 [1 + K_e^n (1+\gamma)] \int_{\partial \Omega_e^c} \frac{\sin \theta \cos \theta}{r} N_i N_{j,\theta} r \Big|_{r=r_a=1} d\theta$$

Vector  $g_i(\phi^n)$  is given by (48)

$$g_i(\phi^n) = M_\infty^2 [1 + K_e^n (1+\gamma)] \int_{\partial \Omega_e^c} \cos^3 \theta N_i r \Big|_{r=r_a=1} d\theta \quad (49)$$

The symmetric compressible problem was solved using sector element (3). Appendix C contains a description of the element and the derivatives of the elemental equations.

#### IV Analysis of Flow Over a Thin Airfoil

The governing equation and boundary conditions for flow over a thin airfoil are described in Chapter II. This chapter describes the numerical analysis of the problem by the Finite Element Method. Many of the formulation techniques and procedures that are used, have been described in Chapter III for the cylinder problem. Similar discussions are not repeated for the airfoil; instead, the reader should refer to the appropriate sections of that chapter for more detail.

##### Flowfield Discretization

The infinite flow domain  $\Omega$  is replaced by a finite but sufficiently large domain  $\Omega_F$  with the potential specified along the far-field boundary  $\partial\Omega_{FF}$ . A detailed discussion of the reasons for this approximation is given in Chapter III. The condition imposed along  $\partial\Omega_{FF}$  is the farfield expression of Klunker (Ref 18) given by

$$\begin{aligned}\phi_{FF} = & \frac{1}{\pi\beta_1} \frac{x}{x^2 + (\beta_1 y)^2} \tau \int_{\text{chord}} f(\xi) d\xi \\ & + \frac{\Gamma}{2\pi} \left[ \frac{\pi}{2} \operatorname{sgn}(y) + \tan^{-1} \frac{x}{\beta_1 y} \right] \\ & + \frac{\gamma+1}{4\pi\beta_1} \iint_{\Omega_F} \frac{u^2(\xi, \eta)(x-\xi)}{(x-\xi)^2 + \beta_1^2(y-\eta)^2} d\xi d\eta\end{aligned}\quad (50)$$

where  $\beta_1 = \sqrt{1 - M_\infty^2}$

The first term in eq 50 is directly associated with the thickness distribution ( $\tau$  is the thickness ratio) of the airfoil, and is the dominant term for nonlifting flow (Ref 18). For lifting flow, the second term is the most dominant of the three and was the only term included in Chan's formulation (Ref 13). The expression  $\text{sgn}(y)$  is required to account for the jump of potential in the farfield downstream of the trailing edge. For lifting flow, a branch cut must be included in  $\Omega_F$  extending from the trailing edge to the farfield boundary. Across this cut the jump of potential is forced to equal the value of  $\Gamma$  appearing in eq 50. The last term is of highest order and involves an area integration over the entire domain  $\Omega_F$ . When this term is included in the farfield expression, an iterative solution algorithm must be used since the term depends upon the solution itself. The effect of neglecting the last term is evaluated in Chapter VI.

Consider the problem of flow over a symmetric airfoil at zero angle of attack. From symmetry considerations the problem can be formulated in the half-space. Figure 6 shows an initial division of  $\Omega_F$  into three segments or super-elements. Since the tangential boundary condition for a thin airfoil is enforced along the  $y=0$  axis, then the first row of elements used to discretize the center segment must extend to the chord line ( $x$ -axis). Any type of element with straight line boundaries (i.e. triangles, rectangles, etc.) could be used to discretize the super-elements. After selecting the type of element to be used, one could write a computer subroutine to automatically discretize each super-element from a few input parameters which describe how the segment is to be divided into smaller parts. This procedure was followed for both the cylinder and the airfoil problem; however, the

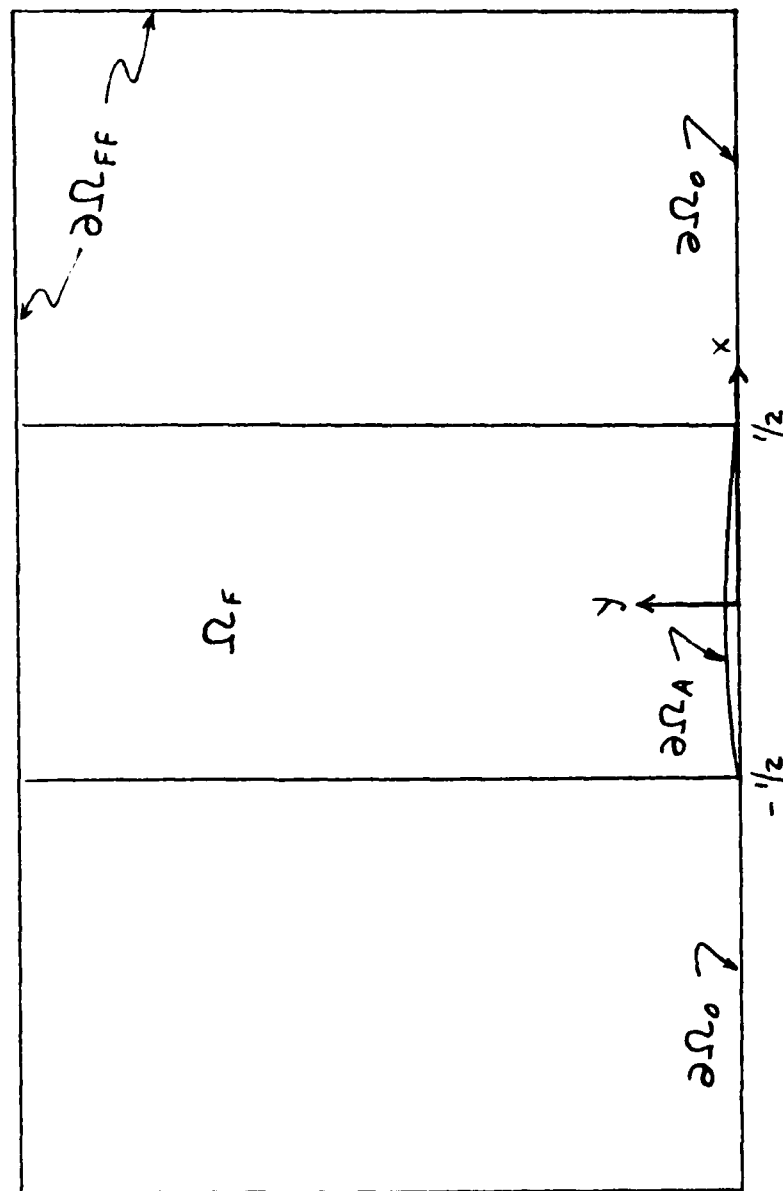


Figure 6 - Initial Flowfield Discretization for Flow Over a Symmetric Nonlifting Airfoil

details are not important and will not be discussed.

A slight modification in the described discretization of the center super-element would be required if the tangential boundary condition was applied along the actual airfoil contour. For this case, elements in the center segment would not extend to  $y=0$ . Elements would have to be selected to either match or approximately match the shape of the thickness profile. This difference in discretizations becomes significant when thick airfoils are to be analyzed, and is discussed further after the elemental equations are formulated.

#### Iterative Approximation

If the solution of eq 11, the governing differential equation, is directly formulated by finite element methods, then a set of second-order, nonlinear, algebraic equations will result. These equations would have to be solved by some iterative technique such as Newton-Raphson. This type of solution process can be avoided by directly expressing and solving the governing equation in iterative form. First, eq 11 is written as

$$\left[ (1 - M_\infty^2) \phi_{,x} - M_\infty^2 \frac{1+\gamma}{2} \phi_{,x}^2 \right]_{,x} + \phi_{,yy} = 0 \quad (51)$$

As described previously for the cylinder, the nonlinear term  $\phi_{,x}^2$  is approximated iteratively by  $\phi_{,x}^n \phi_{,x}^{n+1}$  where  $n$  denotes the iteration number. In essence potential  $\phi$  is replaced by a sequence of potentials  $\{ \phi^0, \phi^1, \dots, \phi^n, \phi^{n+1} \}$ , which converges when

$$\left| \frac{\phi^{n+1} - \phi^n}{\phi^{n+1}} \right| \leq \epsilon \quad (45)$$

for small  $\epsilon$ . Thus, eq 51 written in iterative form becomes

$$\left[ (1 - M_\infty^2) \phi_{,x}^{n+1} - M_\infty^2 \frac{1+\gamma}{2} \phi_{,x}^n \phi_{,x}^{n+1} \right]_{,x} + \phi_{,yy}^{n+1} = 0 \quad (52)$$

### Finite Element Solution

Suppose the half-space  $\Omega_F$  is discretized by a total of  $E$  elements with  $N$  nodes. The approximate solution of eq 52 is obtained from the method of weighted residuals as expressed by

$$\iint_{\Omega_F} \left\{ \left[ (1 - M_\infty^2) \phi_{,x}^{n+1} - M_\infty^2 \frac{1+\gamma}{2} \phi_{,x}^n \phi_{,x}^{n+1} \right]_{,x} + \phi_{,yy}^{n+1} \right\} \psi_i dA = 0 \quad (53)$$

where  $i = 1, \dots, N$ . For suitable weight functions  $\psi_i$ , this equation can be integrated by parts to give

$$\begin{aligned} & \iint_{\Omega_F} \left\{ \left[ 1 - M_\infty^2 - M_\infty^2 \frac{1+\gamma}{2} \phi_{,x}^n \right] \phi_{,x}^{n+1} \psi_{i,x} + \phi_{,y}^{n+1} \psi_{i,y} \right\} dA \\ & - \int_{\partial\Omega_F} \left\{ \left[ 1 - M_\infty^2 - M_\infty^2 \frac{1+\gamma}{2} \phi_{,x}^n \right] \phi_{,x}^{n+1} n_x + \phi_{,y}^{n+1} n_y \right\} \psi_i ds = 0 \end{aligned} \quad (54)$$

where  $\vec{n} = (n_x, n_y)$  is the unit normal vector along each segment of  $\partial\Omega_F$ . The boundary conditions:

$$\phi_{,y}^{n+1} = (1 + \phi_{,x}^{n+1}) \frac{df}{dx} \quad \text{for } (x, y) \text{ in } \partial\Omega_A \quad (55)$$



and

$$\phi_{,y}^{n+1} = 0 \quad \text{for } (x,y) \text{ in } \partial\Omega_0 \quad (56)$$

are substituted into the boundary term of eq 54. Since  $\phi$  is specified along  $\partial\Omega_{FF}$ , then  $\psi_i$  is taken to be zero there.

Equation 54 is piecewise integrable over the discretized half-space providing  $\phi$  and  $\psi_i$  are at least continuous functions across the inter-element boundaries. Within each element the solution can be approximated by

$$\phi(x,y) = N_j(x,y) \phi_j \quad (57)$$

where  $N_j$  are the shape functions and  $\phi_j$  the unknown potential values at the nodes. The shape functions are chosen to satisfy the required continuity of  $\phi$  in the global sense. For Galerkin's method  $\psi_i$  is set equal to  $N_i$ . Thus, all continuity requirements are satisfied to allow eq 54 to be written in elemental form and assembled to obtain the global form. The elemental form of eq 54 is expressed as

$$K_{ij}(\phi^n) \phi_j^{n+1} = f_i \quad (58)$$

Matrix  $K_{ij}(\phi^n)$  is given by the sum of the following five matrices:

$$A_{ij} = (1 - M_\infty^2) \iint_{\Omega_e} N_{i,x} N_{j,x} dx dy \quad (58a)$$

$$B_{ij} = \iint_{\Omega_e} N_{i,y} N_{j,y} dx dy \quad (58b)$$

$$C_{ij}(\phi^n) = -M_\infty^2 \frac{1+\gamma}{2} \phi_K^n \iint_{\Omega_e} N_{K,x} N_{i,x} N_{j,x} dx dy \quad (58c)$$

$$D_{ij} = M_\infty^2 \int_{\partial\Omega_A^*} N_i N_{j,x} \left. \frac{df}{dx} \right|_{y=0^+} dx \quad (58d)$$

$$E_{ij}(\phi^n) = M_\infty^2 \frac{1+\gamma}{2} \phi_K^n \int_{\partial\Omega_A^*} N_{K,x} N_i N_{j,x} \left. \frac{df}{dx} \right|_{y=0^+} dx \quad (58e)$$

Vector  $f_i$  is defined by

$$f_i = \int_{\partial\Omega_A^*} N_i \left. \frac{df}{dx} \right|_{y=0^+} dx \quad (58f)$$

In general  $K_{ij}(\phi^n)$  and  $f_i$  depend upon the shape of the airfoil. The contribution to  $K_{ij}(\phi^n)$  from the airfoil shape comes only from matrices  $D_{ij}$  and  $E_{ij}(\phi^n)$ . These matrices are evaluated only for the first row of elements above the airfoil in the center segment shown in Fig 6. They are zero for all other elements since they come from the global boundary term of eq 54. This boundary term could alternatively be taken to the right-hand side of the equation and treated as a force. The effect of this alteration would be a slightly slower convergence rate caused by replacing  $\phi^{n+1}$  with  $\phi^n$  in the affected terms.

The contribution to  $K_{ij}(\phi^n)$  from matrices  $A_{ij}$ ,  $B_{ij}$ , and  $C_{ij}(\phi^n)$  are independent of the airfoil being considered, since they depend on an integration over the elemental area. This is true only because the tangential boundary condition is imposed along  $y=0^+$ ,

which requires that elements be extended to the  $X$ -axis. If the boundary condition was enforced on the airfoil surface, then the area of elements in the first row of the center segment would be smaller by comparison. Thus, an indirect dependence of the airfoil shape from these elements would be reflected by all the matrices defining

$K_{ij}(\phi^n)$ . The effect of enforcing the boundary condition along  $y = 0^+$  instead of on the airfoil contour, is not critical for thin airfoils as long as element sizes in the  $y$ -direction are larger than the thickness of the airfoil. Since one of the advantages of the FEM is the ability to use relatively large elements to achieve accurate approximations, then element size difficulties should not be critical until thickness ratios become large. For thick airfoils or for arbitrarily shaped bodies the boundary conditions must be satisfied, not on  $y = 0^+$ , but on the surface contour. For these shapes, elements would terminate at the contour and pose no conflict. By way of comparison, some investigators (Refs 10, 40) using finite difference methods and small grid sizes satisfy the tangential condition along  $y = 0^+$ .

Several different types of elements and orders of approximation could be used to solve this problem. For example, the higher-order cubic triangular elements used by Chan (Ref 13) would be more than sufficient. Also, linear triangular elements (Ref 7), which provide the lowest permissible approximation, would be adequate since they satisfy the required continuity. In terms of velocities, the linear triangles would give constant velocity elements. In order to get a linear variation in velocity, which is not required, one would have to use quadratic triangular elements. Somewhere between the linear and

quadratic triangular elements are the bilinear rectangles or, in general, the quadrilaterals. Rectangles are normally not very useful except for simple boundary geometries.

For the problem being considered, the boundaries are straight line segments as shown in Fig 6. The boundary segment between the leading and trailing edges of the airfoil is straight only because the tangential boundary condition is satisfied along the chord (i.e.  $y = 0^+$ ). Therefore, rectangles can be used effectively to discretize  $\Omega_F$  everywhere. Rectangles are desirable due to their simplicity, and were chosen for this reason. They are described in Appendix D along with the derivation of elemental equations.

#### Mixed Flow

Reported Convergence Difficulties. Several investigators, who have tried to solve the velocity potential equation using finite element methods, report difficulties with convergence of solution algorithms for transonic flow. Among these are: Chen and Habashi (Ref 12), Chan (Refs 13-16), Ecer (Ref 22), Akay (Ref 24), and Aziz (Ref 23). Divergence of solution algorithms have lead some to believe that Galerkin's method could not be used. Others claim the source of difficulty is the small-disturbance, velocity potential formulation of the problem and suggest that alternative formulations be tried. However, Akay (Ref 24) reports convergence difficulties with finite element solutions of the total velocity potential equation. It should be noted that convergence problems also occur when finite difference methods are used (Refs 33, 34, 40). To insure that solution algorithms converge, special difference operators have been developed. A different operator

may be used at each grid point depending on whether the point is considered to be an elliptic, parabolic, hyperbolic, or shock point. Divergence of solution techniques for more classical methods, such as the Rayleigh-Janzen Method (Refs 29, 30), also occurs when transonic flow develops.

The convergence problems reported by other investigators for transonic flow are also observed when the methods described in this study are used to solve the transonic problem. Solution techniques converge quickly as long as the flow remains subsonic everywhere in  $\Omega_F$ . When transonic flow occurs (i.e. a small supersonic bubble appears in the flow), solution techniques which are suitable for subsonic flow (i.e. an elliptic problem) do not converge at all. These conclusions are supported by solution results presented and discussed in Chapter VI. Convergence difficulties are caused by the mixed character of the flow which results when the governing differential equation changes type from elliptic to hyperbolic in the supersonic region. To overcome convergence difficulties an adjustment is needed in the finite element equations for elements in the supersonic region. The purpose for this adjustment is to account for the proper zones of influence in the supersonic region where the equation is hyperbolic. Finite element formulations of elliptic equations work quite well, but those same formulations applied to hyperbolic equations will not work.

Formulation Adjustments. Other investigators have tried various techniques to alter their finite element formulations for mixed or transonic flow. These techniques are briefly described, and all were tried in the present study. The first technique was developed by Chan, Brashears, and Young (Ref 23). They altered their finite element

equations for elements in the supersonic zone during the assembly procedure. Before the local stiffness matrix was assembled the  $\phi_{xx}$  coefficient,  $C = 1 - M_\infty^2 - M_\infty^2 (1 + \gamma) \phi_x$ , was calculated at each node. If  $C$  was negative at all nodes in the element, then the rows in the stiffness matrix corresponding to the downwind influence were ignored in the assembly process. By zeroing out the appropriate rows in the elemental stiffness matrix the downwind influence on the solution at upwind nodes was blocked. Chan's technique appeared to work in conjunction with the least squares formulation that he used.

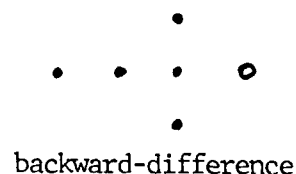
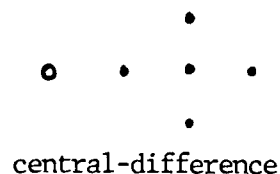
The second technique was developed by Akay, Ecer, and Utku (Ref 24). For the iterative solution procedure they chose, the stiffness matrix was a function of the perturbation velocity squared. During the iterative process, if any element  $e$  was inside the supersonic zone, then the velocity term denoted by  $q_e^2$  was replaced by

$$q_e^2 \rightarrow (1 - \Theta) q_e^2 + \Theta q_u^2 \quad (59)$$

Velocity  $q_u$  is the velocity in the element on the upstream side of element  $e$ . The constant  $\Theta$  is the upwinding coefficient which was taken to be between 0.2 and 0.3. According to Akay, this technique prevented the iterative solution algorithm from diverging; however, it did not produce convergence in the sense of eq 45. Instead, the solution for the potential function oscillated about some solution. In addition to Akay's own technique, he also tried Chan's upwinding method, which caused the solution algorithm to diverge immediately upon application.

Four additional upwinding techniques were tried, three of which are briefly described below. The first is an element sliding technique which is implemented during the assembly process. As the elements are assembled, a check is made to see if the velocity at all element nodes is supersonic. If the element is inside the supersonic region, then it is slid upstream before assembly. Thus, the influence on the unknown nodal values associated with that element comes from the region upwind of the nodes.

The second technique is a nodal sliding method which is implemented after partial assembly of the elements in the supersonic bubble. This method closely resembles the upwinding or backward-difference methods used in finite difference analyses. Before assembling any elements, a check is made to identify which nodes are contained within the supersonic bubble. If a node is in the bubble then all elements which have that node in common are identified. Next, a portion of the stiffness matrix, which comes from the  $X$ -derivative terms, is assembled for the identified elements. After this portion of the assembly process is completed, then the coefficients in the partially assembled global equations are slid upwind one position. This procedure is analogous to taking the first-order, five-point, central-difference star and sliding the horizontal coefficients upwind one step to get the backward-difference operator as illustrated below



The third upwinding technique was only briefly examined. It was taken from a suggestion by Christie (Ref 37), and could prove to be effective if developed properly. For this technique, the weight functions are chosen to be different than the shape functions for all elements inside the supersonic bubble. The idea is to give more weight (i.e. more influence) to the upwind half of the element than to the downwind half. For the technique tried, upwinding was done only in the  $X$ -direction. Weight functions were taken to be  $\Psi_i = N_i + \alpha p(x)$  for  $i$  equal to an upwind node, and  $\Psi_i = N_i - \alpha p(x)$  for  $i$  equal to a downwind node. The function  $p(x)$  is chosen to be zero at the nodes. This technique was tried for  $p(x) = X(X-2a)$  and  $\alpha = 1$ , but it was not explored thoroughly and warrants further study.

New Upwinding Technique. A new upwinding technique was developed in this study. It is more intuitive than analytical in nature, although it has an analytical foundation. It is not as elegant an idea as the previous one, but it is simple to use, and provides accurate approximations of pressure distributions for transonic flows. For this and other reasons it may be preferred to the previous method. It is well known that picking weight functions which are different from the shape functions may lead to significant error (Ref 37).

The new method was developed by modifying the finite element formulation of the nonlinear term, which is the term that is responsible for the mixed character of the flow for subsonic, free-stream Mach numbers.

Recall that the nonlinear term in eq 51 was written iteratively as  $\phi_{,x}^n \phi_{,x}^{n+1}$ . For iteration  $(n+1)$  this term is relaxed by replacing it with the expression



$$\phi_{,x}^n \phi_{,x}^{n+1} \rightarrow R \phi_{,x}^n \phi_{,x}^{n+1} + (1-R) \phi_{,x}^n \phi_{,x}^n \quad (60)$$

The relaxation coefficient  $R$  takes the range of values:  $0 \leq R \leq 1$ .

The last term in eq 60 can be taken to the right-hand side of the governing equation and treated as a force computed from the previous iteration. Thus, eq 51 written in iterative form becomes

$$\begin{aligned} & \left[ (1-M_\infty^2) \phi_{,x}^{n+1} - M_\infty^2 \frac{1+\gamma}{2} R \phi_{,x}^n \phi_{,x}^{n+1} \right]_{,x} + \phi_{,yy}^{n+1} \\ & = \left[ M_\infty^2 \frac{1+\gamma}{2} (1-R) (\phi_{,x}^n)^2 \right]_{,x} \end{aligned} \quad (61)$$

When  $R=1$ , the nonlinear term is not relaxed at all. For  $R=0$ , the nonlinear term is totally relaxed (i.e. it is taken to the right-hand side of the equation and treated as a force that depends upon the previous iteration of the solution). For values of  $R$  between 0.0 and 1.0 a mixture of these two extremes exists. The sole modification of relaxing the nonlinear term is not sufficient to make the solution algorithm converge in the sense of eq 45. It would be difficult to imagine that a hyperbolic equation could be solved by merely solving a sequence of elliptic (Poisson) equations. The ideas of domain of dependence and range of influence from the theory of differential equations must be included into the modification process. As discussed previously the sign of the  $\phi_{,xx}$  coefficient will determine whether the governing equation is elliptic or hyperbolic. Inside the supersonic bubble that appears for transonic flow the coefficient is negative and the equation is hyperbolic. Outside of this bubble the

coefficient is positive and the equation is elliptic. For elliptic differential equations the domain of dependence is the entire domain of the problem, but for hyperbolic equations the domain of dependence at some given point is confined to the region within the backward cone defined by the characteristic curves. Consequently, the solution at the given point is influenced only by the solution at points in the backward cone and not by the solution at any other points in the domain. Likewise, the solution at the given point will influence the solution only for points in the forward cone, also defined by the characteristic curves.

Without getting involved with the method of characteristics, the above described concepts can be incorporated into the modification procedure being discussed. For elements inside the supersonic bubble the nonlinear term is relaxed as described. This means that forces which depend upon the solution are applied at each of the element nodes. However, the solutions at upwind nodes cannot be influenced by the solution at downwind nodes; therefore, the forces acting at downwind nodes are set equal to zero. In addition, the solution in the element cannot depend on forces applied at upwind nodes, when those forces are determined from an integration over the entire area of the element. At any point in the element the solution should depend on the potential only in a backward cone defined by the characteristic curves. Thus, the upwind forces must be reduced in magnitude by some factor. One way to represent this numerically is to multiply the relaxed term  $(1-R)(\phi_x^n)^2$  by the factor  $U$  where  $0.0 \leq U \leq 1.0$  at upwind nodes. Thus, the iterative Galerkin form of the governing equation for hyperbolic elements becomes

$$\begin{aligned}
& \iint_{\Omega_{e,hyp}} \left\{ \left[ (1-M_\infty^2) \phi_{,x}^{n+1} - M_\infty^2 \frac{1+\gamma}{2} R \phi_{,x}^n \phi_{,x}^{n+1} \right]_{,x} + \phi_{,yy}^{n+1} \right\} N_i dA \\
& = U(1-R) M_\infty^2 \frac{1+\gamma}{2} \iint_{\Omega_{e,hyp}} (\phi_{,x}^n)^2_{,x} N_i dA
\end{aligned} \tag{62}$$

where  $U$  is given by

$$U = \begin{cases} 0.0 & \text{to } 1.0 & \text{at upwind nodes} \\ 0.0 & & \text{at downwind nodes} \end{cases}$$

In actual implementation eq 62 is integrated by parts as discussed previously. The elemental equations expressed by eqs 58 a-f, and referred to as equations for elliptic elements, are modified by the upwinding procedure for hyperbolic elements as follows:

$$(A_{ij})_{hyp} = (A_{ij})_{ell} \tag{63a}$$

$$(B_{ij})_{hyp} = (B_{ij})_{ell} \tag{63b}$$

$$C_{ij}(\phi^n)_{hyp} = R C_{ij}(\phi^n)_{ell} \tag{63c}$$

$$(D_{ij})_{hyp} = (D_{ij})_{ell} \tag{63d}$$

$$E_{ij}(\phi^n)_{hyp} = R E_{ij}(\phi^n)_{ell} \tag{63e}$$

$$(f_i)_{hyp} = (f_i)_{ell} + (g_i + h_i)_{hyp} \tag{63f}$$

The last two terms in eq 63f are forces resulting from the upwinding procedure. They are given by

$$(g_i)_{hyp} = - U(1-R) C_{ij}(\phi^n)_{ell} \phi_j^n \quad (63f)$$

$$(h_i)_{hyp} = - U(1-R) E_{ij}(\phi^n)_{ell} \phi_j^n \quad (63h)$$

The relaxation and upwinding parameters ( $R, U$ ) were investigated by numerical experiment for two reasons. First, an estimate was needed on the range of values for which solution algorithms converge. Secondly, the "best possible" combination of parameter values for a given Mach number was needed to solve for realistic pressure distribution on the airfoil. The effect these parameters have on convergence properties and on airfoil pressure distributions is presented in Chapter VI.

In general, the idea behind the upwinding method is to modify the formulation just enough to capture the physics of the problem, within the realm of the assumptions.

For a given airfoil shape and Mach number, the values of  $R$  and  $U$  are selected by an iterative method. First, upper bounds (i.e. values above which solutions will diverge) and lower bounds (i.e. values below which solutions will not diverge) are estimated. The idea is then to determine the lowest upper bound for both  $R$  and  $U$  which permits the solution algorithm to converge. The old, familiar, and perhaps inefficient interval-halving method was used for this procedure. Further discussion concerning this procedure is given in Chapter VI.

## V Results -- Flow Over a Circular Cylinder

Finite element solutions are presented for flow over a unit circular cylinder for Mach numbers within the range of  $0 \leq M_{\infty} \leq M_{cr}$ . These solutions are compared with exact solutions for incompressible flow and with solutions obtained from other approximate methods for compressible flow. The problem of incompressible flow without circulation was solved using three different elements representing one nonconforming and two conforming approximations. The two conforming elements were used to solve the incompressible problem with circulation. The compressible problem was solved using the new conforming element.

### Incompressible Flow Without Circulation

Geometry. The entire flowfield was discretized as shown in Fig 5 for a typical set of discretization parameters. Only a quarter of the field is necessary because of symmetry, but since the addition of circulation requires the entire field, then it was discretized for all of the incompressible problems. A computer subroutine was written to automatically discretize the field from the parameters ( $R_{FF}$ ,  $N_R$ ,  $N_S$ ).  $R_{FF}$  is the radius of the farfield boundary,  $N_R$  the number of element rings, and  $N_S$  the number of angular sectors in each ring (see Fig 5).

The location of the outer boundary depends upon the boundary condition imposed there. When the farfield expression given by eq 40 is used,  $R_{FF}$  can be as close as 3 radii from the cylinder. If other boundary conditions are used, for example  $\phi_{FF} = 0$ , then  $R_{FF}$  has

to be extended beyond 10 radii before the velocity profile on the cylinder surface is unaffected. The boundary condition  $\phi_{FF} = 0$  does not produce adequate velocity distributions when farfield boundaries are located within 10 radii of the surface. This behavior was expected and affects the velocity distribution significantly in the region of maximum velocity. For this reason, and to preclude the necessity of considering large flow domains, the farfield boundary condition given by eq 40 is used exclusively.

Comparison of Three Sector Elements. Before examining the effect of element refinement on convergence, a comparison among the three finite element approximations and the exact solution is given. The solutions for a coarse flowfield discretization of only 12 elements (3 rings and 4 sectors) are shown in Fig 7 for the three trial functions described in Chapter III. The nonconforming approximation appears to be better than either of the other two conforming ones for the discretization used. The nonconforming approximation obtained from this coarse discretization actually compares well with solutions obtained from the other two conforming elements when a more refined discretization is used. One might conclude, on the basis of these results and observations, that sector element (1) is the most desirable element; however, this choice is a bad one. For the two conforming elements, the approximations improve when the discretization is refined, but they do not improve for the nonconforming element. In fact, the error in the approximations becomes greater when the discretization is refined.

One reason for the decline in accuracy for the nonconforming element is due to the error caused by not satisfying the required

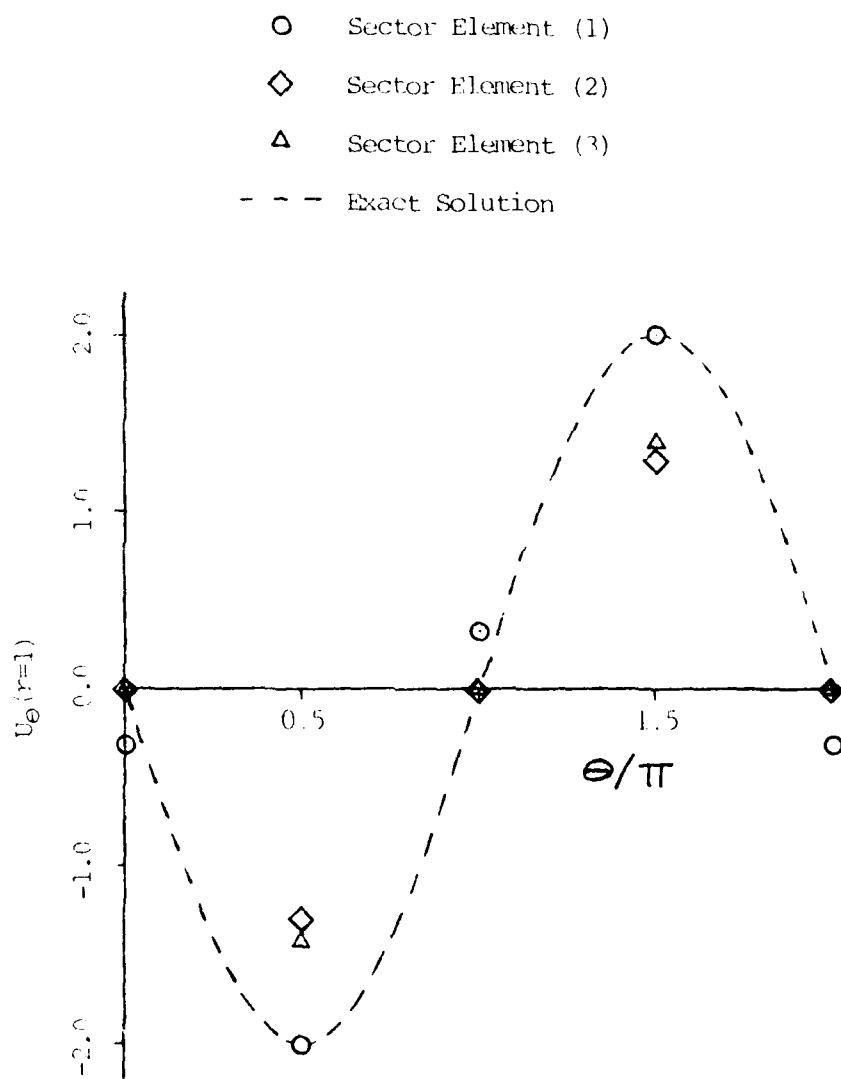


Figure 7 - Comparison of Tangential Velocity Distributions for Incompressible Flow Over a Circular Cylinder

continuity of potential across inter-element boundaries. For coarse discretizations, which mean relatively few such boundary lines, the error is comparatively small. However, as the discretization is refined additional error occurs and the solution degenerates. Further refinement compounds the problem which leads to the rejection of sector element (1), except for the most coarse discretizations. There are formulation adjustments which can be made to improve the nonconforming solutions significantly for finer discretizations. However, the resulting solutions are not as good as those obtained from the conforming elements and these adjustments will not be discussed.

Discretization Effects. Tangential, velocity distributions  $v_\theta(r=1, \theta)$  obtained from each conforming element are compared with the exact solution as shown in Figs 8 and 9. The four finite element solutions in each figure are for four different discretizations of  $\Omega_F$ . Additionally, these discretizations represent refinement of the element angular size parameter  $\beta$  for a fixed value of the element radial size parameter  $\alpha$ . These solutions are presented to show the difference in convergence properties between the two conforming elements as a function of discretization refinement. By comparing the solutions in Figs 8 and 9 with the exact solution it appears that refinement of  $\beta$  alone is sufficient to achieve convergence with element (3), the new element. It also appears that refinement of  $\beta$  alone is not sufficient to achieve convergence with element (2), the bilinear element. For each discretization the velocity distribution obtained with element (3) is closer to the exact distribution than the distribution obtained from element (2). These differences are due to the diverse nature of the trial function for each element.



Circular Cylinder.  $M_\infty = 0$

Symbol	Number of Angular Divisions
$\Delta$	4
$\square$	8
$\diamond$	16
$\circ$	32
- - -	Exact Solution

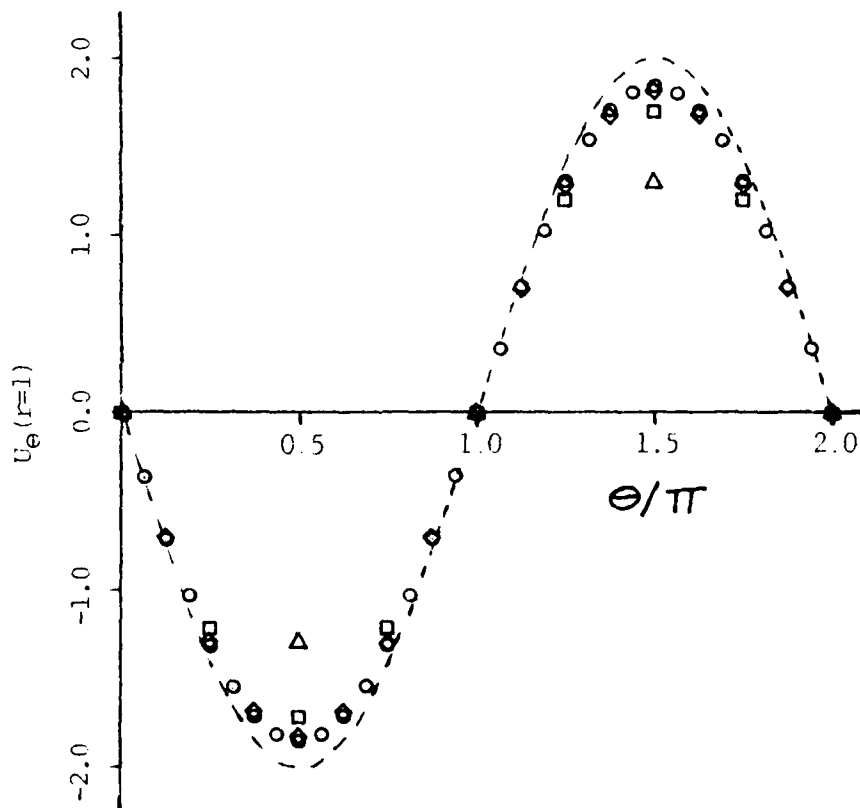


Figure 3 - Convergence of Tangential Velocity for Sector Element (2) for Refinement of  $\beta$  Alone

Circular Cylinder,  $M_\infty = 0$

Symbol	Number of Angular Divisions
$\Delta$	4
$\square$	8
$\diamond$	16
$\circ$	32
- - -	Exact Solution

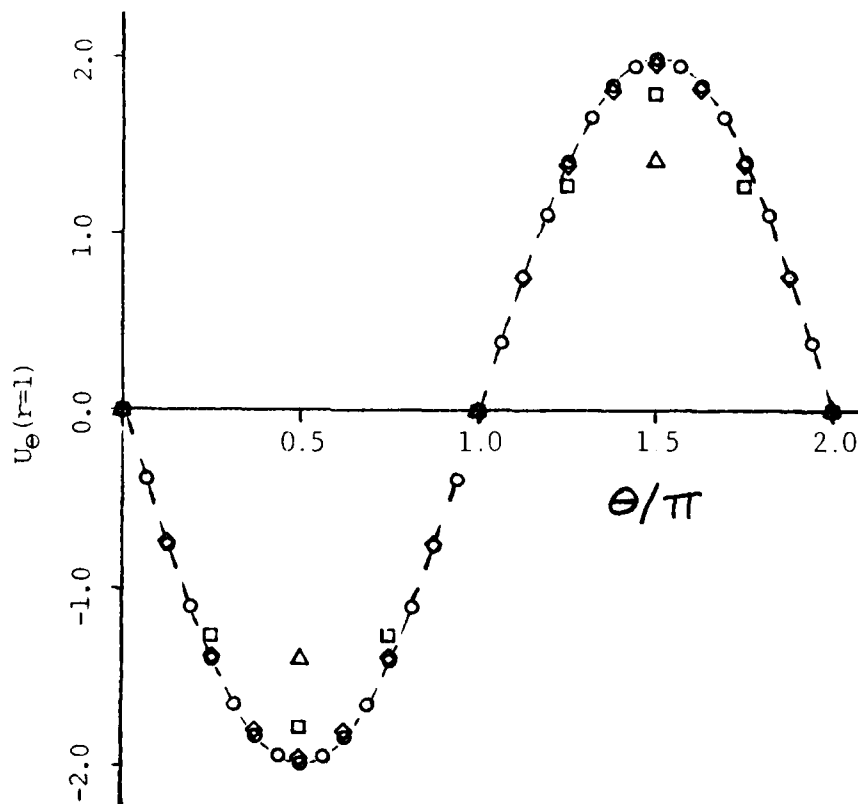


Figure 9 - Convergence of Tangential Velocity for Sector Element (3) for Refinement of  $\theta$  Alone

To further illustrate the difference in convergence properties between the two conforming elements, consider two variations in the discretizations of  $\Omega_F$ . First, the effect of refining only the radial parameter  $\alpha$  is examined. The number of angular sectors and location of the farfield boundary remain fixed. Table I shows the effect on the solution of the tangential velocity at  $\theta = \pm \pi/2$  for refinement of  $\alpha$ . The points  $\theta = \pm \pi/2$  are selected because the point-wise error there is a maximum as shown in Figs 8 and 9.

Table I - Point-wise Error for Conforming  
Sector Elements with Radial Refinement\*

Number of Rings	Outer Radii of Ring						$U_\theta(1, \pi/2)$ Per Cent Error	
	1	2	3	4	5	6	Element (3)	Element (2)
3	2.0	4.0	7.8				0.95	4.46
4	1.4	2.0	4.0	7.8			0.95	2.49
5	1.4	2.0	2.8	4.0	7.8		0.95	1.99
6	1.4	2.0	2.8	4.0	5.6	7.8	0.95	1.87
4	2.0	2.8	4.0	7.8			0.95	3.98
4	2.0	4.0	5.6	7.8			0.95	4.35

\* Number of Angular sectors equals 16.

The percent error is based on the exact solution and is presented for both conforming elements. First, note that the error in velocity  $U_\theta(1, \pi/2)$  for sector element (3) is constant at 0.95% regardless of

the number of rings or the relative size arrangement of those rings. Thus, radial refinement is not required, and does not improve the results obtained with this element. The reason for this behavior is due to the functional dependence of  $r$  in the trial function. Since the exact solution behaves as  $\cos\theta/r$ , then the trial function contains the correct form for the radial variable. This behavior suggests interesting possibilities for other types of problems which will be discussed in more detail in a later section on recommendation for further work. Secondly, note that refinement of parameter  $\alpha$  for sector element (2) significantly affects the solution. For this element the radial dependence of  $r$  in the trial function is different from the exact form; therefore, to achieve convergence, refinement of  $\alpha$  is necessary.

Three other interesting observations can be made about element (2) from the data in Table I. First of all, radial refinement alone will not drive the error to zero. For a given number of angular divisions there is a certain number of rings beyond which the solution does not get closer to the exact one. This behavior is detected by observing the rate at which the error decreases as more rings are added. Secondly, if only one additional ring is to be added to some base-line discretization (represented by 3 rings in Table I) then the location of that ring is crucial. For example, approximately 44% reduction in error is achieved by dividing the first ring into two rings of proportional thickness (as illustrated by line two in the table). Similar divisions of the second and third rings result in approximately 11% and 2% reduction, respectively (as illustrated by the last two lines in the table). Thirdly, for all of the discretizations shown, the

error obtained from the new element, element (3), is significantly less than from the bilinear element, element (2).

Next, the effect of refining only the angular size parameter  $\beta$  is examined. Refinement of this parameter is required of both conforming elements to achieve convergence. The number of rings and location of the farfield boundary remain fixed. The tangential velocity at  $\theta = \pm\pi/2$  is presented in Table II for different angular divisions.

Table II - Point-wise Error for Conformal  
Sector Elements with Angular Refinement\*\*

Number of Sectors	$U_\theta(1, \pm\pi/2)$		Percent Error	
	Element (3)	Element (2)	Element (3)	Element (2)
4	1.7038	1.6484	14.81	17.58
8	1.9244	1.8569	3.78	7.16
16	1.9810	1.9108	.95	4.46
32	1.9952	1.9244	.24	3.78
48	1.9979	1.9269	.11	3.66

\*\*Number of rings equals 3.

The error in velocity at  $\theta = \pm\pi/2$  for the new element can be shown to decrease by  $O(\beta^2)$ . The bilinear element converges rapidly for a couple of refinements in  $\beta$ , but then a point is reached where further refinement produces very little change of results. This same behavior was observed in Table I for radial refinement. Thus, for element (2) both the radial and angular size parameters must be

refined simultaneously with some other parameter such as element aspect ratio held constant.

#### Incompressible Flow With Circulation

Most of the discretization questions discussed for flow without circulation also apply when circulation is present. The required far-field boundary location, the effect of element refinement, and the characteristic differences between the two conforming elements are unchanged by the addition of circulation. The only remaining discretization question that needs to be answered is whether the relative arrangement of elements about the stagnation point has an impact on the value of circulation predicted.

Circulation. In general, the value of circulation obtained from the solution depends upon the relative location of the stagnation point within the element containing it. To quantify this statement Table III presents the error in predicted circulation for a number of discretizations. The data in this table was obtained with the use of element (3) with the farfield boundary located at  $R_{FF}=5$  and stagnation point at  $\theta = -\pi/6$ .

Table III - Error in Circulation for Sector Element (3)  
for Stagnation Point  $\theta = -\pi/6$

Angular Sectors	Number Element	Number Nodes	% Error in Circulation
8	16	27	11.6
12	24	39	24.0
16	32	51	5.5
20	40	63	4.6
24	48	75	11.6
32	64	99	2.9
40	80	123	2.2

The error in circulation appears to behave irratically as the number of angular sectors is increased. One would expect the error to decrease as the parameter  $\beta$  is refined. The reason for the erratic behavior is due to the relative difference in locations of the stagnation point within the appropriate stagnation element as  $\beta$  is refined. When location differences are accounted for, then the error in circulation does decrease as  $\beta$  is refined. For example, for angular divisions of 12 and 24 the stagnation point lies on a node. Doubling the number of angular divisions from 12 to 24 reduces the error in circulation by approximately 50%; although, the magnitude of error is greater than for solutions with fewer angular divisions (i.e. larger elements). Also, doubling the number of angular divisions from 8 to 16 and again to 32 shows an error reduction of about 50% for each doubling. The same observation holds true for the division from 20 to 40 sectors. So, one may wonder, what causes the erratic behavior?

A search was made to determine if an optimum point exists within the stagnation element such that the error in circulation is minimal. Such a point was found to be the angular centroid of the element. Once the stagnation point is established, then the flowfield should be discretized to permit the stagnation point to be located at the angular centroid of the stagnation element. For instance, in order for a stagnation point at  $\theta = -\pi/6$  to occur at the proper location in the element, either 6, 18, or 30 angular divisions should be used. Table IV gives the results from both conforming elements using these angular divisions and 4 rings of elements.

Table IV - Error in Circulation for Conforming Sector Elements with Stagnation Point  $\theta = -\pi/6$  Located at the Optimum Point.

Angular Sectors	Number Nodes	% Error in Circulation	
		Element (3)	Element (2)
6	28	0.0144	3.797
18	95	0.0080	0.597
30	155	0.0032	0.597

It is readily apparent by comparing the results presented in Tables III and IV, that the error obtained for circulation strongly depends on where the stagnation point is located in the stagnation element. The error is maximum when the stagnation point coincides with a node, and it is minimum when the point lies half way between two nodes. It is also apparent that for a given discretization the new element provides by far the best approximation, although acceptable results are obtained



from the bilinear element for the coarse discretizations presented.

Velocity Distribution. Figures 10 and 11 give velocity distributions obtained from each of the conforming elements for the discretizations presented in Table IV. The exact solutions are plotted for comparison purposes. Accurate estimates of the velocity profile are achieved whenever the circulation can be predicted correctly.

### Compressible Flow

Iterative Algorithm. The iterative solution algorithm for constant coefficients defined by eq 44 converged for subsonic flow and even for flows where the local Mach number exceeded one. It is believed that a minor disagreement between the onset of transonic flow and the simultaneous occurrence of a change in the differential equation from elliptic to hyperbolic, accounts for the convergence for slightly supercritical flow. Since the small-disturbance equation is not totally applicable for compressible flow over a cylinder, and since it is locally linearized by constant local coefficients, then it does not change types at exactly the same  $M_\infty$  for which the local Mach number exceeds unity. The local Mach number must exceed unity to the extent that an element becomes supersonic (engulfed within the supersonic bubble) before the equation changes types. The occurrence was created by formulation assumptions and would not occur if the nonlinearity were treated in a more exact manner. When the differential equation for one or more elements becomes hyperbolic the iterative solution diverges. A few reported "upwinding" algorithms were attempted, but none proved successful and the attempt was abandoned for the cylinder. The new "upwinding" technique described for the airfoil was not tried and may

Sector Element 2

Stagnation Point =  $-\pi/6$

Angular Divisions = 18

$M_\infty = 0$

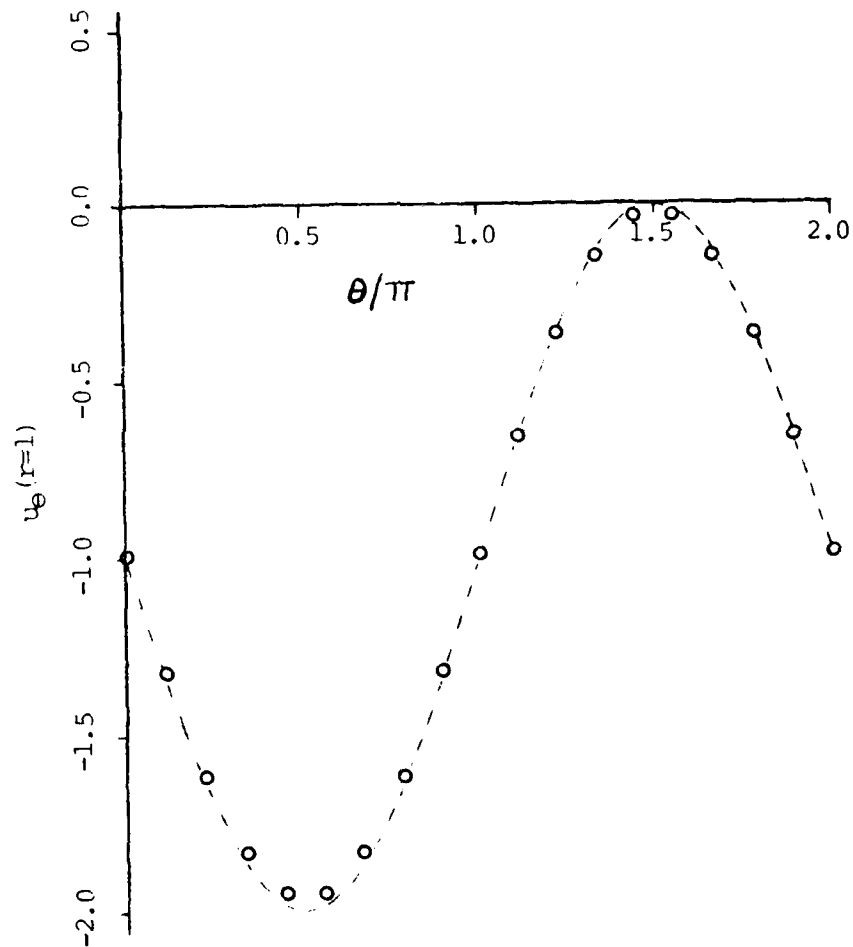


Figure 10a - Perturbation Velocity Distribution from Sector Element (2) for Discretization (2), Table IV

Sector Element 3

Stagnation Point ( $\theta = -\pi/6$ )

Angular Divisions = 18

$M_\infty = 0$

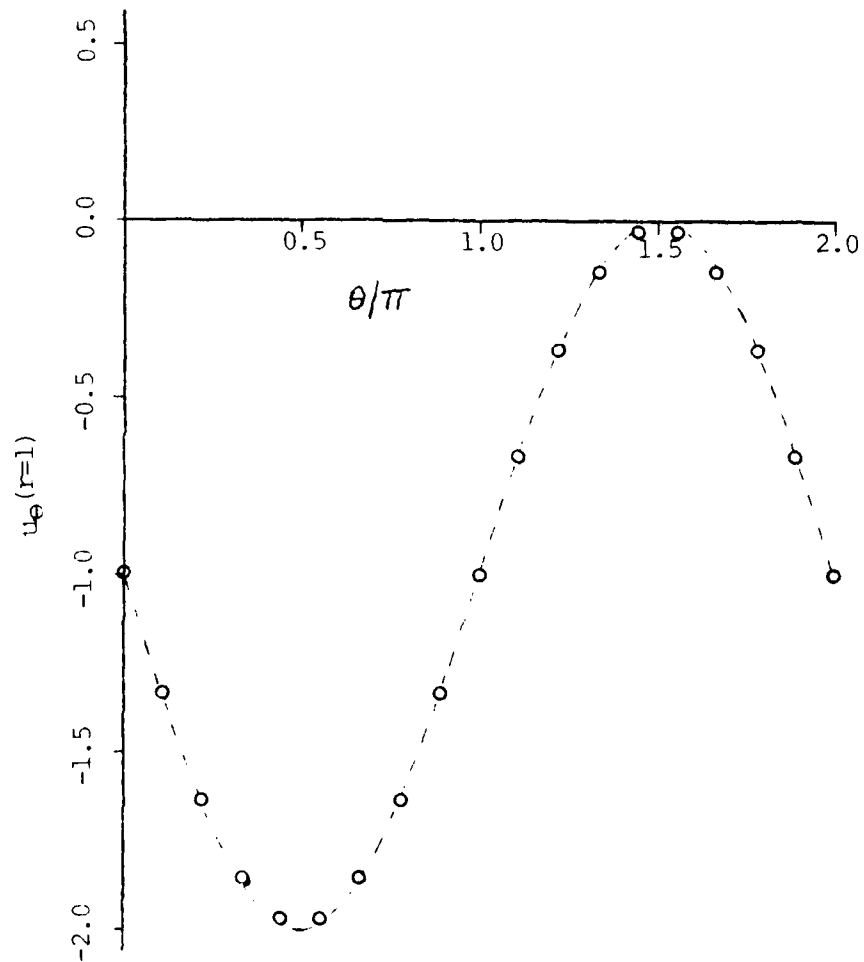


Figure 10b - Perturbation Velocity Distribution from Sector Element (3) for Discretization (2), Table IV

Sector Element 2

Stagnation Point ( $\theta = -\pi/6$ )

Angular Divisions = 30

$M_\infty = 0$

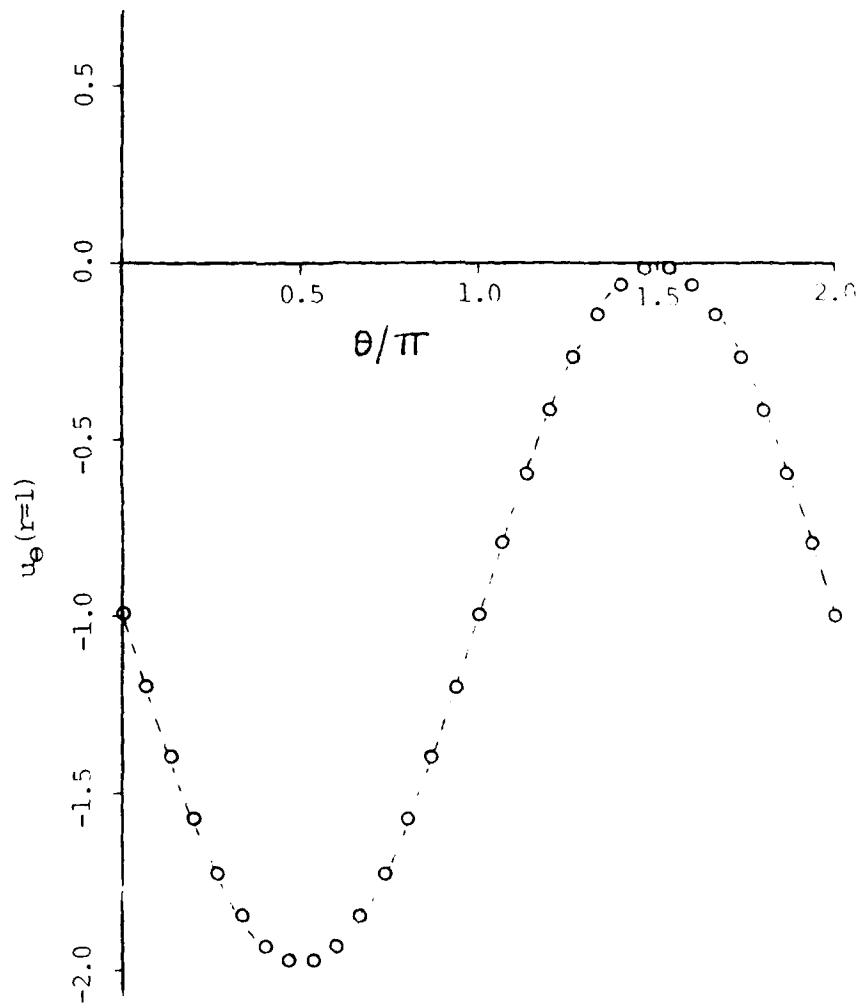


Figure 11a - Perturbation Velocity Distribution from Sector Element (2) for Discretization (3), Table IV

Sector Element 3

Stagnation Point ( $\theta = -\pi/6$ )

Angular Divisions = 30

$M_\infty = 0$

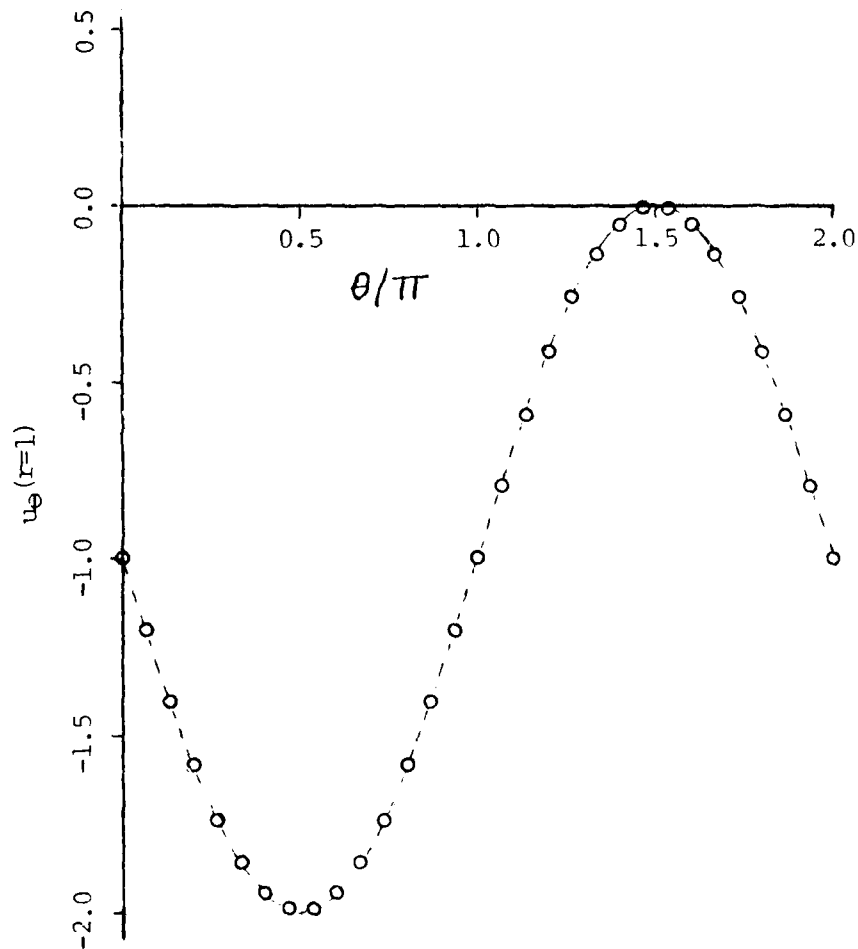


Figure 11b - Perturbation Velocity Distribution from Sector Element (3) for Discretization (3), Table IV

prove useful for transonic flows.

Critical Mach Number. The critical Mach number  $M_{\infty} = 0.403$  was predicted for a discretization of 64 elements with 80 nodes. This value compares well with that obtained by Imai (Ref 30), who used a Janzen-Rayleigh method of third order. Table V shows a comparison of critical Mach numbers reported by several investigators. Greenspan (Ref 32) used finite difference methods in conjunction with a variational principle. Habashi (Ref 31) used linear triangular elements as discussed in Chapter I.

Table V - Comparison Critical Mach Numbers

Source of Results	$M_{cr}$	% Difference*
This Report	0.403	-0.32
Imai (Ref 30)		
3rd-Order	0.4043	0.00
2nd-Order	0.4090	1.16
1st-Order	0.4206	4.03
Habashi (Ref 31)	0.40-0.42	-1.06 to +3.88
Greenspan (Ref 32)	0.404	-0.07

\* % Difference based upon Imai's 3rd-order approximation.

Velocity Distributions. The velocity distributions for  $M_{\infty} = 0.3$  and 0.4 are presented in Fig 12. Imai's third-order accurate results are presented for comparison purposes. Agreement is good over

approximately 60 degrees of a quadrant. Differences are more pronounced in the neighborhood of  $\pi/2$ . It is in this region that finite element results for smaller elements are not as good as those reported. It is believed that the error resulting from using the small-disturbance equation is responsible for the deterioration when smaller elements are used. Velocity perturbations in this region approach or exceed  $U_\infty$ .

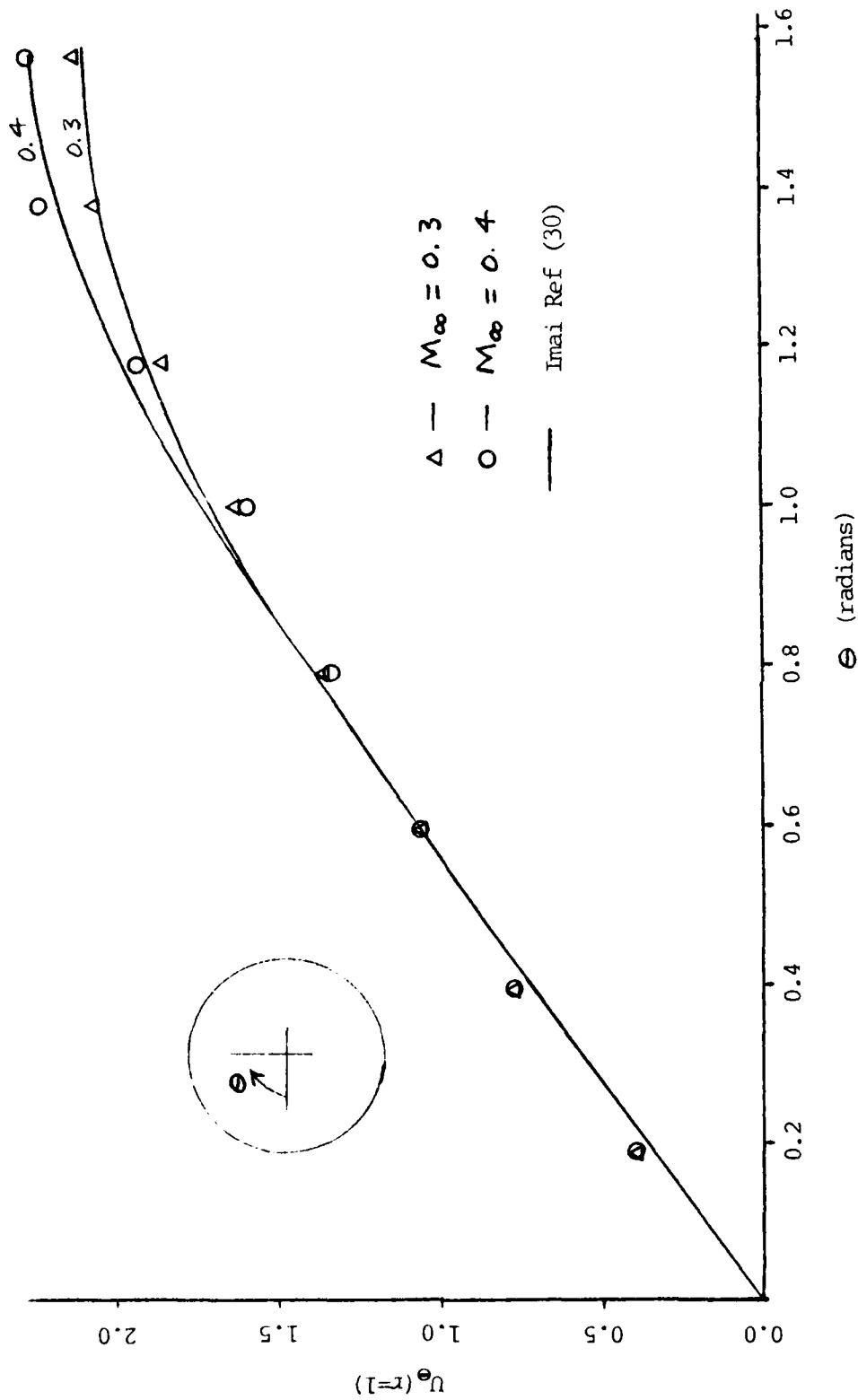


Figure 12 - Tangential Velocity Distribution on the Cylinder Surface Without Circulation (Compressible Flow)



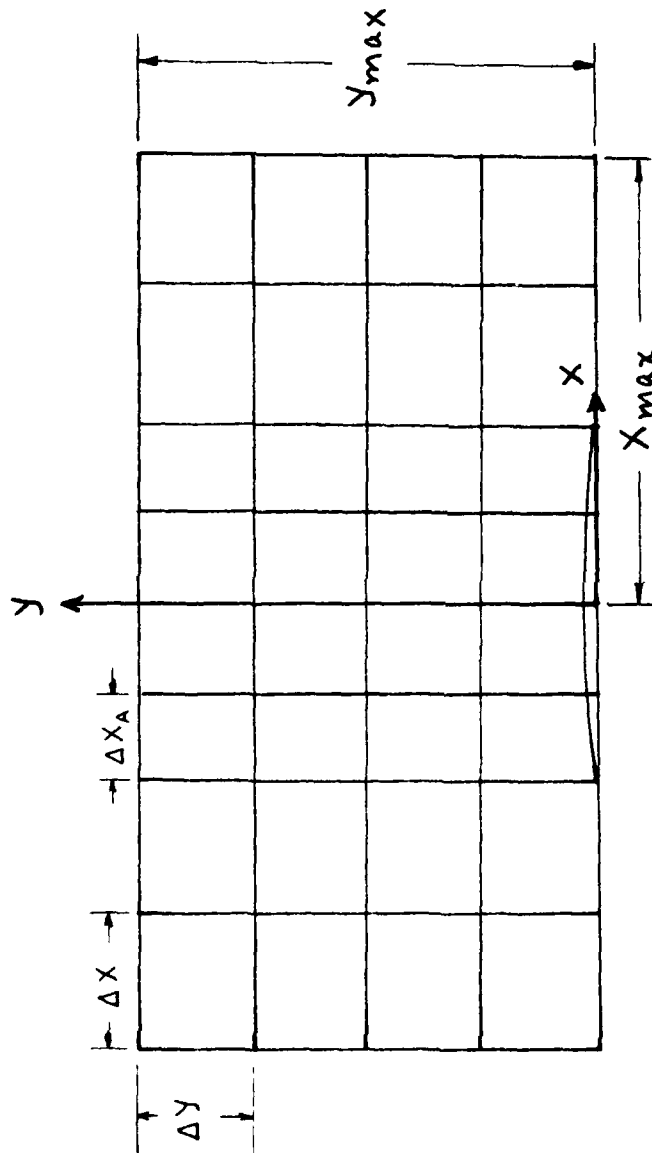
## VI Results of Flow Over a Nonlifting Airfoil

Finite element results are presented for a symmetric, 6%-thick, parabolic-arc airfoil. Pressure coefficient distributions on the upper surface of the airfoil are computed from the finite element solutions of the potential function in domain  $\Omega_F$ . Appendix D contains the computational details of this process. Distributions of the pressure coefficient are presented for a range of Mach numbers from zero up through the transonic, mixed-flow regime. Where possible, these distributions are compared with experimental data and distributions computed from classical thin-airfoil theory, finite difference methods, and other finite element methods. Convergence properties of the iterative solution algorithm are investigated. In addition, convergence properties of the pressure distribution as a function of discretization refinement and location of the farfield boundary are established.

### Discretization Effects

When the flow domain  $\Omega_F$  is discretized several decisions must be made concerning the flowfield size and arrangement of elements. For instance, one must decide where to place the farfield boundary. Should it be relatively close to the airfoil or far from it? How many elements should be used? If smaller elements are needed to improve the accuracy of desired results, then how should the discretization be refined? Should the discretization of the entire flow domain be refined? Will refinement in a subregion of  $\Omega_F$  improve desired results? If so, then which subregion? Answers to these and related questions are given.

Farfield Boundary Location. The farfield boundary location of flow domain  $\Omega_F$  can be characterized by two parameters  $X_{\max}$  and  $Y_{\max}$  as shown in Fig 13. The solution for the airfoil problem as formulated could be obtained for any combination of  $X_{\max}$  and  $Y_{\max}$ . One could select relatively large values for these parameters, but from a computational viewpoint this approach may be prohibitive. One would like to select the smallest possible region to reduce the cost of computing a solution without sacrificing desired accuracy. Thus, lower permissible bounds of  $X_{\max}$  and  $Y_{\max}$  were estimated from a series of solutions obtained from elements of fixed size. First, a baseline solution was computed for a given value of  $X_{\max}$  and  $Y_{\max}$ . By adding additional elements to the outer perimeter of the flow domain a succession of solutions was obtained for increasing values of  $X_{\max}$  and  $Y_{\max}$ . By holding the element size constant and varying only the number of elements used, the effect on the pressure distribution as a function of only the location of the farfield boundary could be assessed. This process was done twice, once to get a bound on  $X_{\max}$  for  $Y_{\max}$  held constant and vice versa. Figures 14 and 15 show the effect on the pressure distributions obtained by this procedure for  $M_{\infty} = 0$ . There is nothing magic about selecting the number 3/2 for the parameter held fixed. Any greater value could be chosen to demonstrate trends. The table in Figs 14 and 15 gives the numerical values of the pressure coefficient at the midchord of the airfoil. From the trend of this data the pressure coefficient converges from below as  $X_{\max}$  and  $Y_{\max}$  are increased. This means that the perturbations velocities  $\phi_x$  converge from above as the farfield boundary is extended. From the data presented in these two figures there appears to be a farfield boundary

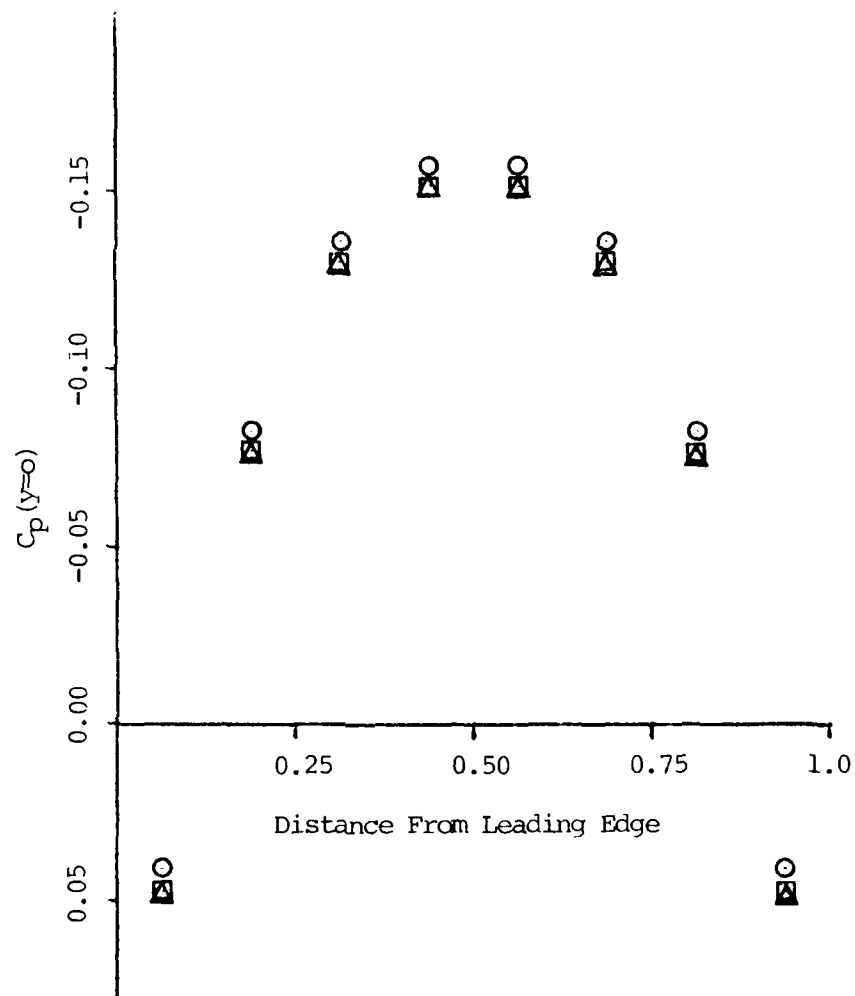


NDX = Number of  $\Delta x$  divisions = 4

NDY = Number of  $\Delta y$  divisions = 4

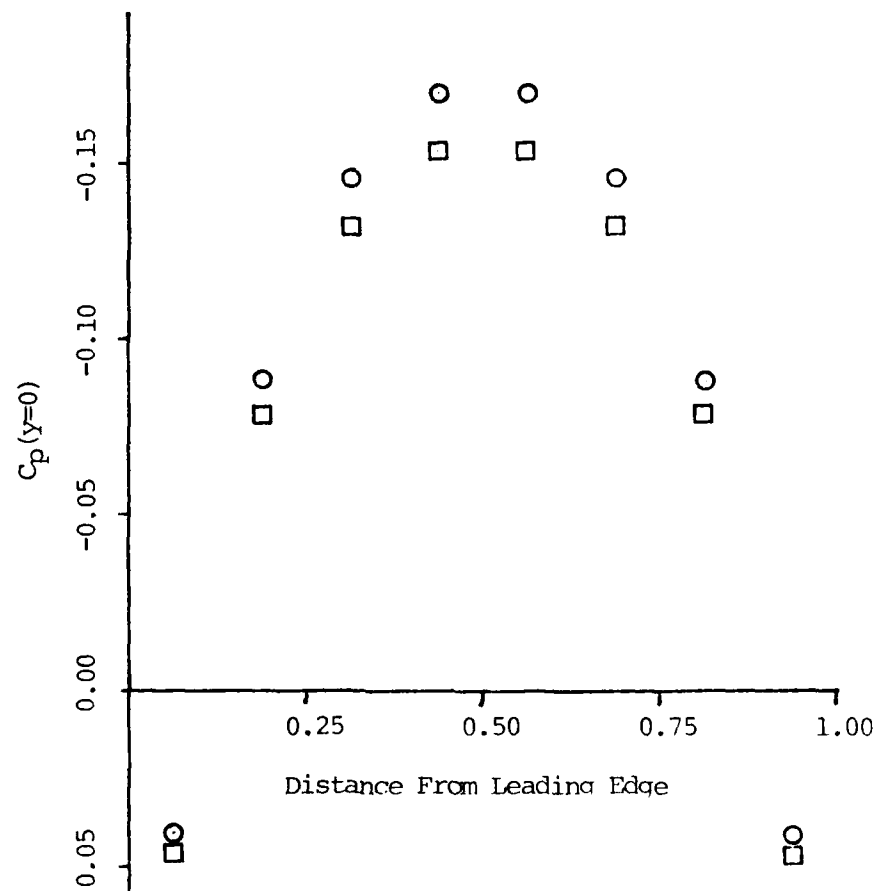
NDXA = Number of  $\Delta x_A$  divisions = 4

Figure 13 - Typical Discretization of Flowfield for Flow Over a Symmetric Nonlifting Airfoil



Symbol	$X_{\max}$	$C_p(0.50)$	Nodes	Elements
⊙	1.0	-0.1568	91	72
□	1.5	-0.1515	119	96
△	2.0	-0.1498	147	120
	2.5	-0.1493	175	144
	3.0	-0.1491	203	180

Figure 14 - Farfield Boundary Location  
Effects for  $Y_{\max} = 1.5$



Symbol	$Y_{max}$	$C_p(0.50)$	Nodes	Elements
○	1.0	-0.1531	85	64
□	1.5	-0.1515	119	96
	2.0	-0.1513	153	128
	2.5	-0.1512	187	160
	3.0	-0.1512	221	192

Figure 15 - Farfield Boundary Location Effects for  $X_{max} = 1.5$

location beyond which pressure distributions are unaffected as the boundaries are extended.

Other descriptions of convergence are provided in Figs 16 to 19 which include the effect of Mach number. The pressure coefficient in these figures is normalized with respect to its converged value. Figures 16 and 17 are for the 1/4-chord point (also 3/4-chord) while Figs 18 and 19 are for the midchord point. Convergence trends are the same at these three points and as demonstrated in Figs 14 and 15 for incompressible flow, the trend is similar for the entire distribution.

What conclusions can be made concerning the farfield boundary location from these figures? First, the curves show that farfield boundaries more than 3 chord lengths from the origin will not appreciably improve results. In fact, farfield boundaries could be chosen closer with little effect. For example, less than 4% error occurs when farfield boundaries are located as close as 3/2 chord lengths. Secondly, the effect of Mach number on the lower bound for  $X_{\max}$  is opposite to that for  $Y_{\max}$ . For a desired degree of accuracy  $X_{\max}$  can be taken smaller while  $Y_{\max}$  should be larger as Mach number increases. This behavior is not surprising in light of the Prandtl-Glauert transformation which stretches the  $y$ -variable as Mach number increases. Thus, perturbations need more distance in the  $y$ -direction to dissipate.

Farfield Boundary Conditions. Associated with the farfield boundary location is the condition imposed there. For nonlifting flow the farfield boundary condition for the potential is given by eq 50 with  $\Gamma = 0$ . The first and last terms of that equation can be expressed

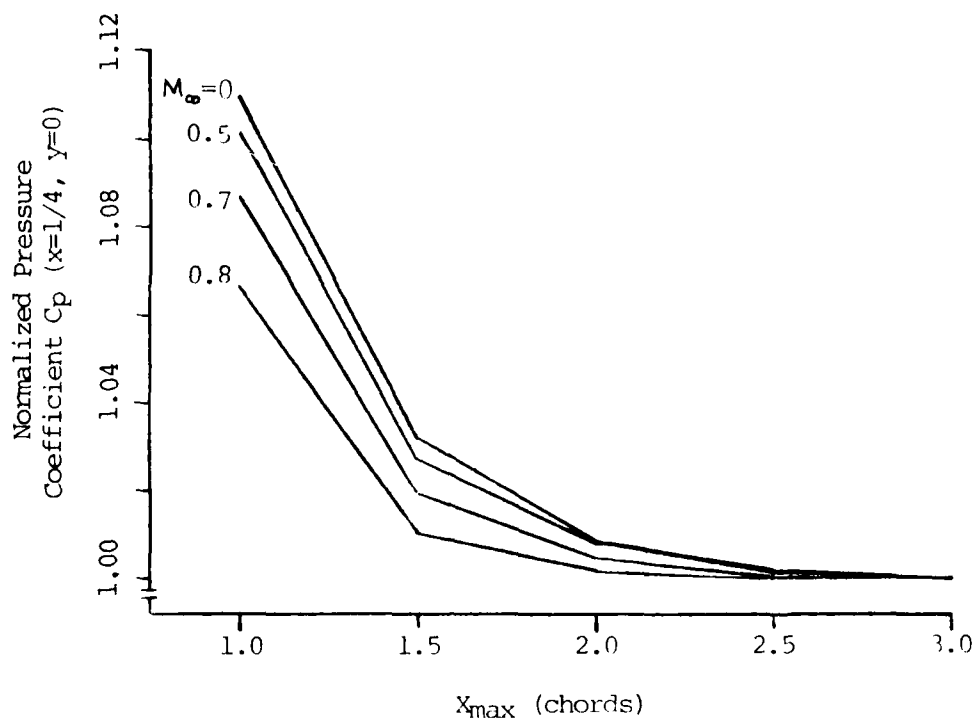


Figure 16 - Convergence Behavior of  $C_p$  (1/4-chord) as a Function of  $M_\infty$  and  $X_{max}$

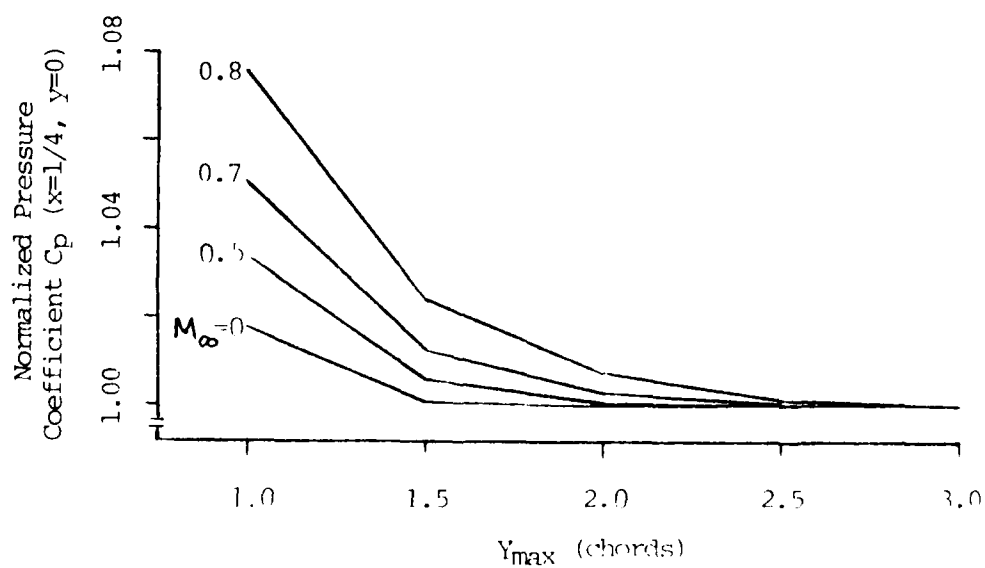


Figure 17 - Convergence Behavior of  $C_p$  (1/4-chord) as a Function of  $M_\infty$  and  $Y_{max}$

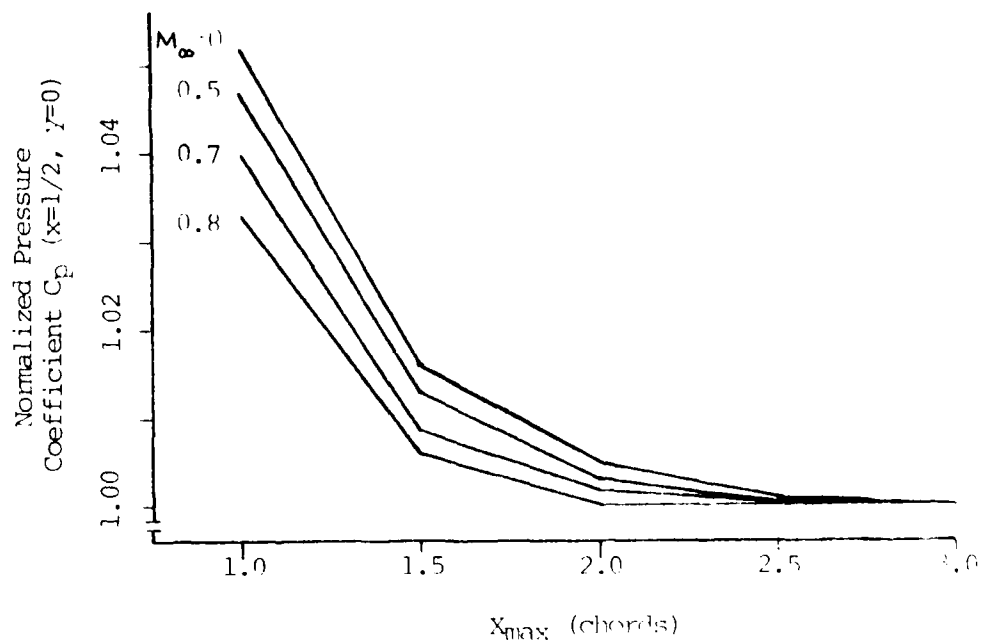


Figure 18 - Convergence Behavior of  $C_p$  (midchord) as a Function of  $M_\infty$  and  $X_{max}$

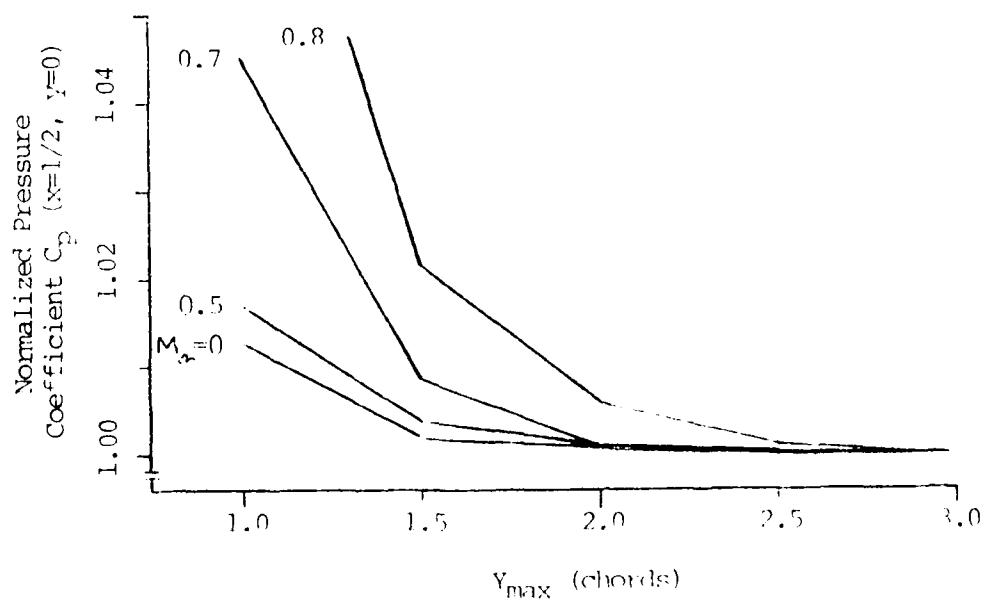


Figure 19 - Convergence Behavior of  $C_p$  (midchord) as a Function of  $M_\infty$  and  $Y_{max}$



as

$$\phi_{FF} = \phi_{FF}^L + \phi_{FF}^{NL} \quad (64)$$

where  $\phi_{FF}^{NL}$  is of higher order than  $\phi_{FF}^L$ , as previously discussed. Now suppose that the above boundary condition is modified by a constant and written as

$$\phi_{FF} = \bar{K} (\phi_{FF}^L + \phi_{FF}^{NL}) \quad (65)$$

When  $\bar{K} = 1$ , the condition is identical to that of Klunker, eq 50. For any other value of  $\bar{K}$  the doublet strength expressed in eq 50 is proportionally modified. Recall that the term  $\phi_{FF}^{NL}$  comes from an integration of  $\phi_x^2$  over the entire domain which means that it depends upon the solution. When this term is kept in the farfield boundary condition to compute the solution for the n-th iteration of  $\phi$ , then velocity  $\phi_x$  from the previous iteration is used.

Now, consider the effect on the pressure coefficient as  $\bar{K}$  is varied from 0 to 1, as shown in Fig 20 for incompressible flow.  $\bar{K} = 0$  is a bounding condition for the distribution of pressure coefficient  $C_p$ . Increasing  $\bar{K}$  has the effect of translating the  $C_p$  distribution uniformly toward more negative values. Since convergence of  $C_p$  is from below, as will be shown in the next section, then increasing  $\bar{K}$  can produce very accurate results for relatively coarse discretizations (i.e. large elements). In fact, for any realistic discretization that might be used a value of  $\bar{K}$  can be found that will provide  $C_p$  approximations that accurately match known or experimental results. All of the results presented in this chapter are for

6 % - Thick Parabolic-Arc Airfoil

$M_\infty = 0$

○  $\bar{K} = 0$

△  $\bar{K} = 1/3$

□  $\bar{K} = 2/3$

▽  $\bar{K} = 1$

- - Exact (Thin-Airfoil Theory)

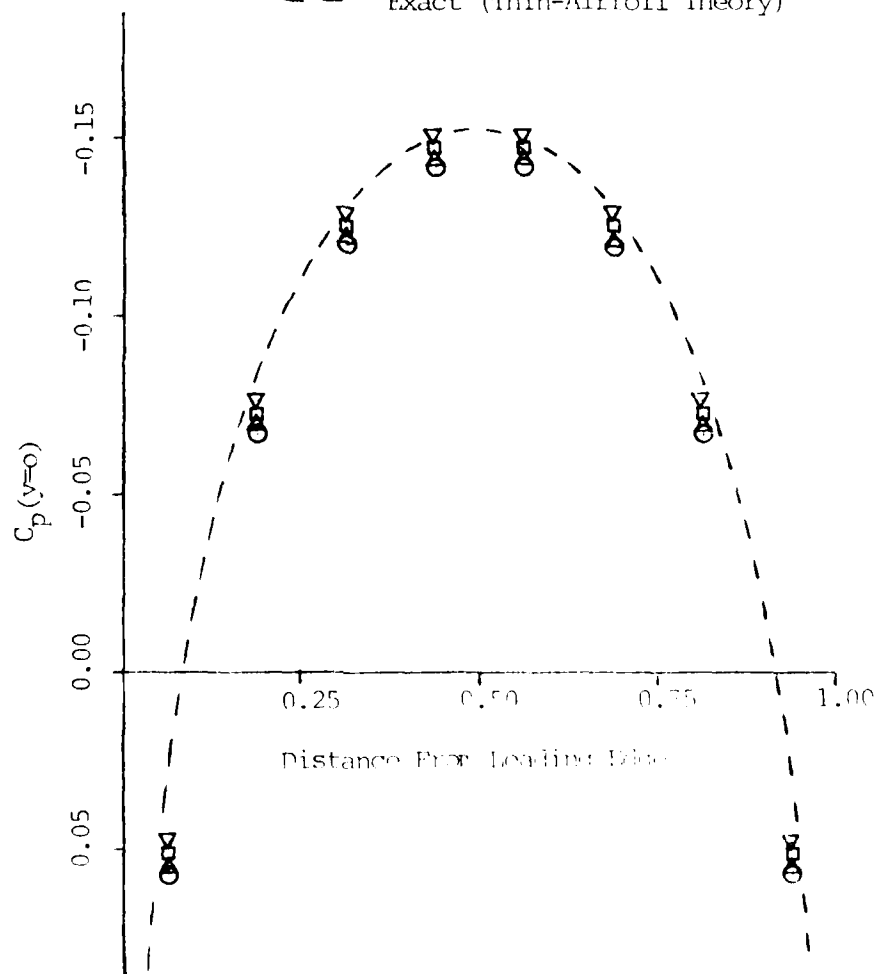


Figure 20 - Effect of Varying the Strength of the Farfield Boundary Condition

AD-A107 201

AIR FORCE INST OF TECH WRIGHT-PATTERSON AFB OH SCHOO--ETC F/6 20/4  
PREDICTION OF AERODYNAMIC FORCES ON A CIRCULAR CYLINDER AND A T--ETC(U)

JUN 79 J E MARSH

UNCLASSIFIED

AFIT/DS/AA/79M-1

AFIT-CI-79-216D

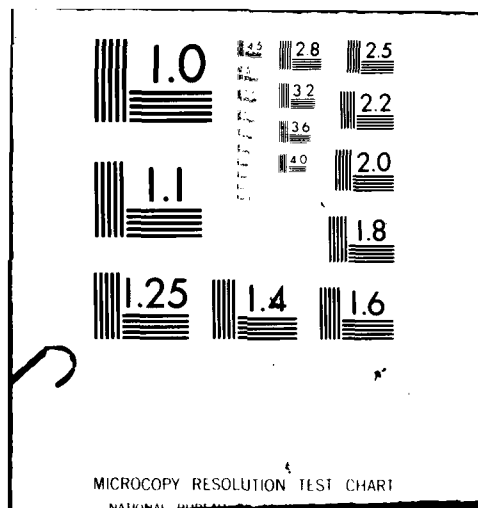
NL

2 of 2

25 0710



END  
DATE  
FILMED  
12-81  
DTIC



$$\bar{K} = 1.$$

For compressible flow the effect of keeping the nonlinear far-field boundary term is not significant (Ref 13). Since this term is of higher order (Ref 18) its contribution is negligible particularly for subsonic flow and even for Mach numbers which produce transonic flow. For example, the average change in the solution for the pressure coefficient with the nonlinear boundary term included is only: 0.09% for  $M_\infty = 0.5$ , 0.32% for  $M_\infty = 0.7$ , and 0.85% for  $M_\infty = 0.8$ . Due to the computational nature of  $\phi_{FF}^{NL}$  and its minimal effect on the solution, it may be neglected in favor of reducing computer time.

No other type of farfield boundary conditions were studied; however, several other possibilities could be tried and will undoubtedly be the basis for further study.

Element Refinement. In order to study the point-wise convergence of the pressure coefficient as element size decreases, all other discretization and solution parameters were held fixed while element size was varied. Figure 13 shows a typical discretization of the flow-field governed by parameters NDX, NDY, and NDXA which are defined in the figure. The farfield boundary was located at  $X_{max} = Y_{max} = 1.50$ . Element refinement was done 4 ways:

- (1) All elements in the flowfield were uniformly decreased in size.
- (2) Only elements above the airfoil were decreased in width only while those for  $|x| \geq 0.5$  were held fixed (see Fig 13).
- (3) Elements for  $|x| \geq 0.5$  were refined in width only while all other discretization parameters were held fixed (i.e. changing  $\Delta x$  for  $|x| \geq 0.5$  while  $\Delta x$  for  $|x| \leq 0.5$

and  $\Delta y$  for  $y \geq 0$  are fixed; see Fig 13).

- (4) All elements were refined in height (i.e. giving more layers of elements) while all other discretization parameters were held fixed.

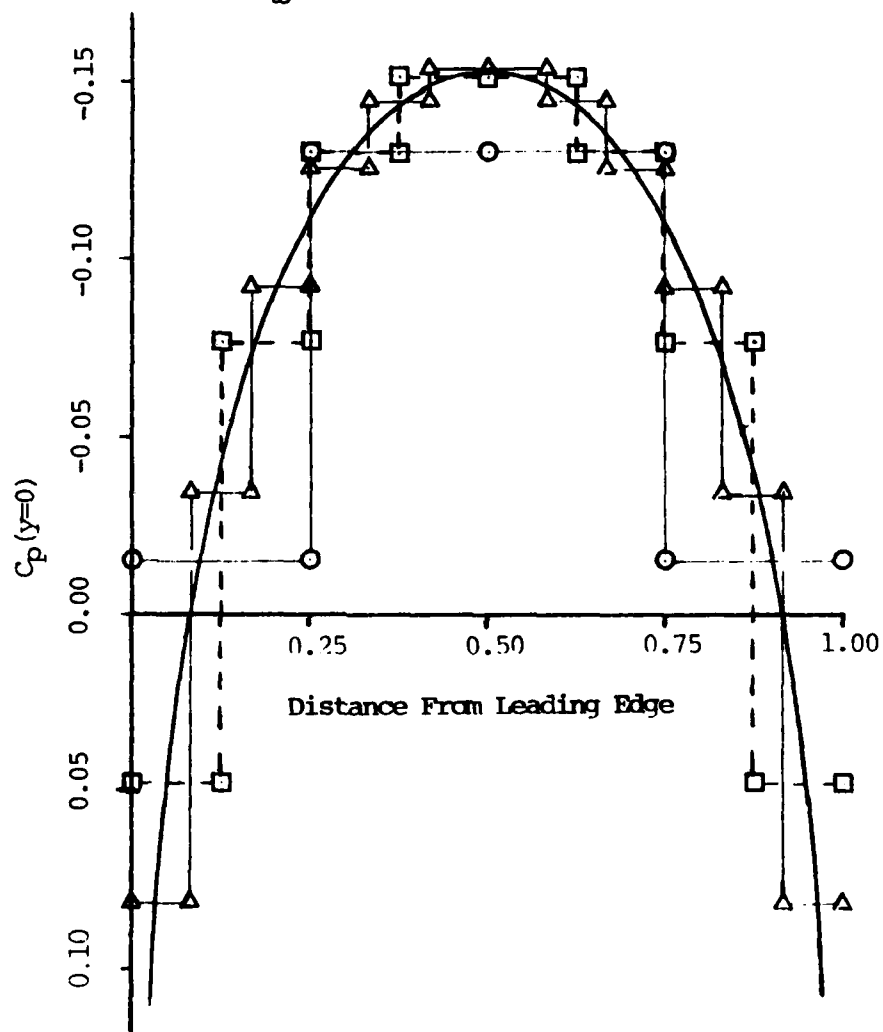
Figure 21 shows the effect of uniform element refinement (i.e. procedure 1 above) on the solution for the pressure coefficient for  $M_\infty = 0$ . The exact curve computed from thin-airfoil theory is also shown for comparison purposes.

Two observations can be made from Fig 21. First, the step function for each of the approximations intersects the exact curve at some point in the interval of the step size. Thus, even the approximation from the most coarse discretization is not unrealistic. Secondly, the point-wise error over most of the chord decreases with a corresponding decrease in element size. In an average sense, the error in pressure decreases with element refinement. Further, the point-wise convergence at the midchord appears to be very rapid compared to that at the leading and trailing edges. The description of pressure coefficient at the leading and trailing edges improves as the elements become smaller, but improvement is slower than for other points on the airfoil. Special finite element treatment may be needed for regions near the singular points to improve the convergence there. The results in Fig 21 show that the solution trend is correct, in that, it approaches the exact solution as element size approaches zero.

Refinement of elements only in the region over the airfoil profile (i.e. procedure 2) has a slightly different effect on the pressure distribution than does uniform refinement of all elements in the flowfield. The coefficients of pressure for refinement of

6 % - Thick Parabolic-Arc Airfoil

$$M_{\infty} = 0$$



Symbol	Nodes	Elements	NDX	NDXA	NDY
○	36	36	4	4	3
□	119	96	8	8	6
△	225	192	12	12	8

Figure 21 - Effect of Uniform Element Refinement on the Solution for Pressure Coefficient

discretization parameter NDXA alone are presented in Fig 22. Note that the actual shape of the pressure distribution is more well defined with smaller elements due to the step-function nature of pressure, but the pressure at the mid-point of each step does not show substantial deviation from the exact solution with refinement. The greatest change with refinement of NDXA occurs near the leading and trailing edges where better definition of the pressure coefficient is obtained as the elements become smaller. The change near the peak is almost insignificant by comparison.

The difference in the behavior of pressure for the two refinement procedures described thus far suggests a discretization technique. First, discretize  $C_p$  with relatively large elements everywhere and refine the element size until there is little change in the pressure coefficient at the midchord. Then, for better definition of the distribution refine only the NDXA parameter. Perhaps an improvement on this technique would be the use of variable size elements with the smaller elements located near the leading and trailing edges.

Refining elements beyond the airfoil leading and trailing edges (i.e. procedure 3, refining parameter NDX only) has little effect on the pressure distribution except in the two elements containing the leading and trailing edges respectively; refer to Fig 23. The variation of pressure that occurs in these two elements does not appear to be directly related to the change made in the refined elements. The fact that  $C_p$  changes at all is due to the decrease of size in elements adjacent to the leading and trailing edge elements. It clearly points out that "for points farthest removed from the elements refined, the smaller the change the refinement makes." This "truism"



# 6%-Thick Parabolic-Arc Airfoil

$$M_{\infty} = 0$$

○ NDXA = 4

△ NDXA = 8

□ NDXA = 16

◇ NDXA = 20

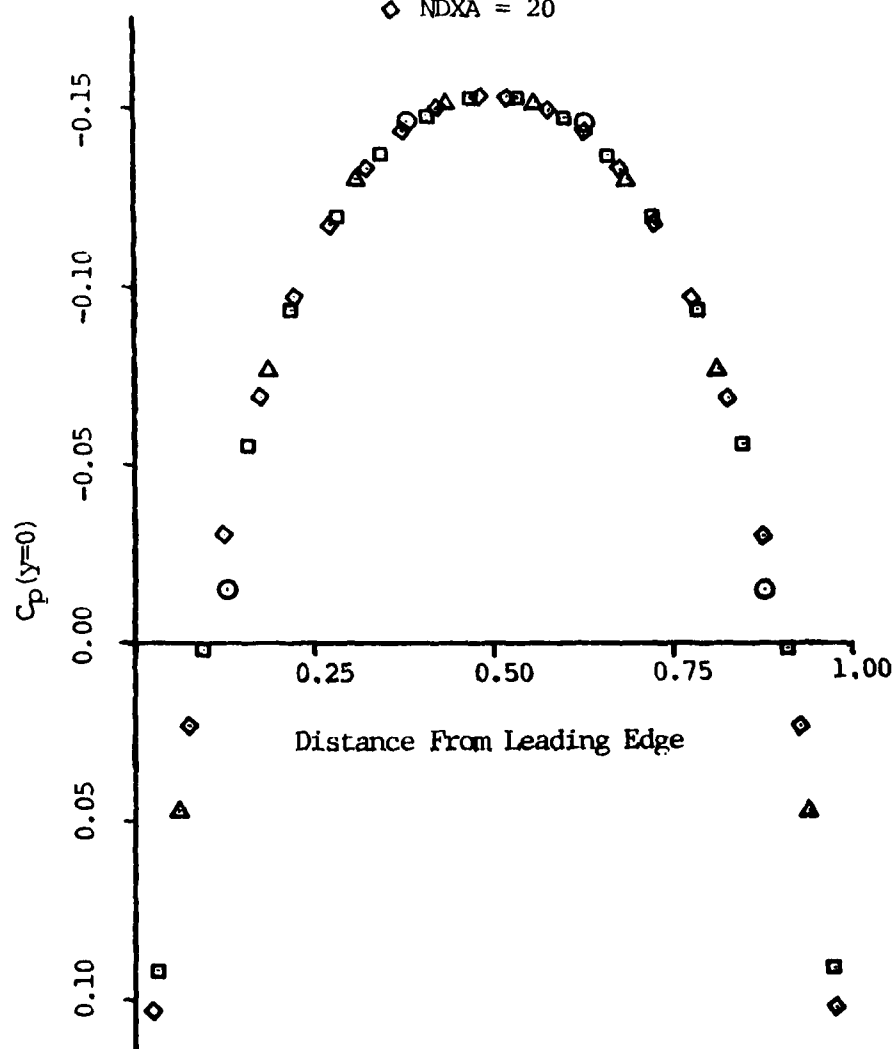


Figure 22 - Effect of Refining Discretization Parameter NDXA Only

6 % - Thick Parabolic-Arc Airfoil

$M_{\infty} = 0$

○ NDX = 4

□ NDX = 8

△ NDX = 16

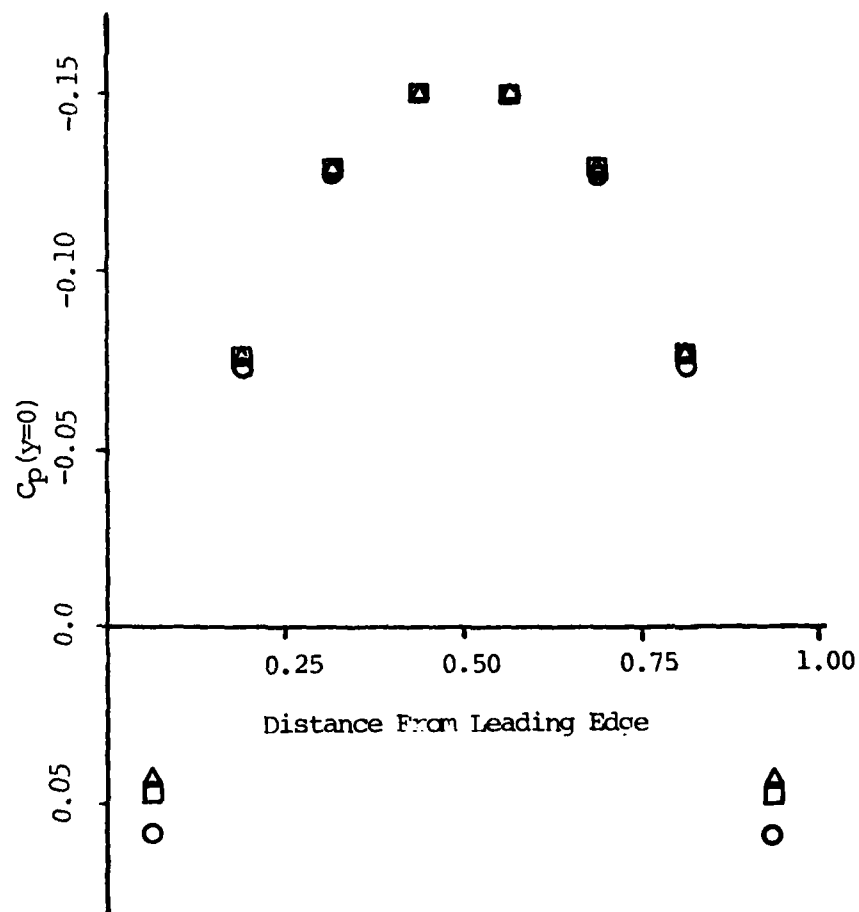


Figure 23 - Effect of Refining Discretization  
Parameter NDX Only

is detected in Fig 23 by noting the decreasing rate of change in pressure as the midchord is approached from either direction.

Refinement of NDY with all other discretization parameters held fixed (i.e. procedure 4) significantly affects the pressure distribution as shown in Fig 24. Changes occur rapidly near the peak, but are slower near the leading and trailing edges. The width of the elements as well as the height needed to be refined near these points to improve the resulting approximation.

#### Incompressible Results

Figure 25 shows a comparison between the finite element solution for the pressure coefficient and the exact curve computed from thin airfoil theory. The pressure coefficient is a step function, but when the midpoint value in each step interval is plotted the comparison with the exact solution shows good agreement. The finite element solution was obtained using discretization parameters:  $X_{\max} = 1.5$ ,  $Y_{\max} = 2.0$ ,  $NDX = 8$ ,  $NDXA = 18$ ,  $NDY = 8$ .

Another interesting comparison is shown in Fig 26 where the finite element solution is compared with a finite difference solution obtained from Ref (40). The finite difference solution was obtained using a constant grid step size  $\Delta X = \Delta Y = 0.125$  everywhere. The finite element results were obtained using the same step size over the airfoil surface (i.e.  $\Delta X_A = 0.125$ ), but the other element dimensions were twice as large as that used in the finite difference calculations (i.e.  $\Delta X = 0.25$ ,  $\Delta Y = 0.25$ ). The degrees-of-freedom for the two solutions were 119 nodes for finite element and 350 grid points for finite difference. The accuracy achieved by the finite element method

6 % - Thick Parabolic-Arc Airfoil

$$M_{\infty} = 0$$

○ NDY = 3

□ NDY = 6

△ NDY = 12

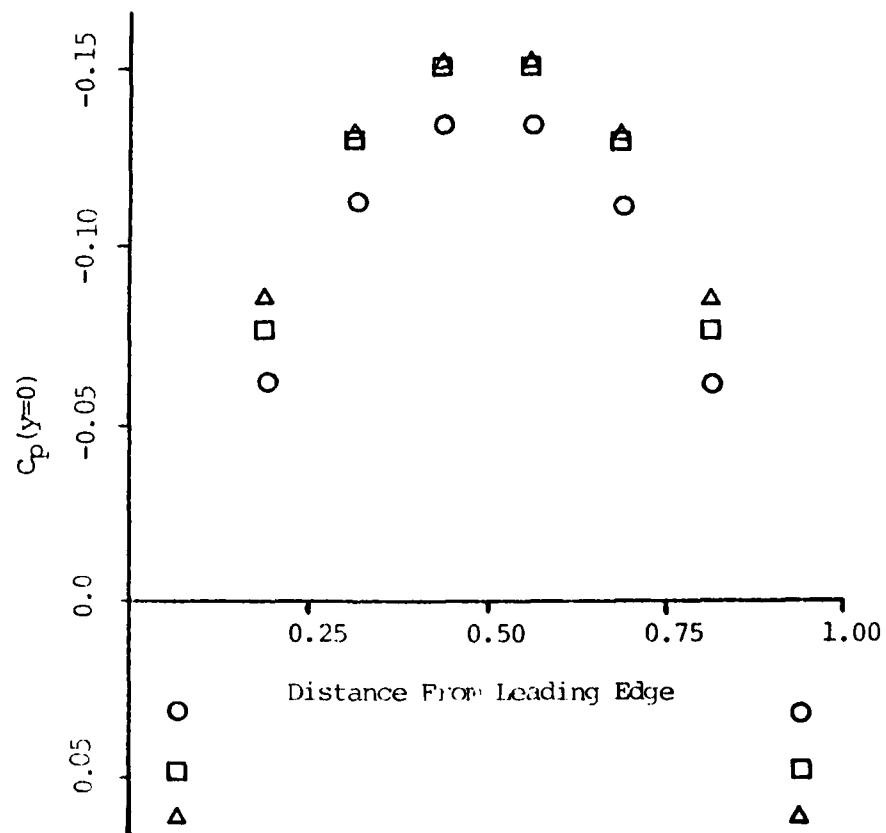


Figure 24 - Effect of Refining Discretization Parameter NDY Only

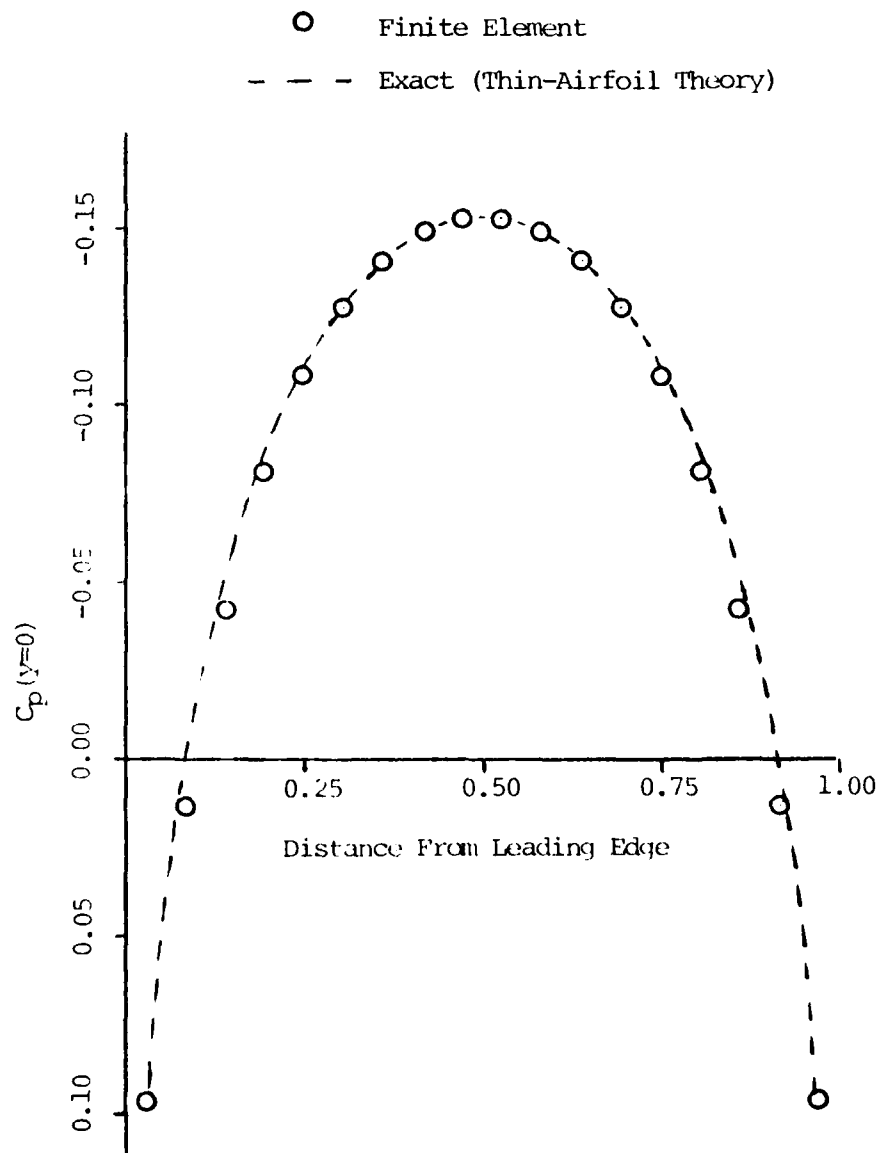


Figure 25 - Pressure Coefficient for a 6%-Thick Parabolic-Arc Airfoil for  $M_\infty = 0$

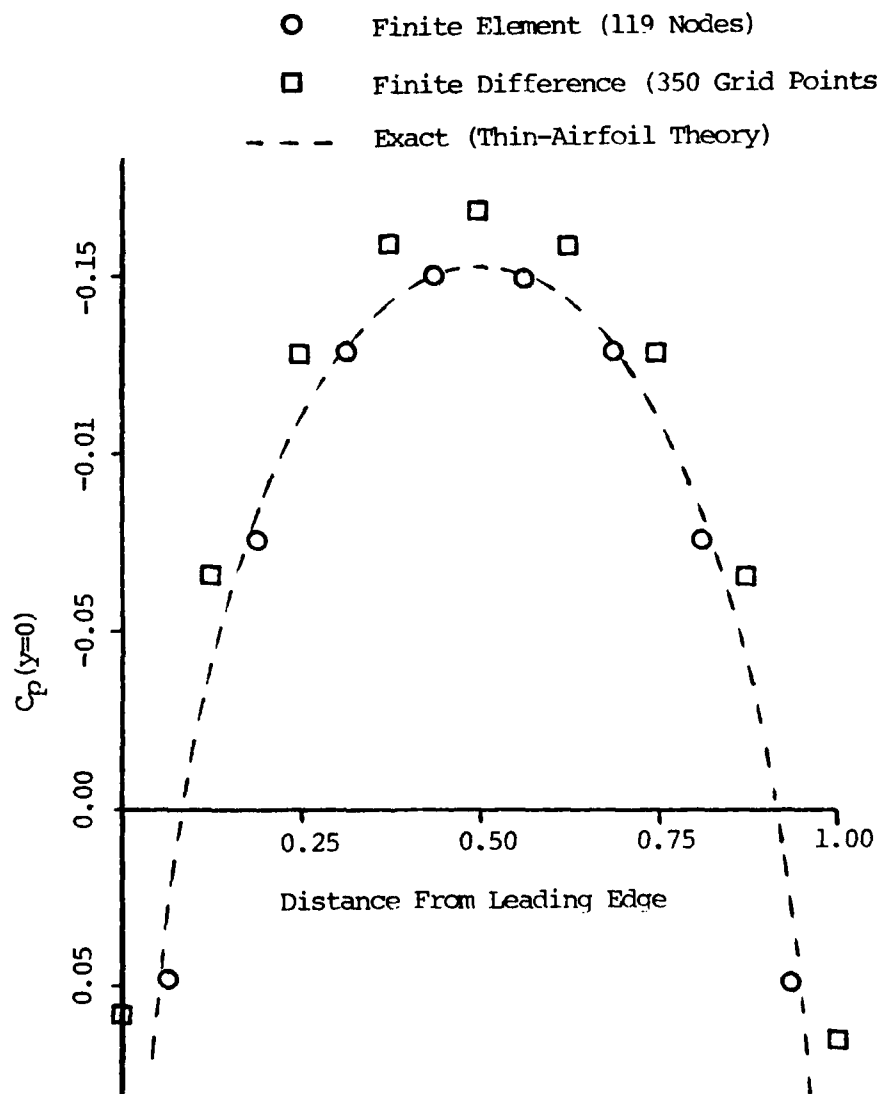


Figure 26 - Comparison of Results for a 6%-Thick Parabolic-Arc Airfoil for  $M_\infty = 0$

is clearly better than for finite difference.

### Compressible Subsonic Results

The flow is subsonic at all points in the flow domain  $\Omega_F$  as long as the coefficient of  $\phi_{,xx}$  in the governing differential equation remains positive. When the free-stream Mach number is increased slightly above a critical value, then the coefficient of  $\phi_{,xx}$  becomes negative in a small subregion of  $\Omega_F$  and transonic flow begins. Before discussing results for compressible subsonic flow, the convergence behavior of the iterative solution algorithm for Mach numbers through the subsonic regime up to the onset of transonic flow is considered.

Convergence of Iterative Scheme. Recall that the approximate solution of the governing differential equation was written in iterative form as expressed by eq 58. Also recall that convergence of the iterative solution scheme was governed by the criteria specified in eq 45. For  $\epsilon = 0.5 \times 10^{-4}$  the number of iterations required to achieve convergence of eq 58 is presented in Figs 27 and 28 as a function of Mach number. For the data in these figures, solutions were started by setting all nodal values of potential equal to zero. For low subsonic flow ( $0.0 \leq M_\infty \leq 0.5$ ) the number of iterations required for convergence of the iterative scheme is five or less. Fewer iterations were required when solutions were started from better initial guesses. For example, fewer iterations than given in Fig 27 were required to obtain a solution for  $M_\infty = 0.5$  when the iterative scheme was started from the solution for  $M_\infty = 0.4$ . As the Mach number was increased to  $M_\infty = 0.8$  the slope of the convergence curve increased, but convergence still occurred in seven or less iterations.

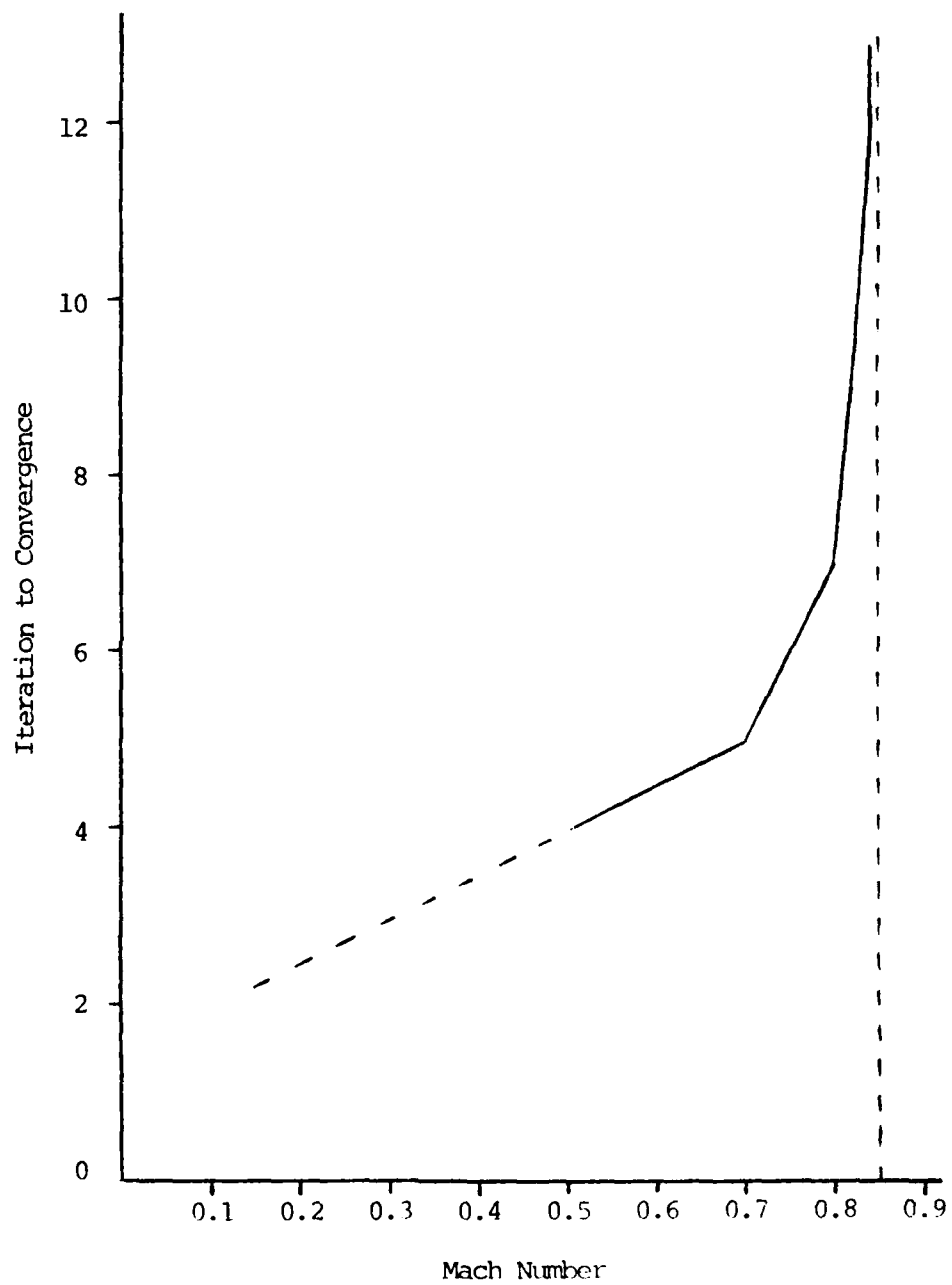


Figure 27 - Convergence of Solution Algorithm  
as a Function of Free-Stream Mach  
Number



At approximately  $M_\infty = 0.85$  a sharp increase in the number of iterations occurred as indicated by the vertical segment of the curve in Fig 27. At this Mach number a small supersonic bubble has formed in the flow above the midchord of the airfoil and the equation has locally changed type. For  $M_\infty = 0.85$  the iterative solution scheme no longer converged in the sense of eq 45 for small values of  $\epsilon$ . What happened to the solution of the potential function for each iteration is illustrated in Fig 28. In this figure the percent change in the nodal value of the potential function at the midchord was computed from  $\Delta\phi = |(\phi^{n+1} - \phi^n) / \phi^{n+1}|$  and plotted as a function of the iteration number for Mach numbers from 0.50 to 0.86. The solution was initiated by setting the potential function equal to zero at all nodes. As observed in Fig 27, for low subsonic flow the potential converges rapidly, but for  $M_\infty = 0.85$  the potential function does not converge at all. Initially the solution gives the appearance of converging as it does for lower Mach numbers, but then an iteration is reached (iteration 6) where the apparent convergence trend begins to reverse itself. This behavior occurs because the governing equation has locally changed type from elliptic to hyperbolic in a small region above the midchord. Further iterations produced what appears to be a diverging solution scheme. In actuality the solution does not diverge, but cycles back through the "bucket" shape shown in Fig 28. The behavior for larger Mach numbers was similar to that shown for  $M_\infty = 0.85$ . In general, the "bucket" shape moves to the left and upward indicating that fewer iterations are required before the solution develops to the stage where transonic flow occurs.

Comparison of Results. First, the distribution of pressure

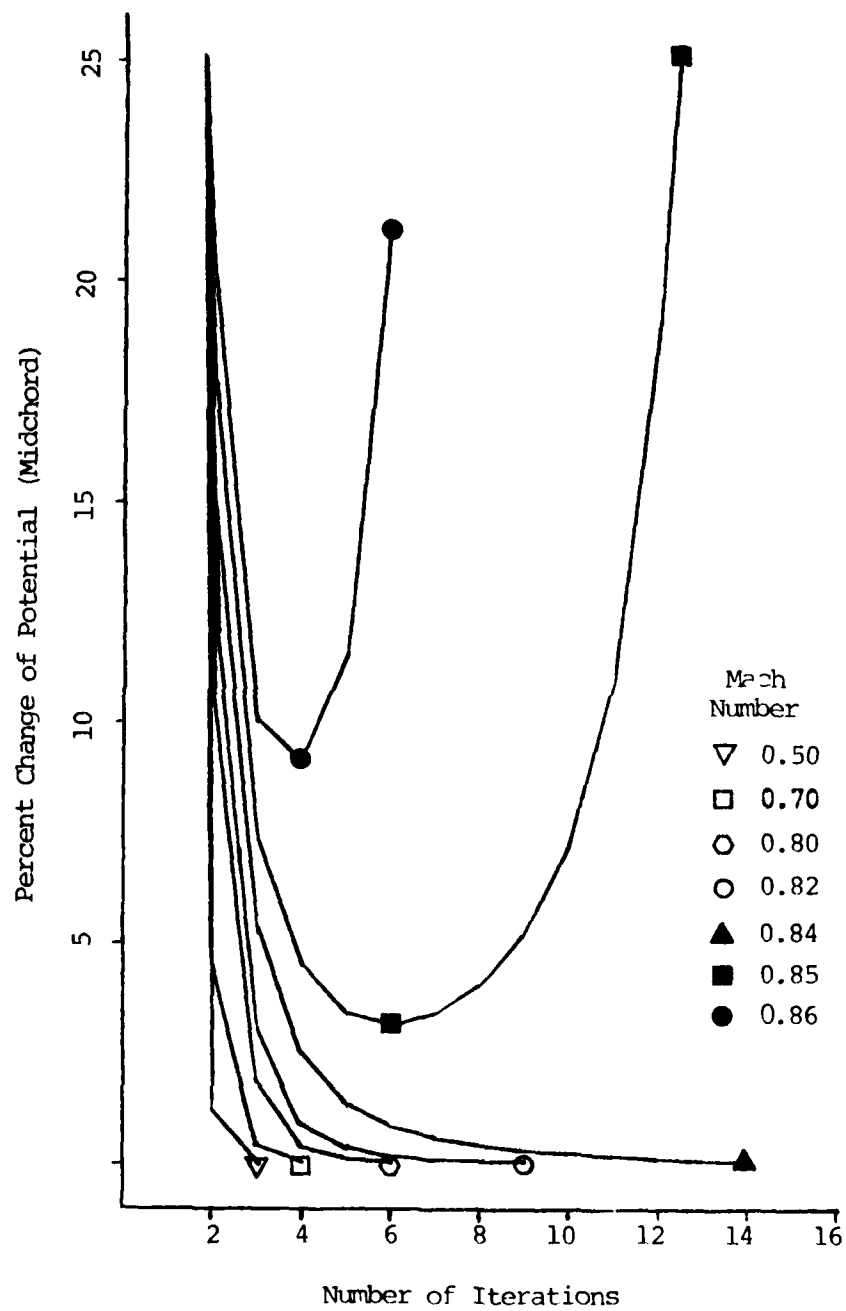


Figure 28 - Convergence Behavior of Potential Function at the Midchord as Function of Free-Stream Mach Number

coefficient for a given discretization is shown in Fig 29 as a function of Mach number. The distributional shape of  $C_p$  is slightly different than predicted from linear theory, where  $C_p$  scales with Mach number by a factor  $(1 - M_\infty^2)^{1/2}$ . The departure from linear theory is not significant but is attributable to the presence of the nonlinear term in the differential equation, which begins to become significant for Mach number near  $M_\infty = 0.8$ . More discussion of nonlinear effects is included in the next section. Figure 30 compares finite element results with experimental data obtained by Knetchnel (Ref 39) for  $M_\infty = 0.707$ . Good agreement exists over most of the airfoil. For comparison purposes a finite difference solution (Ref 40) is given for  $M_\infty = 0.7$  (which is 1% lower than for other results). In addition, the exact-linear, thin-airfoil-theory results obtained by scaling the incompressible solution are shown. The farfield boundary locations were the same for both the finite element and finite difference approximations ( $X_{\max} = Y_{\max} = 1.5$ ). However, the number of nodes used for the finite element method was more than an order of magnitude less than the number of grid points used for the finite difference method (i.e. 225 nodes compared to 8514 grid points, respectively). The finite difference solution does not compare with the experimental data as well as either the finite element or the exact linear solutions.

Figure 31 compares  $C_p$  distributions for  $M_\infty = 0.8$  obtained from the present finite element solution, finite difference solutions (Ref 40), and from linear, thin-airfoil-theory solutions. The difference in pressure distributions between the solutions from linear theory and the two numerical solutions based on nonlinear theory are readily detectable. Differences between the finite element and

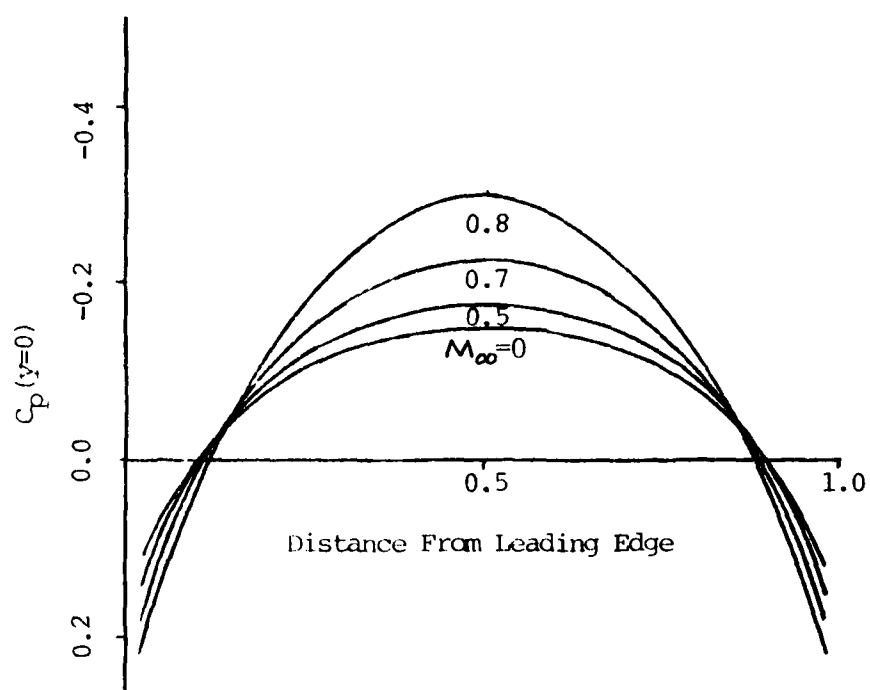


Figure 29 - Mach Effects on  $C_p(y = 0)$  for  
a 6%-Thick Parabolic-Arc Airfoil

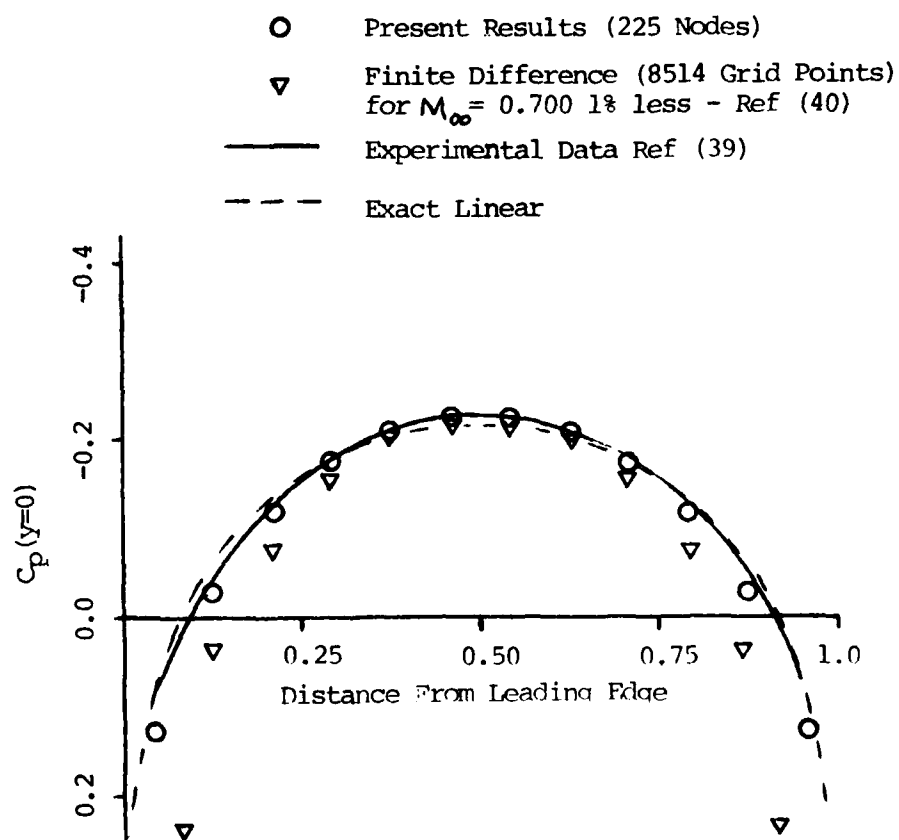


Figure 30 - Comparison of Results for a 6%-Thick Parabolic-Arc Airfoil at  $M_\infty = 0.707$

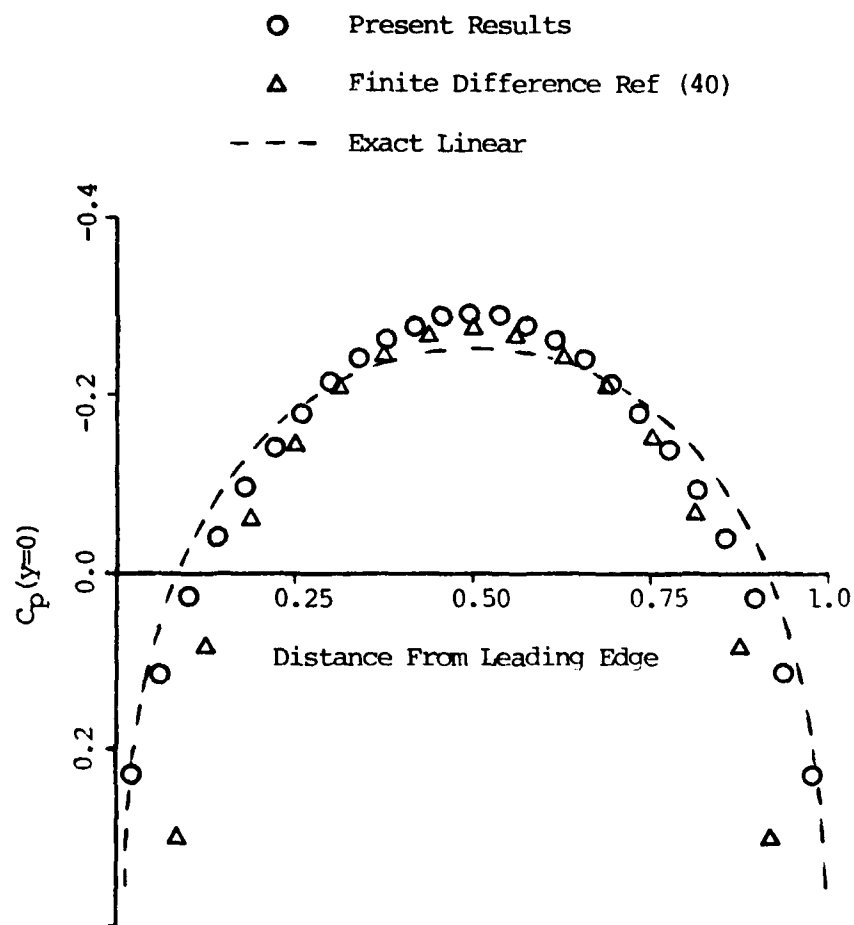


Figure 31 - Comparison of Results for a 6%-Thick Parabolic-Arc Airfoil at  $M_\infty = 0.80$

finite difference results occur for the entire distribution. These variations are due to the inherent difference in approximations achieved by each method and, perhaps to a lesser extent, the finer mesh size used for the finite difference solution.

### Transonic Flow

Iterative Behavior of Solution Scheme. As discussed previously, the iterative solution algorithm does not converge, as it does for subsonic flow, once a supersonic bubble larger than half of an element forms in the flowfield. Figures 32 and 33 show solution results after each iteration for Mach numbers equal to 0.84 and 0.86 respectively. The solution shown in Fig 32 converges in the sense of eq 45 after 12 iterations for a tolerance of  $\epsilon = 0.5 \times 10^{-4}$ . The peak  $C_p$  is slightly above the critical value of  $C_p^* = 0.347$ , but the supersonic bubble only engulfs approximately half of the element which straddles the point of maximum thickness. When the Mach number is increased to 0.86 the solution fails to converge. Figure 33 shows what happens to the solution for the first 6 iterations. The solution remains symmetric (shockless) and after 3 iterations, more than one element is contained in the supersonic bubble. Solutions for further iterations (except iteration 8 which goes off the page) are shown in Fig 34. The spike at the midchord continues to increase until iteration 9, when it changes sign and creates a crevice at the midchord. Further iterations result in the fallen spike being rebuilt, which eventually occurs, and then the process is repeated. Thus, the solution is oscillatory, and although it never converges neither does it diverge. If the Mach number is increased further, violent oscillations occur and eventually the solution diverges.

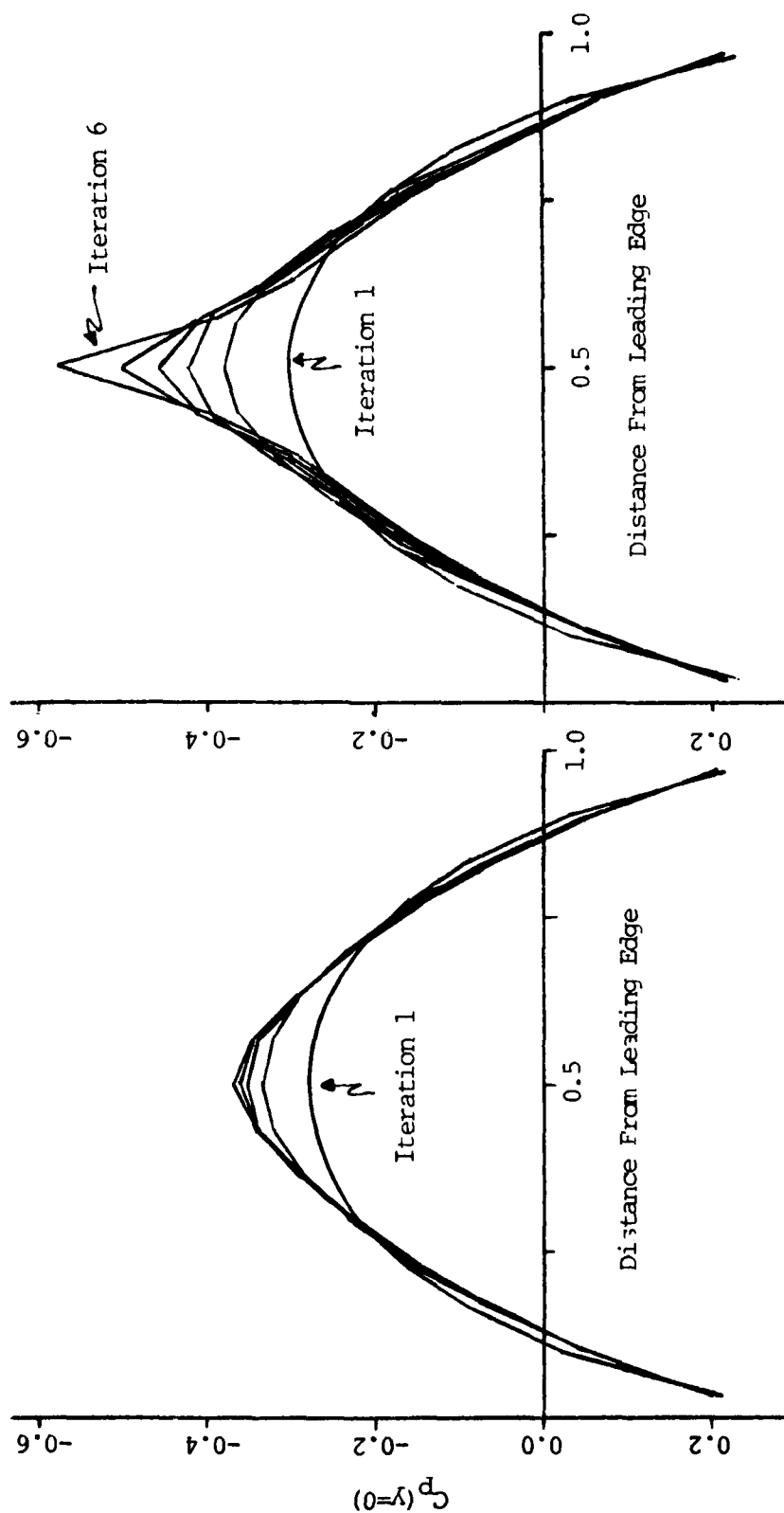


Figure 32 - Convergence Behavior of Iterative Solution Scheme for  $M_\infty = 0.84$

Figure 33 - Divergence Behavior of Iterative Solution Scheme for  $M_\infty = 0.86$



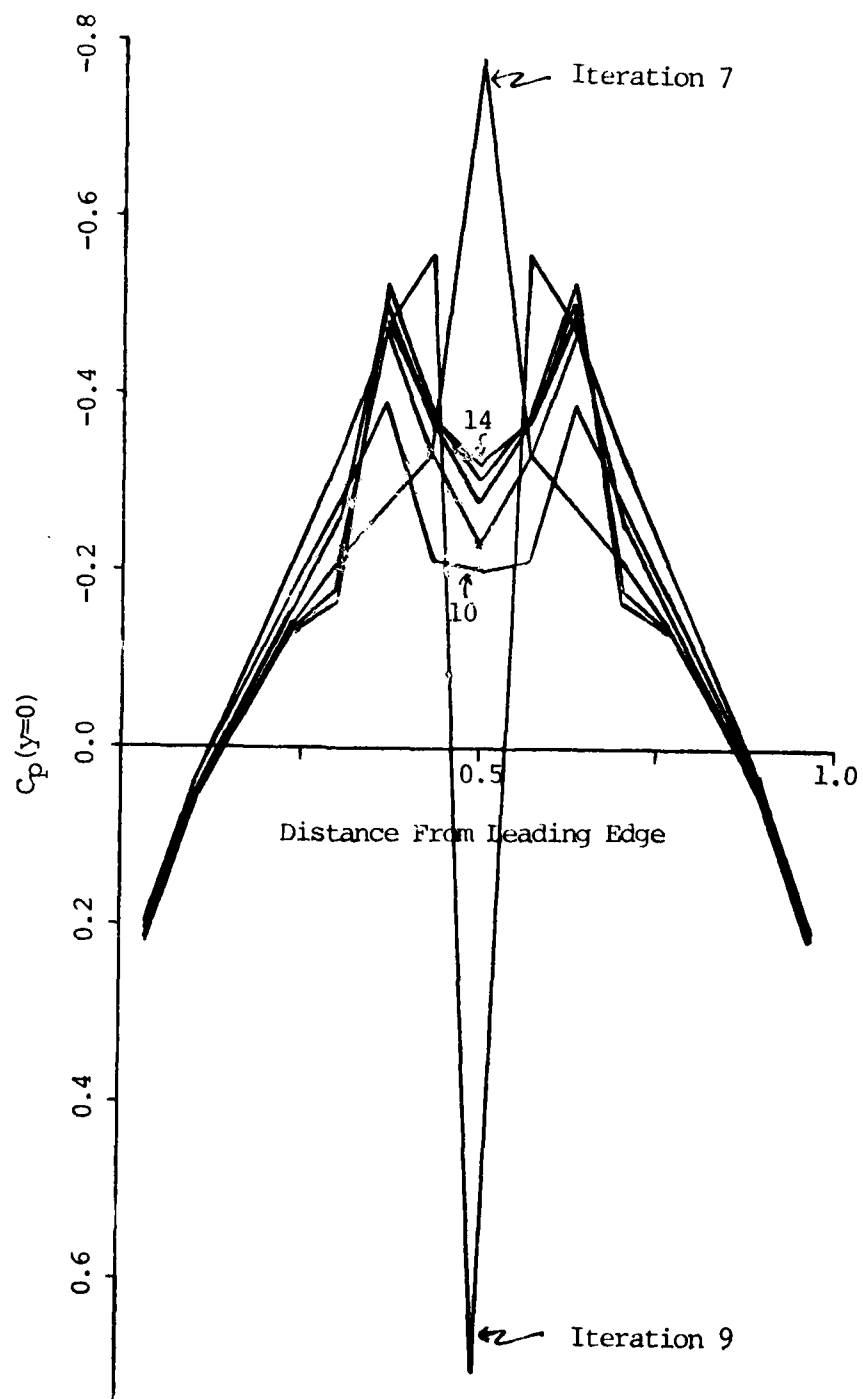


Figure 34 - Further Iterative Behavior  
(Continued from Figure 33)  
for  $M_\infty = 0.86$

Figures 32-34 were included only to illustrate the behavior of the solution at the on-set of transonic flow when the finite element solution is obtained as if the problem was elliptic. When the coefficient of  $\phi_{,xx}$  in the differential equation becomes negative, the differential equation changes type from elliptic to hyperbolic which forms the supersonic bubble in the flow. Since elliptic differential equations are fundamentally different than hyperbolic ones, then formulations and algorithms suitable for elliptic equations are not expected to be valid for hyperbolic equations. At this point in the solution scheme, the "upwinding" techniques described in Chapter IV were employed.

Upwinding Techniques. The upwinding techniques that were reported in the literature, as described in Chapter IV, were tried for the transonic flow problem. None of the reported techniques were able to stabilize the iterative solution scheme, and a discussion of the solution behavior for each of these techniques is omitted. In general, when they were employed one of two things happened. First, for most cases considered, the application of the upwinding technique caused the iterative solution scheme to diverge immediately. Secondly, for a few cases where the solution scheme converged, it converged to a solution that was not physically meaningful. Due to the inability of the reported upwinding techniques to stabilize the solution scheme, other upwinding schemes were sought. As a result, the new proposed upwinding technique was developed.

Recall that the new upwinding technique described in Chapter IV modifies the finite element formulation to account for the hyperbolic character of the equation for those elements within the supersonic

bubble. The behavior of the upwinding procedure is governed by two parameters  $R$  and  $U$ . Equation 62 gives the modification of the finite element formulation of the governing equation by these two parameters for elements within the supersonic or hyperbolic bubble. The behavior of the solution as a function of these two parameters is shown in Figs 35 to 39. For the airfoil considered, the numerical values of  $R$  and  $U$  fall somewhere in the ranges:  $0 \leq R \leq 0.3$  and  $0 \leq U \leq 0.6$ .

The behavior of the solution (pressure distribution) as a function of upwinding parameter  $U$  for fixed values of  $M_\infty$  and parameter  $R$  is shown in Figs 35-37. Although a different value of  $R$  or  $M_\infty$  is held fixed in each of these figures, the effect of  $U$  on the solution is the same in each case. The function of  $U$  is to change the symmetry of the flow. If  $U$  is set equal to zero (corresponding to the upwinding scheme not being employed), then the distribution of  $C_p$  remains symmetric about the midchord, as shown in Fig 33. Note in Figs 35-37 that for increasing values of  $U$  the distributions are skewed downwind. Pressure gradients become greater on the downwind side of the peak value, in the vicinity of an expected, weak compression shock. Thus parameter  $U$  not only alters the symmetry of the pressure distribution, but it also appears to capture the behavior of weak shocks by permitting relatively large discontinuities of velocity to occur aft of the peak pressure. This behavior is particularly evident in Fig 37 for  $U = 0.40$ .

The behavior of the solution (pressure distribution) as a function of parameter  $R$  for fixed values of  $U$  is shown in Figs 38 and 39. The distribution of pressure coefficient is not substantially affected by changes in parameter  $R$  except near the peak. In this region increased

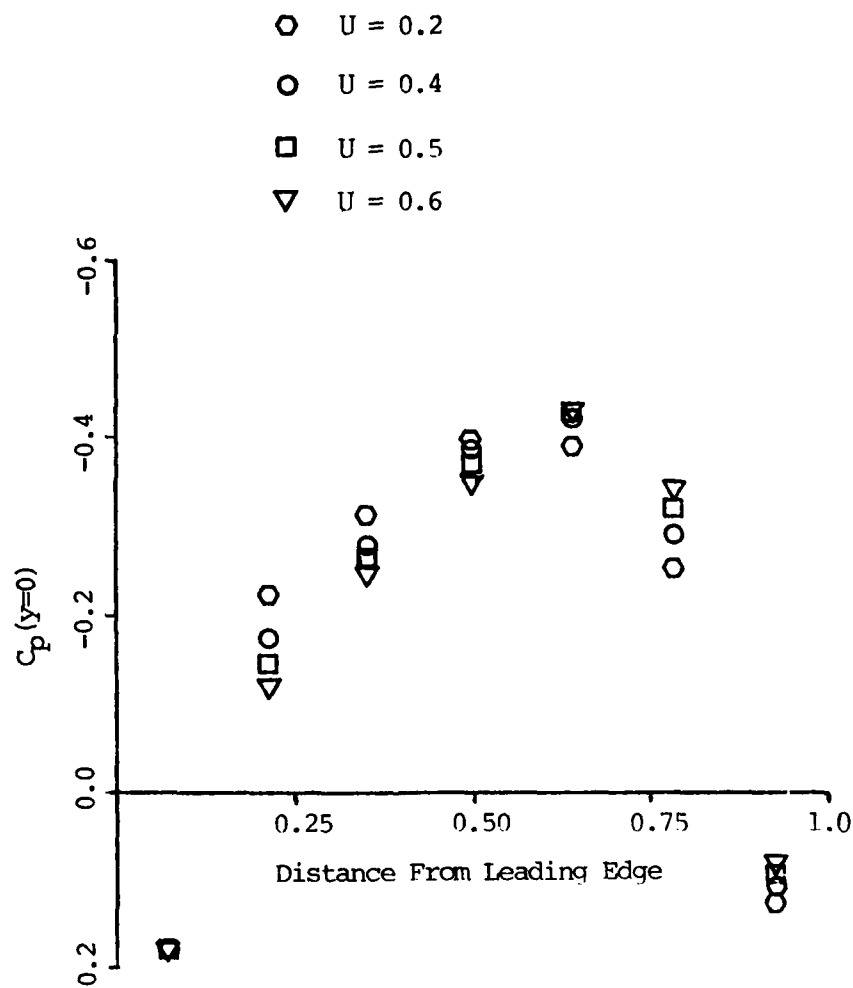


Figure 35 - Effect of Upwinding Parameter  $U$  for a 6%-Thick Parabolic-Arc Airfoil at  $M_\infty = 0.908$  and  $R = 0$

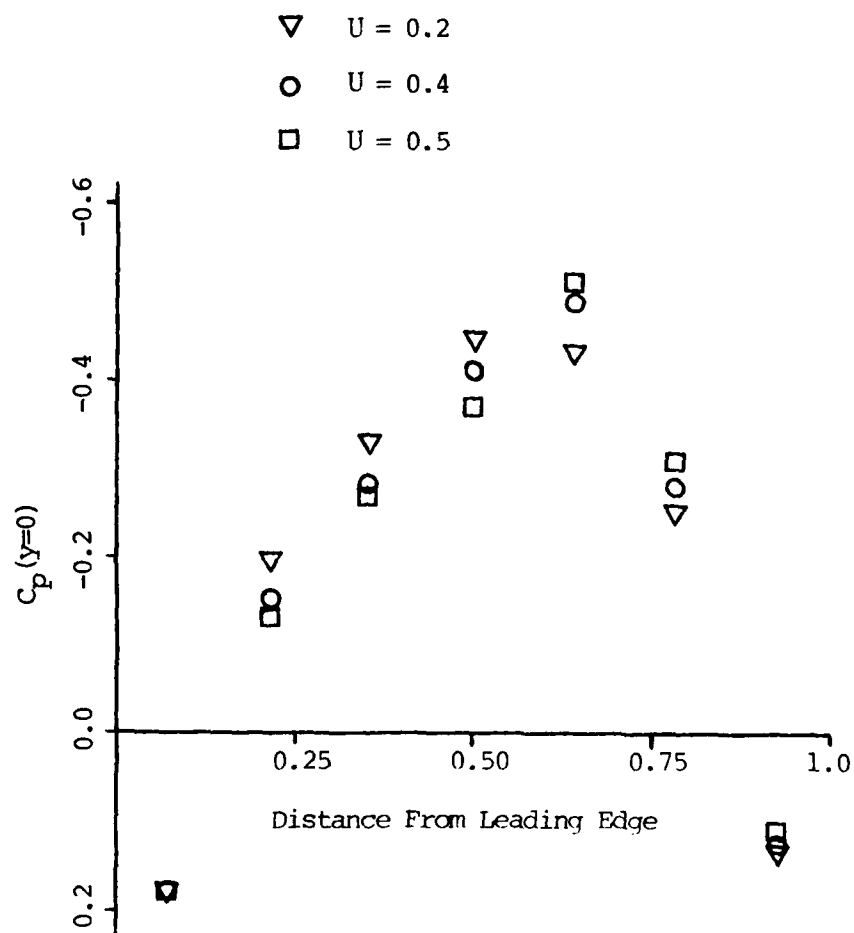


Figure 36 - Effect of Unwinding Parameter  $U$  for a 6%-Thick Parabolic-Arc Airfoil at  $M_\infty = 0.908$  and  $R = 0.20$

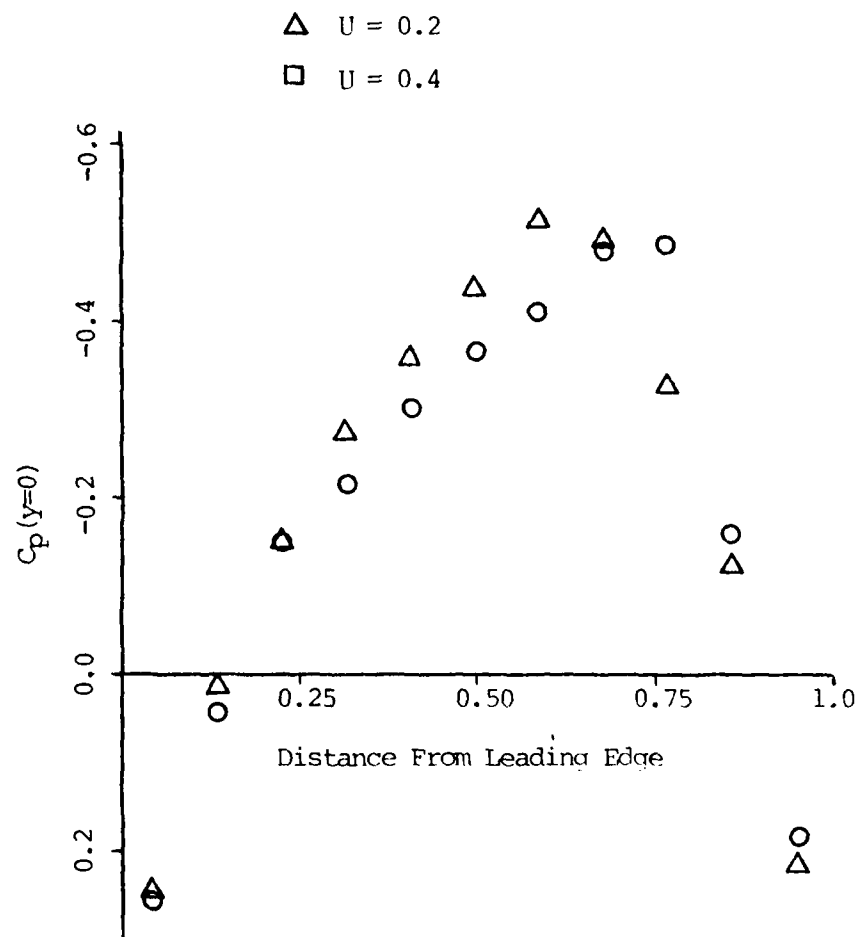


Figure 37 - Effect of Upwinding Parameter  $U$  for a 6%-Thick Parabolic-Arc Airfoil at  $M_\infty = 0.92$  and  $R = 0.20$

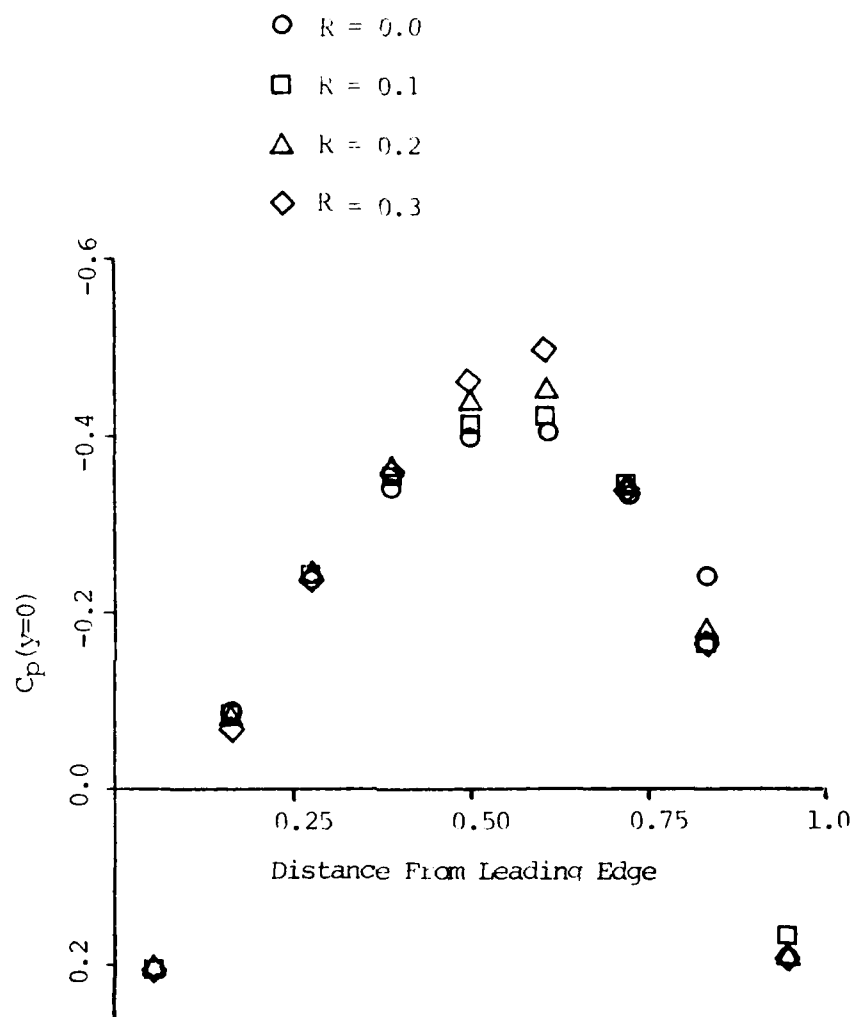


Figure 38 - Effect of Parameter  $R$  for a 6%-Thick Parabolic-Arc Airfoil at  $M_\infty = 0.908$  and  $U = 0.20$

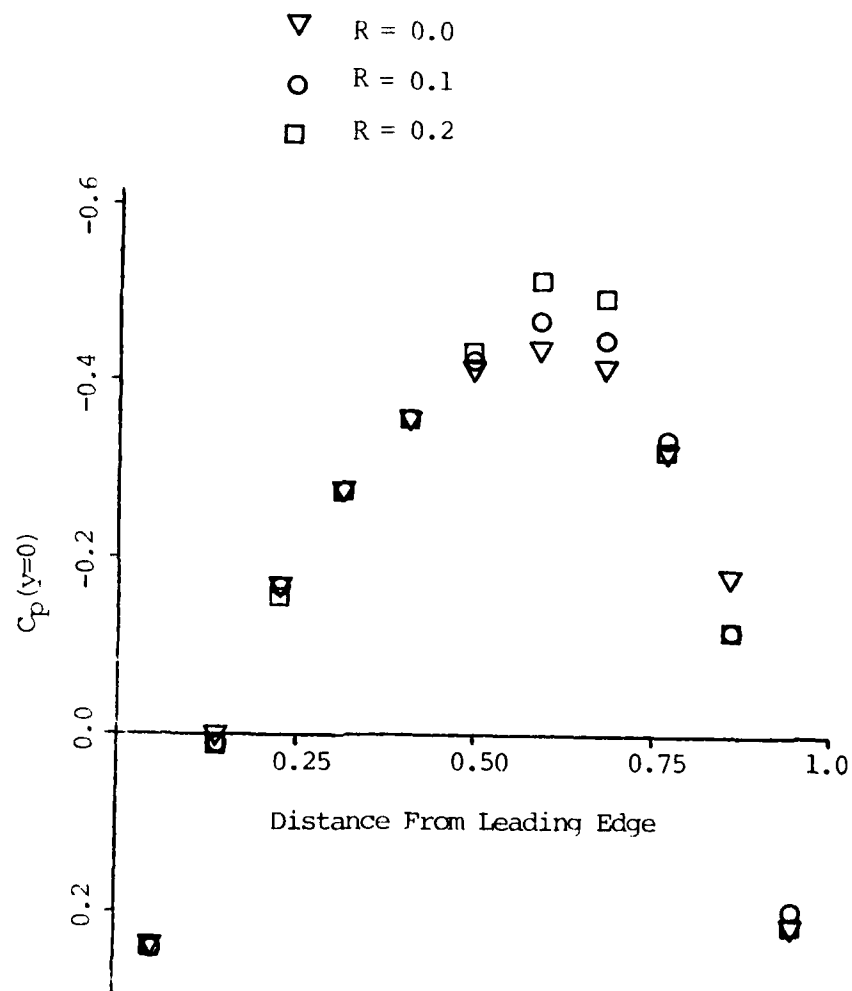


Figure 39 - Effect of Parameter  $R$  for a 6%-Thick Parabolic-Arc Airfoil at  $M_\infty = 0.92$  and  $U = 0.20$



values of  $R$  produce larger peak pressures which means aft of the peak larger gradients of pressure are produced. Thus parameter  $R$  also appears to be contributing to the numerical mechanism of capturing the weak compression shock. Recall that the function of  $R$  is to retain part of the nonlinear term on the left-hand-side of the governing equation and to subject the remaining part to the upwinding operation. Judging from the results in Figs 38 and 39 it may be necessary to keep part of the term on the left-hand-side of the equation, which means that an inversion must be done for each iterate. If the entire nonlinear term is treated as a force (i.e.  $R = 0$ ) then accuracy may be sacrificed. The value of  $R$  for the cases considered range between 0.2 and 0.3 for best results.

If  $R$  is arbitrarily selected, say  $R = R_a$ , for given values of  $M_\infty$  and  $U$ , then one of three things could happen. First, if  $R_a$  is picked too large the solution will either diverge or oscillate about some solution as demonstrated in Figs 33 and 34. For this situation not enough of the nonlinear term is subjected to the upwinding operation to permit convergence of the iterative scheme. Secondly, if  $R_a$  is picked too small, then too much of the nonlinear term is altered by the upwinding process. As a consequence, even if the solution algorithm converges, the solution may not be as close to the true solution as it could be for a larger value of  $R_a$ . Thirdly, if  $R_a$  is appropriately chosen, the iterative scheme will converge to an accurate solution which correctly describes the physics of the problem as shown for the examples in the next section.

In general, the values of  $R$  and  $U$  depend upon the airfoil shape, Mach number, and the angle of attack for lifting airfoils. When

values of  $R$  and  $U$  are correctly chosen, then convergence occurs rapidly; usually less than 15 iterations are required. If, on the other hand, they are not correctly chosen, then the iterative scheme will not converge. After a couple of iterations the scheme will reach a point of divergence which indicates that the other values of  $R$  and  $U$  should be selected for the case being considered. Unfortunately, there are no known analytical expressions which select the best values of  $R$  and  $U$  for specific airfoils and flow cases. The values can be determined iteratively as suggested by the procedure in Chapter IV. This procedure first requires that "ballpark" values of  $R$  and  $U$  be found which permit convergence of the iterative scheme. Next,  $R$  and  $U$  are "fine tuned" to select the "best" possible values.

Comparison of Results. Finite element solutions for transonic flow over a 6% - thick parabolic-arc airfoil are compared with experimental data obtained by Knetchel (Ref 39), finite difference calculations of Olsen and Batill (Ref 40) and also those of Olsen (Ref 60), and with finite element solutions of Akay (Ref 24). For  $M_{\infty} = 0.908$ , finite element solutions for the pressure coefficient are presented in Figs 40 and 41 for seven discretizations of the flow domain  $\Omega_f$ , as specified in Table VI.

Table VI  
Domain Discretization Parameters,  
For  $M_{\infty} = 0.908$

Grid	NDX	NDXA	NDY	Nodes
1	8	5	6	98
2	8	7	7	128
3	8	7	9	160
4	6	14	9	210
5	6	9	13	224
6	6	9	13	224
7	6	11	11	216

By comparing the solutions for the pressure coefficients given in Fig 40 with those given in Fig 41, a significant difference in behavior is noticed only in the vicinity of the expected, weak compression shock. In Fig 40 for grids 1-3 at a location eight-tenth of a chord-length from the leading edge ( $x_{LE} = 0.8$ ), a comparatively large jump in  $C_p(y=0)$  occurs between adjacent elements. This behavior occurs naturally in the solution process and is associated with the occurrence of a weak compression shock which occurs in the flow domain to permit the fluid in the supersonic bubble to return to subsonic conditions.

The occurrence of the jump at  $x_{LE} = 0.8$  was not forced by imposing any shock jump conditions. but it is an inherent consequence of the potential formulation of the problem, the finite element approach selected to solve the problem, and the use of the new upwinding scheme governed by parameters  $R$  and  $U$ . Since the velocity potential function is being solved for, and since elements were selected which insure only

6% - Thick Parabolic-Arc Airfoil

$M_\infty = 0.908$

○ Grid 1

□ Grid 2

△ Grid 3

--- Experimental, Ref (39)

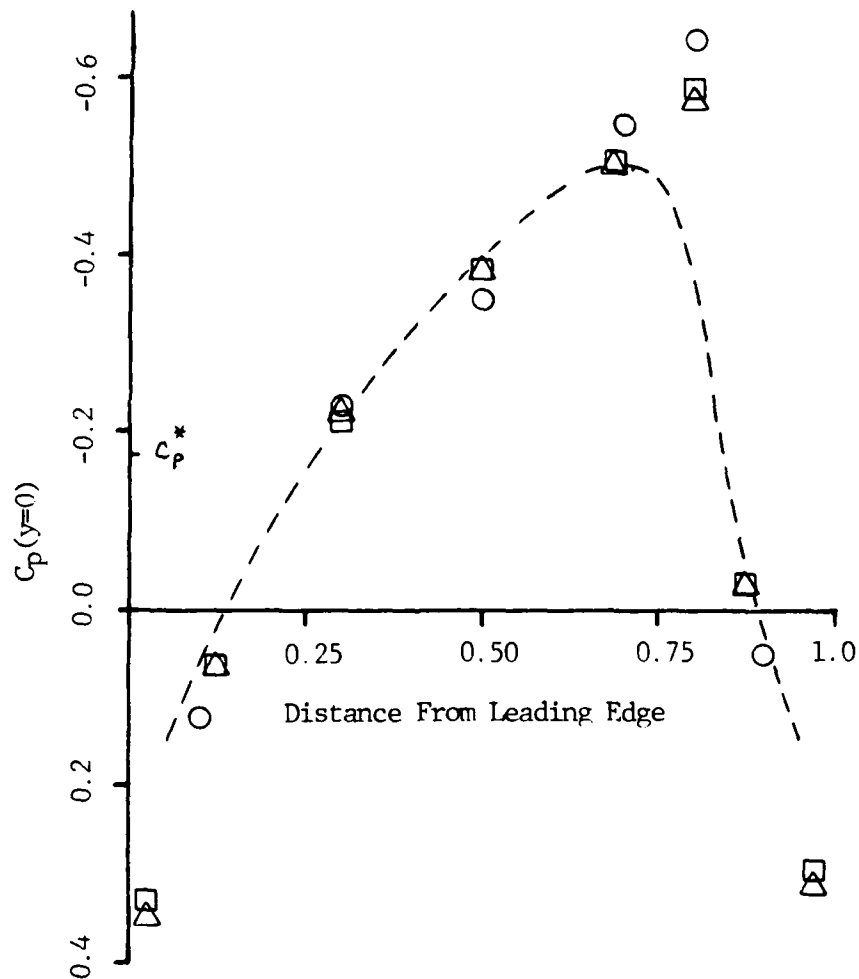


Figure 40 - Finite Element Solutions,  
 $R = 0.25$  and  $U = 0.70$

6% - Thick Parabolic-Arc Airfoil

$M_\infty = 0.908$

○ Grid 4

□ Grid 5

△ Grid 6

◇ Grid 7

--- Experimental, Ref (39)

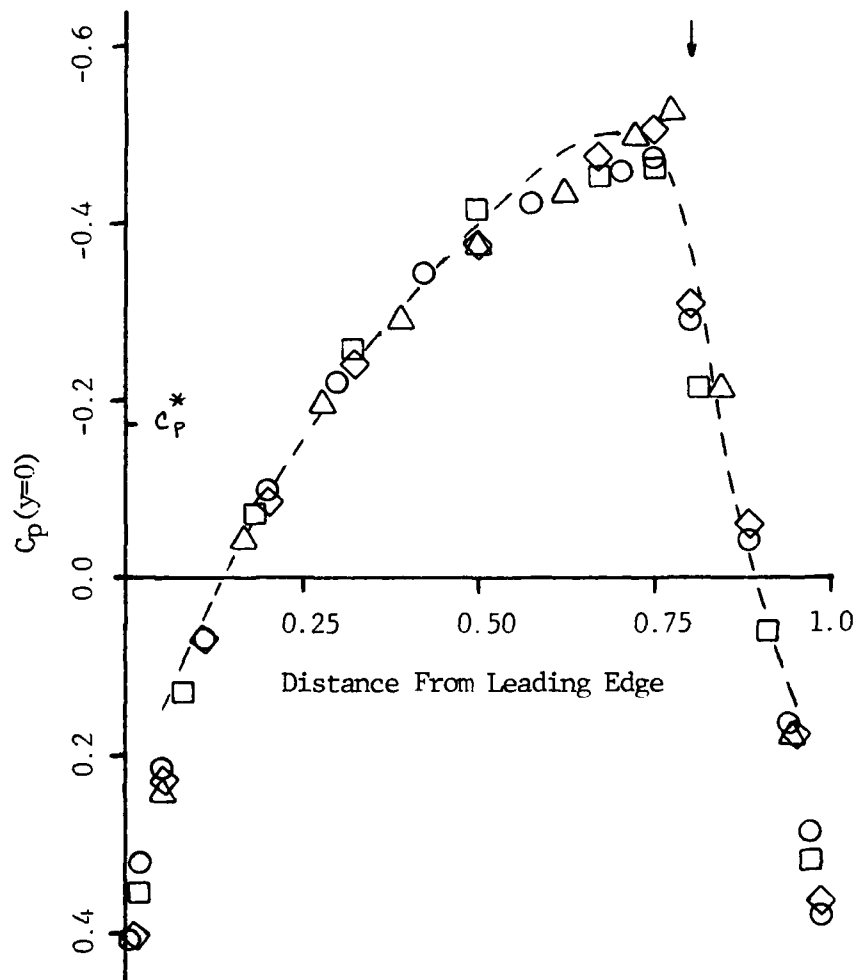


Figure 41 - Finite Element Solutions,  
 $R = 0.25$  and  $U = 0.50$

continuity of the velocity potential function across inter-element boundaries, then jumps or discontinuities in the derivatives of the potential function (i.e. velocities) across inter-element boundaries are inherently expected to occur. From small-disturbance theory, the pressure coefficient is proportional to the velocity in the x-direction, thus a corresponding jump of pressure between elements. The significant part of this behavior is that the jump is of sufficient magnitude to allow the flow to change from supersonic to subsonic conditions by crossing an element boundary line, thus an ideal shock of zero thickness. This particular behavior occurs only when the discretization is arranged in such a manner that a node occurs at the location where the weak shock would like to impinge upon the airfoil.

The solutions presented in Fig 41 are notably different in the vicinity of  $X_{LE} = 0.8$ . For these solutions the discretization does not place a node at  $X_{LE} = 0.8$ ; the discretizations straddle that point instead. Since the shock should occur at  $X_{LE} = 0.8$ , then it must occur within an element rather than on its boundary. However, there is no numerical mechanism for the shock to occur within an element, as there is between elements. Consequently, two jumps are required to return the flow from supersonic to subsonic conditions. For these discretizations the solutions smear the shock over the span of one element and two successive inter-element boundary locations.

The difference between solutions given in Fig 40 and those given in Fig 41 is more graphically demonstrated in Fig 42, where solutions for grids 3, 6, and 7 are compared. The symbol at the peak of each distribution indicates the location of the expected weak shock, which is denoted by the vertical arrow at  $X_{LE} = 0.8$ . All other symbols

6% - Thick Parabolic-Arc Airfoil

$M_\infty = 0.908$

$\triangle$  Grid 3 ( $X_{LE} = 0.800$ )

$\circ$  Grid 6 ( $X_{LE} = 0.778$ )

$\square$  Grid 7 ( $X_{LE} = 0.750$ )

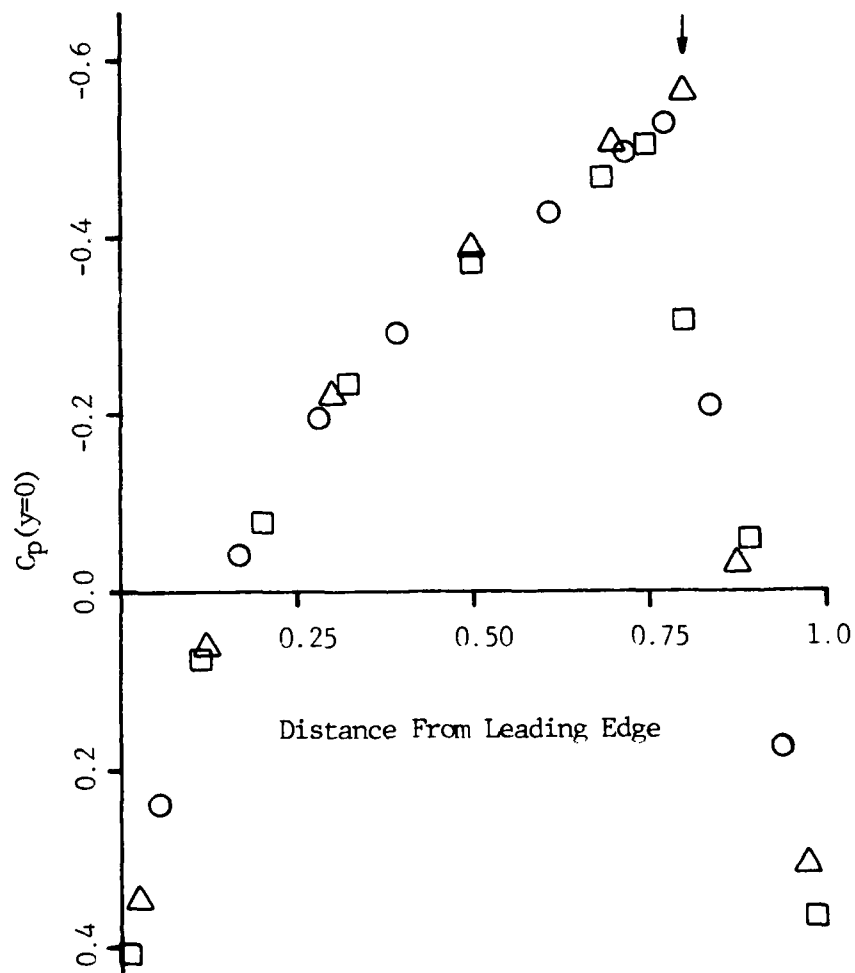


Figure 42 - Effect of Element Fitting  
Near the Weak Shock

are plotted at the midpoint of the interval (i.e. midway between nodes) as described previously. Note, as the elements which straddle the shock become large (i.e. grid 6 as compared to grid 7), the more the solution is affected in the vicinity of the weak shock. It appears that smearing the shock over a larger element tends to decrease the magnitude of the peak pressure, as well as, affecting the magnitude of the jumps required to return the flow to subsonic conditions. Although smearing does not provide the best approximation, in terms of describing the physics of the flow, it does provide an acceptable approximation without the use or need of shock elements. Better approximations can be obtained by altering or "fine tuning" the discretizations to provide solutions similar to those obtained from grid 3.

The new upwind method appears to exhibit characteristics common to both shock "capturing" and "fitting" techniques. The location and strength of the weak shock can be obtained without fitting the discretization in the sense described. However, if better approximations are required, then the discretization can be iterated upon to fit the element boundaries so they coincide with the location of the shock. From the approach taken in this study, the shape of the shock is restricted to a vertical line segment (i.e. parallel with the y-axis). In general, the shock may be inclined to the vertical, although it would remain straight. Discretizations could be devised by rotating segments of the grid to fit the shock between adjacent elements for such cases. Neither of the situations represented in Fig 42 would be possible without the use of the new upwinding technique. Without its use the pressure distribution would remain symmetric with respect to the midchord, and the solution algorithm would not converge.



Convergence is possible only because the physics of the flow is modelled by excluding the downwind influence on the solution at upwind nodes.

Figure 43 compares the finite element solutions for no smearing of the shock with the finite difference solutions and with experimental data. The two finite difference solutions correspond to a constant grid size (Ref 40) and a variable grid size (Ref 60), respectively. The latter solution was obtained for smaller step sizes near the leading and trailing edges and in the vicinity of the expected shock. The finite element solutions were also obtained from both constant (grid 1) and variable element sizes (grids 2 and 3). For the variable element discretizations, smaller (more narrow) elements were placed near the leading and trailing edges. In addition, solutions were attempted for discretizations that were refined only in the region where the shock was expected to occur. This discretization resulted in a grid where "needle like" elements were placed adjacent to elements of aspect ratio near unity. The solution algorithm for such discretizations did not converge and the idea of using variable size elements to assist in "capturing" the shock was abandoned. It is believed that the upwinding technique is applicable only for elements of constant size throughout the supersonic bubble, and it works best when the aspect ratio of the elements is near unity. Any substantial departure from a uniform grid particularly in the center segment (refer to Fig 13) leads to convergence problems in the iterative solution process.

Figure 44 shows a comparison of pressure distributions obtained from two finite element solutions using different upwinding techniques. The finite element solution presented in Fig 40 for grid 3 is compared with the solution obtained by Akay (Ref 24). His upwinding technique

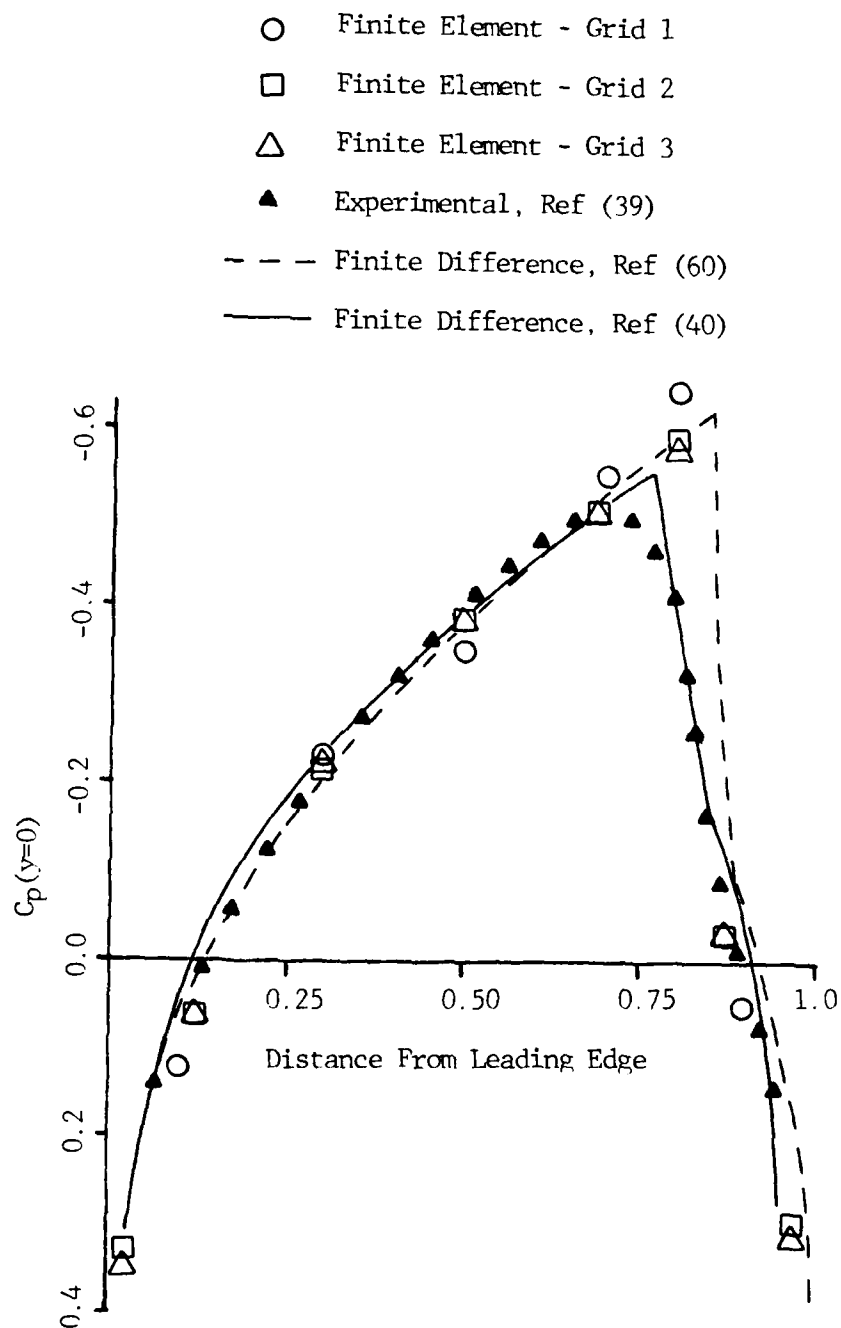


Figure 43 - Comparison of Results for a 6%-Thick Parabolic-Arc Airfoil for  $M_\infty = 0.908$

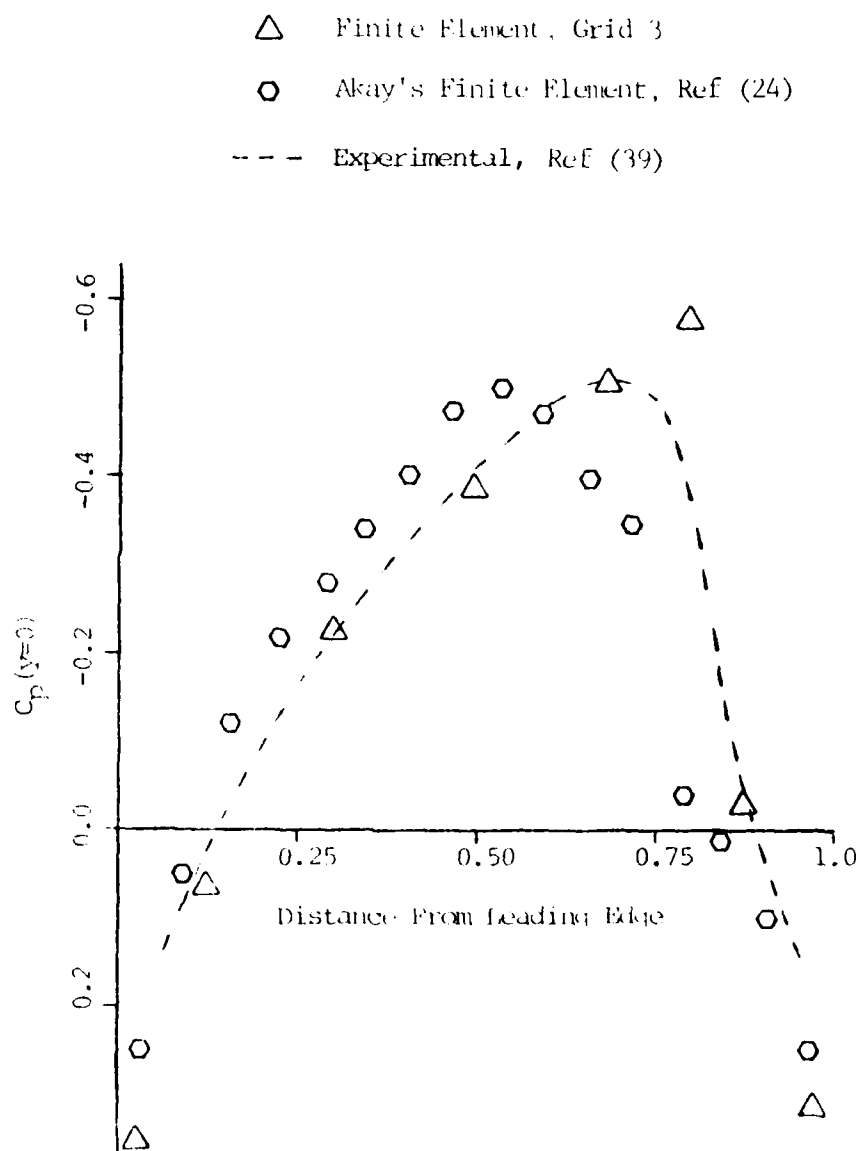


Figure 44 - Comparison of Two Finite Element Results for a 6%-thick Parabolic-Arc Airfoil for  $M_\infty = 0.908$

differed from that used in this study as described in Chapter IV. It consisted of replacing the velocity  $g_e^2$  by  $(1+\Theta)g_e^2 + \Theta g_u^2$ , where  $g_u$  is the velocity upstream of element  $e$ . The value of  $\Theta$  was taken to be 0.20. The results of this study agree with the trend of the experimental data and the finite difference solutions much better than do Akay's predictions. It is believed that the difference in upwind techniques, rather than formulation methods is what accounts for the variation between the two  $C_p$  distributions.

Figure 45 compares the distribution of  $C_p(y=0)$  with experimental data for a 6%-thick parabolic arc airfoil at  $M_\infty = 0.92$ . Domain  $\Omega_F$  was discretized with grid 7 described in Table VI. Upwinding parameters of  $R = 0.20$  and  $U = 0.40$  were required to obtain convergence. Essentially the same behavior observed for the solution for  $M_\infty = 0.908$  applies to this case. The shock is smeared over one element and the pressure distribution agrees with the trend of the experimental data.

In general the new upwinding technique gave acceptable results. A number of other upwinding techniques described in Chapter IV were tried. None of these gave satisfactory results, although each technique did alter the symmetry in the flow. In most cases the initial application of the upwinding technique resulted in a dramatic change in the flowfield velocities. As a result, the solution scheme either diverged after one or two iterative steps, or it oscillated without regularity about some solution. The possibility exists that these upwinding techniques could be modified to provide successful application, but no such alterations were found in this study.

6% - Thick Parabolic-Arc

$M_\infty = 0.920$

▲ Finite Element, Grid 7

--- Experimental Data, Ref (39)

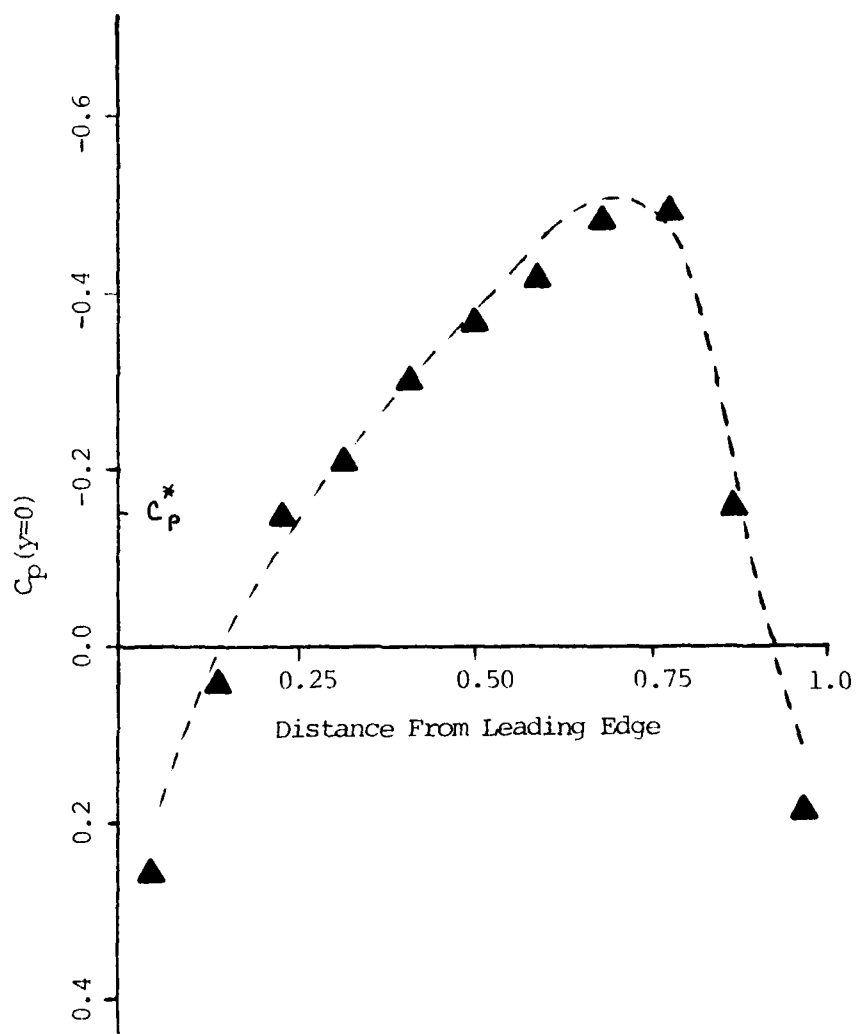


Figure 45 - Finite Element Solutions,  
 $R = 0.20$  and  $U = 0.40$

## VII Summary, Conclusions, and Recommendations

The Galerkin Finite Element Method was used to obtain approximate solutions of the steady, transonic, small-disturbance, velocity potential equation for flow over a circular cylinder and thin airfoil.

### Circular Cylinder

Incompressible Flow. One non-conforming and two conforming sector elements were used to solve the problem of incompressible flow without circulation over a unit circular cylinder. The non-conforming element was rejected because the solution error became significant as element size was refined. It gave accurate approximations only for coarse discretization of the flowfield. Velocity distributions calculated from the two conforming elements agreed well with the exact solution. In general, the new sector element gave more accurate solutions than the other sector element, which was based upon a conventional bilinear polynomial approximation. The new element was developed from a trial solution using rational functions. For incompressible flow over the cylinder the radial size parameter of the new element did not have to be refined to achieve convergence as element size approached zero. The only refinement required for convergence was the angular width of the element, which represents an improvement over the conventional conforming element. This element required refinement of both size parameters with the aspect ratio held fixed (equal to one) to achieve convergence. Consequently, for a desired degree-of-accuracy more elements and larger degrees-of-freedom were needed for the bilinear element than for the new element. This translated into more computer core-storage requirements and longer processing time to solve

a given problem.

The differences between the two conforming elements used for this problem showed the advantage of using elements with trial functions which resemble the expected form of the solution. This idea could be extended to the airfoil problem, or for that matter, any problem, providing the behavior of the solution is known. The solution for the airfoil problem at least in the farfield behaves like  $1/r$ . It may be possible to use rational trial functions (perhaps raised to some power) to approximate the solution and achieve an element with improved characteristics.

The utility of the new element is not fully realized for solving circular cylinder problems, but can be realized when solving airfoil problems. The sector element could be used to discretize the flowfield from one chord-length or other specified radius on out to the farfield boundary. Since the trial function for the sector element automatically satisfies the infinity condition (as  $r \rightarrow \infty$ ), then the boundary could be extended as far as necessary to approximately satisfy the boundary condition there. It is also possible that an infinite element could be developed from this element by neglecting the polynomial terms in the trial function. These elements could prove quite useful in this respect since a farfield boundary condition given by eq 50 would not have to be used, and the dreadful nonlinear term that requires integration over the flowfield would not have to be evaluated.

Circulation. The two conforming sector elements were used to solve the problem of incompressible flow with circulation. A splitting technique was employed which permitted the Kutta or

stagnation condition to be enforced in a convenient manner after the elementary or component solutions were obtained. Both elements predicted results accurately. In general, the new element was more efficient and required less refinement for a given degree-of-accuracy. The circulation could be predicted with its use to within 0.003% of the exact value for coarse discretizations. This degree-of-accuracy is possible only when the discretization is constructed in such a manner that the stagnation point is located at the angular centroid of the stagnation element. As the stagnation point is moved toward the edge of the element the error in circulation increases, and reaches a maximum when the stagnation point lies on a node. Velocity distributions were accurately predicted by both elements whenever the circulation was correctly predicted.

Compressible Flow. The new sector element was used to solve the small-disturbance equation for compressible, potential flow over the cylinder. The equation was locally linearized by an iterative solution scheme which converged rapidly for subsonic flows. The scheme failed to converge for transonic flows when the supersonic zone engulfed at least one complete element. Predictions of the critical Mach number and subsonic velocity distributions compared well with known results.

#### Thin Airfoil

Bilinear rectangular elements were used exclusively to discretize the flow domain for the airfoil problem. Cases of incompressible flow and compressible subsonic and transonic flows were considered for a nonlifting symmetric airfoil. The governing nonlinear equation was



written as a sequence of linear equations with variable coefficients and was solved by an iterative process. The iterative solution algorithm converged very rapidly for low subsonic flows. As the Mach number approached a critical value the rate of convergence decreased. For Mach numbers slightly below critical, convergence still occurred in less than twelve iterations. Convergence continued to occur as the Mach number was increased until more than half of one element became engulfed in the supersonic region. At this point the iterative scheme oscillated about some solution and diverged for still larger Mach numbers.

To achieve convergence for transonic flows (mixed elliptic-hyperbolic), the finite element formulation had to be modified to account for the proper zones of influence for those elements within the supersonic (hyperbolic) region. Several modifying methods including those reported by other investigators were tried. All but one method failed to produce the desired result. This method is a new upwinding technique governed by two parameters which exclude the influence of iterative downwind forces on the solution at upwind nodes. The new upwinding technique not only keeps the iterative solution scheme from diverging, but it also captures the weak compression shock which forms in the flowfield.

Accurate approximations for pressure distributions were obtained for all flow regimes from incompressible to transonic flows. The simplifying assumptions and approximations used in this study represents an exceedingly basic approach to an extremely complex nonlinear problem. One of the original intents was to demonstrate whether a simple approach was acceptable. The finite element

techniques used in this study represent approaches that are about as basic as one could take. Excluding the use of linear triangular elements, it would be difficult to conceive of a more fundamental way to solve the nonlinear small-disturbance equation than the way it was done in this study. More complicated problem formulations as well as higher orders of approximation could be used. Some of these approaches are described in the remaining section.

### Recommendations for Future Work

Further development of finite element methods for airfoil analysis could take numerous directions. Several extensions to the present effort could be made, as well as, additional approaches to the problem. Future work will undoubtedly be conducted in the areas of: problem formulation, element development, application of existing higher-order elements, singular treatment of the leading edge, unsteady analysis, and special treatment for the mixed or transonic problem. Each of these areas will be discussed briefly with specific suggestions for development programs.

Problem Formulations. For steady flow three additional inviscid formulation techniques could be investigated. They are the velocity formulation for small-disturbance theory and both velocity and potential formulations for large disturbances.

The small-disturbance potential equation used in this study can alternatively be written as two equations in terms of the disturbance velocities ( $u, v$ ) as

$$\left[1 - M_\infty^2 - M_\infty^2(1 + \gamma)u\right] u_{,x} + v_{,y} = 0 \quad (66)$$

and

$$u_{,y} - v_{,x} = 0 \quad (67)$$

Boundary conditions are

$$v = (1 + u) \frac{df}{dx} \quad (68)$$

and

$$(u, v) \rightarrow 0 \quad \text{as} \quad r \rightarrow \infty \quad (69)$$

These conditions are Dirichlet conditions which are imposed upon the trial functions. The manner in which the boundary conditions are treated using this formulation technique differs from the small-disturbance potential formulation used in this study. The present boundary conditions are of the Neumann type which are not imposed on the trial function. They are, instead, enforced indirectly by the formulation procedure.

The velocity formulation with the use of linear elements as used in this study would provide pressure distributions along the airfoil contour that are linear and continuous, without jumps between elements. This would be an improvement over the potential formulation which results in pressure distributions that are step-functions for linear elements and step-linear-functions for quadratic elements. To achieve continuous pressure distributions from the potential formulation Hermite polynomials would have to be used as approximation functions. Along with the improved accuracy of the velocity formulation over the potential formulation comes the disadvantage that twice as many degrees-of-freedom are needed for linear element discretizations. Two unknowns  $u$  and  $v$  are required as nodal parameters instead of the single parameter  $\phi$ .

The other problem formulations which should be further investigated are the full-potential and alternatively full-velocity formulations. The full-potential equation for inviscid compressible flow is

given by eq 15. This equation could be cast into velocities  $u$  and  $v$  and used in conjunction with the irrotational condition. These formulations would not be limited to slender aerodynamic bodies, since large disturbances are not excluded by assumption. However, non-linearity is more severe than for the small-disturbance equation which will create numerical difficulties. As a first approximation, at least for subsonic flow, the equation could be cast into an iterative Poisson equation. Perhaps an upwinding technique similar to that used in this study could also be tried for supercritical flow. Other solution possibilities exist which should be investigated.

Higher Order Elements. A direct extension of the present study is possible by using higher order elements to approximate the solution. Initially, only those elements along the airfoil contour should be made of higher order with all other elements remaining bilinear. This arrangement would permit an improvement in the description of the pressure distribution along the airfoil contour without significantly increasing the total number of nodal parameters. As a further extension, all elements could be of higher order. Results from these solutions could be compared with those of this study to determine the rate of convergence. ( $p$ -type convergence).

Boundary Conditions. Extensions to the present solutions could be made by applying the tangential boundary condition along the airfoil surface rather than along  $y=0^{\pm}$ , as done in thin-airfoil theory. This improvement is not expected to alter results very much for thin-airfoils, but would be necessary for thick ones. A number of approximations are possible. First, the actual boundary shape could be approximated by suitably shaped elements with the boundary condition

applied along the appropriate element edge. Secondly, isoparametric elements with one side shaped to approximate the contour shape are possible. Of these types several possibilities exist depending on the order of the element chosen and the actual contour shape.

Arbitrary Thin-Airfoil Shapes. For the present approach a computational subroutine needs to be developed to extend the present analysis for an arbitrarily shaped airfoil. Two extensions are required to accomplish this goal. First, the nonlinear form of the governing differential equation will have to be included for lifting flow. This addition will also require the inclusion of an upwinding technique when the flow is transonic. These additions will follow the analysis presented for the symmetric transonic case identically, except the lower half-space will be included. As a consequence, integration along the lower airfoil surface will have to be included. Secondly, an algorithm will have to be added to the subroutine to compute the finite element vectors and matrices that come from the boundary integrals along the airfoil profile. These computations will have to be made from normalized airfoil profile coordinates. Since the boundary integrals depend on the airfoil slope then a procedure to accurately describe the slope from profile coordinates is needed. For a family of airfoils which can be defined by an equation with perhaps variable coefficients the integral can be computed exactly (numerical integration may be easier). A separate routine would be needed for each equation (family) type with the coefficients as input parameters.

New Elements. An interesting study would be to attempt development of new elements for compressible flow problems which have properties similar to the new element used in this study for

incompressible flow about a circular cylinder. The first attempt might be for the circular cylinder; although, the thin-airfoil may be easier, due to the decrease in nonlinearity. Trial functions should be attempted which resemble the form of the solution. For the cylinder problem, forms with  $(1/r)^g$  might be attempted where  $g$  is variable. For the airfoil problem, forms with  $(1/x)^g$  and  $(1/\rho, y)^g$  could be tried. Perhaps, terms which vary as the farfield expression [i.e.  $x/(x^2 + (\rho, y)^2)$ ] could also be included.

Shock Elements. An area which has not been successfully treated with finite element methods for 2-D problems is the correct treatment of shock waves. Shock fitting techniques could be developed, but a better and more elegant technique would be to develop a "special" shock element to capture both the location and strength of the shock. Such an element would have to be constructed from discontinuous functions. Since the location of the shock is not known a priori, the element would have to be sufficiently general to exclude shocks if they do not appear and describe their strength and relative location within the element when they do appear. These "special" elements would be used only in the region of anticipated shock occurrence.

Singularities. For airfoils with sharp leading edges or other slope discontinuities along the contour there will be local singularities. Rather than discretizing these regions with extremely small elements to describe the rapid change of behavior, a local subregion could be isolated to treat the singularity separately. The use of "special" shape functions which describe the singularity near the singular point could be included in the finite element analysis. This technique has been done in applications of other singular problems, such as the stress

concentration near a crack tip.

Unsteady Analysis. Chan's et. al. work is the only extensive unsteady analysis to appear in the literature. Additional finite element solutions for this problem are required. A number of approaches and formulation procedures are possible. One particular approach which should be tried for the small-disturbance equation is to assume that the potential can be expressed as

$$\phi(x, y, t) = N_i(x, y) \phi_i(t) \quad (70)$$

The spacial shape functions  $N_i(x, y)$  are the same as those used for the steady problem. What is different is the nodal parameters  $\phi_i(t)$  are functions of time. Instead of obtaining a set of algebraic equations to solve, a set of ordinary second-order differential equations will result for the nodal parameters. For small oscillations about the mean steady position these equations will be linear and can be solved by existing methods.



### Bibliography

1. Krupps, J. A. and Murman, E. M. "Computations of Transonic Flows Past Lifting Airfoils and Slender Bodies," AIAA Journal, 10: 880-886 (1972).
2. Zienkiewicz, O. and Cheung, Y. K. "Finite Elements in the Solution of Field Problem," The Engineer (Sept 1965).
3. Martin, H. C. "Finite Element Analysis of Fluid Flow," AFFDL-TR-68-150: (December 1969).
4. deVries, G. and Norrie, D. H. "The Application of the Finite Element Technique to Potential Flow Problems: Part I," University of Calgary, Mech. Eng. Dept. Report No. 7: (August 1969).
5. deVries, G. and Norrie, D. H. "The Application of the Finite Element Technique to Potential Flow Problems: Part II," University of Calgary, Mech. Eng. Dept. Report No. 8: (July 1969).
6. deVries, G. and Norrie, D. H. "The Application of the Finite Element Technique to Potential Flow Problems: Part III," University of Calgary, Mech. Eng. Dept. Report No. 9: (June 1973).
7. deVries, G. and Norrie, D. H. "Application of the Finite Element Technique to Potential Flow Problems," Journal of Applied Mechanics: 798-802 (December 1971).
8. Norrie, D. H. and deVries, G. The Finite Element Method. N. Y.: Academic Press, 1973.
9. Shen, S. F. "An Aerodynamicist Looks at the Finite Element Method," Finite Elements in Fluids Vol 2. N. Y.: John Wiley, 1975.
10. Murman, E. M. and Cole, J. D. "Calculations of Plane Steady Transonic Flows," AIAA Journal, 9: 114-120 (1971).
11. Periaux, J. "Three Dimensional Analysis of Compressible Potential Flows with the Finite Element Method," International Journal for Numerical Methods in Engineering, 9: 775-831 (1975).
12. Shen, S. F. and Habashi, W. G. "Local Linearization of the Finite Element Method and its Application to Compressible Flows," International Journal for Numerical Methods in Engineering, 10: 565-577 (1975).
13. Chan, S.T.K. and Brashears, M. R. Analysis of Steady and Unsteady Transonic Flows by Finite Element Method. AFFDL-TR-74-11. WPAFB, Ohio: March 1974.
14. Chan, S.T.K. and Brashears, M. R. Analysis of Steady and Unsteady Transonic Flows by Finite Element Method. NASA CR 144930: January 1976.

15. Chan, S.T.K. et al. Finite Element Analysis of Transonic Flows Over Thin Airfoils, Vol I. AFFDL-TR-76-49-Vol I. WPAFB, Ohio: May 1976.
16. Chan, S.T.K. et al. Finite Element Analysis of Transonic Flows Over Thin Airfoils, Vol II. AFFDL-TR-76-49-Vol II. WPAFB, Ohio: May 1976.
17. Chan, S.T.K., and Chan, H. C. "Finite Element Applications to Unsteady Transonic Flow," AIAA/ASME 18th Structures, Structural Dynamics & Materials Conference. San Diego: March 1977.
18. Klunker, E. B. Contributions to Methods for Calculating the Flow About Thin Lifting Wings at Transonic Speeds -- Analytical Expressions for the Farfield. NASA TN-D-6530: November 1971.
19. Landahl, M. T. Unsteady Transonic Flow. N. Y.: Pergamon Press, 1961.
20. Wellford, L. C. and Hafez, M. M. "Implicit Velocity Formulations for the Calculation of Transonic Flow by the Finite Element Method," Proceedings of the Symposium on Application of Computer Methods in Engineering. August 1977.
21. Wellford, L. C. and Hafez, M. M. An Implicit Velocity Formulation for the Small-Disturbance Transonic Flow Problem Using Finite Elements. Flow Research Report No. 81: May 1977.
22. Ecer, A. et al. "On the Solution of Hyperbolic Equations Using Finite Element Methods," Proceedings of the Symposium on Applications of Computer Methods in Engineering. August 1977.
23. Aziz, A. K. and Leventhal, S. "The Foundation and Development of the Finite Element Method to Solve Partial Differential Equations in Fluid Mechanics," AGARD Lecture Series No. 86 on Computational Fluid Dynamics. AGARD-LS-86.
24. Akay, H. U. et al. "Finite Element Analysis of Compressible Flow," Proceedings of the Symposium on Applications of Computer Methods in Engineering. August 1977.
25. Strang, G. and Fix, G. S. An Analysis of the Finite Element Method. Englewood Cliffs: Prentice-Hall, Inc., 1973.
26. Mitchell, A. R. and Wait, R. The Finite Element Method in Partial Differential Equations. N. Y.: John Wiley, 1977.
27. Raju, I. S. and Rao, A. K. "Stiffness Matrices for Sector Elements," AIAA Journal, 7: 156-157 (January 1969).
28. Raju, I. S. et al. "Sector Elements for Matrix Displacement Analysis," International Journal for Numerical Methods in Engineering, 6: 553-563 (1973).

29. Imai, I. "On the Flow of a Compressible Fluid Past a Circular Cylinder," Physico-Mathematical Society of Japan: Proceedings, 20: 636-645 (1938).
30. Imai, I. "On the Flow of a Compressible Fluid Past a Circular Cylinder, II", Physico-Mathematical Society of Japan: Proceedings, 23: 180-193, 1941.
31. Habashi, W. G. "A Study of the Finite Element Method for Aerodynamic Applications," PhD Thesis: Cornell University (June 1975).
32. Greenspan, D. Lectures on the Numerical Solution of Linear Singular and Nonlinear Differential Equations. Englewood Cliffs: Prentice-Hall, Inc. 1968.
33. Hafez, M. M. et al. Numerical Computations of Transonic Flow by Finite Element and Finite Difference Methods. Flow Research Report No. 70: January 1977.
34. Hafez, M. M. et al. Finite Element and Finite Differences for Transonic Flow Calculations. NASA Report (No. Unknown) May 1977.
35. Hafez, M. M. et al. Numerical Solution of the Unsteady Transonic Small-Disturbance Equation. Flow Research Report No. 83: August 1977.
36. Ergatoudis, I. "Curved Isoparametric, Quadrilateral Elements for Finite Element Analysis," International Journal of Solids, Structures, 4: 31-42 (1968).
37. Christie, I. "Finite Element Methods for Second Order Differential Equations with Significant First Derivatives," International Journal for Numerical Methods in Engineering, 10: 1389-1396 (1976).
38. Heinrich, J. C. et al. "An 'Upwind' Finite Element Scheme for Two-Dimensional Convective Transport Equation," International Journal for Numerical Methods in Engineering, 11: 131-143 (1977).
39. Knechtel, E. D. Experimental Investigations at Transonic Speeds of Pressure Distributions Over Wedge and Circular -- Arc Airfoil Sections and Evaluation of Perforated-Wall Interference. NASA-TN-D-15: August 1959.
40. Olsen, J. J. and Batill, S. M. Application and Improvement of Finite-Difference Methods in Transonic Nonlifting Flow. AFFDL-TM-73-85-FYS: WPAFB, Ohio (July 1973).
41. Baker, A. J. Finite Element Computational Fluid Mechanics, Vol I. Knoxville: University of Tennessee, 1977.
42. Chung, T. J. Finite Element Analysis in Fluid Dynamics, Vol III. Knoxville: University of Tennessee, 1977.

43. Doctors, L. J. "An Application of the Finite Element Technique to Boundary Value Problems of Potential Flow," International Journal for Numerical Methods in Engineering, 2: 343-352 (1970).
44. Guderley, K. G. The Theory of Transonic Flow. Oxford: Pergamon Press, 1962.
45. Oden, T. J. et al. Finite Element Methods in Flow Problems. Huntsville: UAH Press, 1974.
46. Oden, T. J. et al. Finite Elements in Fluids, Vol 1. N. Y.: John Wiley, 1975.
47. Oden, T. J. et al. Finite Elements in Fluids, Vol 2. N. Y.: John Wiley, 1975.
48. Fix, G. J. A Mixed Finite Element Scheme for Transonic Flows. ICASE Report 76-25, August 1976.
49. Fix, G. J. and Gunzburger, M. D. On Least Squares Approximation to Indefinite Problems of the Mixed Type. ICASE Report 76-27, August, 1976.
50. Fix, G. J. and Gurtin, M. E. "On Patched Variational Principles with Application to Elliptic and Mixed Elliptic-Hyperbolic Problems," (Journal Unknown).
51. Tai, T. C. "Transonic Inviscid Flow over Lifting Airfoils by the Method of Integral Relations," AIAA Journal, 12: (June 1974).
52. Magnus, R. and Yoshihara. "Unsteady Transonic Flow Over an Airfoil," AIAA Journal, 13: 1622-1628 (December 1975).
53. Steger, J. L. and Lomax, H. "Transonic Flow About Two-Dimensional Airfoils by Relaxation Procedures," AIAA Journal, 10: 49-52 (January 1972).
54. Martin, D. E. and Lomax, H., "Rapid Finite-Difference Computations of Subsonic and Slightly Supercritical Aerodynamic Flows," AIAA Journal, 13: 479-486 (May 1975).
55. Garabedian, P. R. and Korn, D. G. "Analysis of Transonic Airfoils," Comm. on Pure and Applied Mathematics, Vol 24, 1971, pp 841-851.
56. Jameson, A. "Iterative Solution of Transonic Flow over Airfoils and Wings, Including Flows at Mach 1," Comm. on Pure and Applied Mathematics, Vol 27, 1974, pp 283-309.
57. Nieuwland, G. Y. and Spec, B. M. "Transonic Airfoils: Recent Developments in Theory, Experiment, and Design," Annual Review of Fluid Mechanics, Annual Review Inc. 1973, pp. 119-150.
58. Bisplinghoff, R. L. and Ashley, H. Principles of Aeroelasticity. N. Y.: John Wiley, 1962.

59. Zienkiewicz, O. C. The Finite Element Method in Engineering Science. London: McGraw-Hill, 1971.
60. Olsen, J. J. Subsonic and Transonic Flow Over Sharp and Round Nosed Nonlifting Airfoils. PhD Dissertation, Ohio State University, 1976.

## Appendix A

### Shape Functions and Elemental Equations for Sector Element (1)

This appendix contains a description of how shape or basis functions are derived from assumed trial functions. The description primarily pertains to elements used to solve the potential flow problems formulated in Chapter III for the circular cylinder. This appendix also contains the derivation of finite element equations for the symmetric flow case when sector element (1) is used.

#### Shape Functions

In general, when a continuum problem is solved by the Finite Element Method, the continuum is divided into a finite number of elements which are connected at discrete points situated on their boundaries called nodes. The continuum which has infinite degrees-of-freedom is replaced by a finite number of unknown nodal parameters. These parameters are nodal-point values of the solution function or its derivatives, depending upon the complexity of the approximation desired. Between nodes (i.e. inside an element) the solution function is approximated by an assumed functional relationship which can be expressed in terms of the unknown nodal parameters. The approximating function (trial function) can be written as a linear combination of the shape functions and the unknown nodal parameters. For example, consider the incompressible flow problem described in Chapter III. An assumed trial function for the sector element shown in Fig 3 can be written as

$$\phi^e(r, \theta) = N_j(r, \theta) \phi_j^e \quad (A-1)$$

where  $N_j(r, \theta)$  are the basis functions and  $\phi_j^e$  the nodal value of the solution  $\phi$  at node  $j$ . The repeated index  $j$  implies summation from  $j = 1, \dots, 4$ . It is immediately apparent that the shape function should have the property that

$$N_i(r_j, \theta_j) = \delta_{ij} \quad (A-2)$$

where  $\delta_{ij}$  is the Kronecker delta. For simple elements it is often easy to select a functional form for the solution and with the use of the above property simply write down the basis functions. To insure that the guessed form produces a conforming element, the required continuity conditions have to be satisfied. For more complicated approximations the guess technique may not work very well, and a more direct method will have to be used (Ref 59). When using the direct method, the assumed trial function must be written with as many undetermined constants as there are nodal parameters in the element. It could be expressed as

$$\phi(r, \theta) = G(r, \theta; a_1, \dots, a_n) \quad (A-3)$$

where  $(r, \theta)$  are independent variables and the  $a$ 's are undetermined constants. What is done for the Finite Element Method is to express these constants as functions of the element geometry and the unknown nodal parameters  $\phi_j, (j = 1, \dots, n)$ . This process is started by first writing eq A-3 at each node to give a system of  $n$  equations expressed as

$$\phi_i = \hat{G}_{ij} a_j \quad (A-4)$$

The constants are expressed in terms of the nodal parameters by

inverting  $\hat{G}_{ij}$  to give

$$a_i = \hat{G}_{ij}^{-1} \phi_j \quad (\text{A-5})$$

Substituting the constants into the trial function, eq A-3, and collecting terms will produce an expression in the form of eq A-1.

To illustrate the direct process, consider trial function (1) for the sector element shown in Fig 3. Trial function (1) is given in Chapter III by eq 35 as

$$\phi(r, \theta) = a_1 + b_1 \frac{\sin \theta}{r} + c_1 \frac{\cos \theta}{r} + d_1 \theta \quad (35)$$

Expressing  $\phi$  at each of the nodes gives a system of 4 equations for the 4 unknown nodal values of  $\phi$ . These equations are expressed in matrix form as

$$\begin{Bmatrix} \phi_1 \\ \phi_2 \\ \phi_3 \\ \phi_4 \end{Bmatrix} = \begin{bmatrix} 1 & \frac{\sin \theta_a}{r_a} & \frac{\cos \theta_a}{r_a} & \theta_a \\ 1 & \frac{\sin \theta_a}{r_b} & \frac{\cos \theta_a}{r_b} & \theta_a \\ 1 & \frac{\sin \theta_b}{r_b} & \frac{\cos \theta_b}{r_b} & \theta_b \\ 1 & \frac{\sin \theta_b}{r_a} & \frac{\cos \theta_b}{r_b} & \theta_b \end{bmatrix} \begin{Bmatrix} a_1 \\ b_1 \\ c_1 \\ d_1 \end{Bmatrix} \quad (\text{A-6})$$

Inverting this matrix, substituting the constant into eq 35, and collecting like terms of  $\phi_j$  will produce the desired form. The resulting shape functions are



$$N_1 = \frac{\frac{\beta \sin(\theta_b - \theta)}{r/r_b} - (\theta_b - \theta) \sin \beta}{\beta(\alpha - 1) \sin \beta} \quad (\text{A-7a})$$

$$N_2 = \frac{\frac{-\beta \sin(\theta_b - \theta)}{r/r_b} + \alpha(\theta_b - \theta) \sin \beta}{\beta(\alpha - 1) \sin \beta} \quad (\text{A-7b})$$

$$N_3 = \frac{\frac{-\beta \sin(\theta - \theta_a)}{r/r_b} + \alpha(\theta - \theta_a) \sin \beta}{\beta(\alpha - 1) \sin \beta} \quad (\text{A-7c})$$

$$N_4 = \frac{\frac{\beta \sin(\theta - \theta_a)}{r/r_b} - (\theta - \theta_a) \sin \beta}{\beta(\alpha - 1) \sin \beta} \quad (\text{A-7d})$$

where  $\beta = \theta_b - \theta_a$  and  $\alpha = r_b/r_a$  as defined in Fig 3. It is easily demonstrated that the shape functions satisfy  $N_i(r_j, \theta_j) = \delta_{ij}$ . However, further examination reveals that continuity of  $\phi$  across inter-element boundaries is guaranteed only along radial lines. Along circumferential lines  $\phi$  is continuous only at the nodal points. The use of this element for the second order problem of incompressible flow over a circular cylinder as formulated in Chapter III will give a non-conforming approximation.

#### Elemental Equations

The elemental equations for incompressible flow over a circular cylinder are expressed by eq 30 as  $K_{ij}^e \phi_j^e = f_i^e$  for  $(i, j = 1, \dots, 4)$ . Stiffness matrix  $K_{ij}^e$  is given by eq 31 as

$$K_{ij}^e = \iint_{\Omega_e} (N_{i,r} N_{j,r} + r^2 N_{i,\theta} N_{j,\theta}) r dr d\theta \quad (31)$$

Each element of  $K_{ij}^e$  is calculated by substituting the shape functions and performing the required integration. For example, the  $K_{11}^e$  component of  $K_{ij}^e$  is obtained by setting  $i = j = 1$ , and substituting eq A-7a into eq 31. The result is

$$K_{11}^e = \int_{\theta_a}^{\theta_b} \int_{r_a}^{r_b} \frac{1}{\Delta^2} \left[ \frac{\beta^2}{r^3} - \frac{2\beta}{r_b r^2} \sin \beta \cos(\theta_b - \theta) + \frac{\sin^2 \beta}{r_b^2 r} \right] r dr d\theta \quad (A-8)$$

where

$$\Delta = \frac{\beta(\alpha - 1) \sin \beta}{r_b}$$

Integrating and substituting the limits gives

$$K_{11}^e = \frac{\beta(\alpha+1)}{2(\alpha-1)\sin^2\beta} - \frac{2}{\beta(\alpha-1)} + \frac{\ln\alpha}{\beta(\alpha-1)^2} \quad (A-9)$$

Note that  $K_{11}^e$  depends only upon the two elemental geometric parameters  $\alpha$  and  $\beta$ .

The remaining elements of  $K_{ij}^e$  are obtained in a similar manner to give a symmetric stiffness matrix of the form

$$K_{ij}^e = \begin{bmatrix} K_1 & K_2 & K_3 & K_4 \\ & K_1 & K_5 & K_3 \\ & & K_1 & K_2 \\ & & & K_1 \end{bmatrix} \quad (A-10)$$

where

$$K_1 = a - \frac{2}{b} + \frac{c}{\beta}$$

$$K_2 = -a + \frac{\alpha+1}{b} - \frac{\alpha}{\beta}c$$

$$K_3 = a\cos\beta - \frac{\alpha+1}{b} + \frac{\alpha}{\beta}c$$

$$K_4 = -a\cos\beta + \frac{2}{b} - \frac{c}{\beta}$$

$$K_5 = -a\cos\beta + \frac{2\alpha}{b} - \frac{\alpha^2}{\beta}c$$

The constants  $a, b, c$  are given by

$$a = \frac{\beta(\alpha+1)}{2(\alpha-1)} \frac{1}{\sin^2 \beta}$$

$$b = \beta(\alpha-1)$$

$$c = \frac{\ln \alpha}{(\alpha-1)^2}$$

The force vector  $f_i^e$  is given by eq 39 as

$$f_i^e = \int_{\theta_a}^{\theta_b} N_i \cos \theta \bigg|_{r=r_a=1} d\theta \quad (39)$$

Substituting the shape functions eq A-7 into this expression and integrating gives

$$f_1^e = \frac{\beta}{2D} [A \sin \theta_b - B \cos \theta_b] \\ + \frac{\sin \beta}{Dr_b} [\beta \sin \theta_a + c]$$

$$f_2^e = \frac{1}{D} [-\sin \beta (\beta \sin \theta_a + c) \\ + \frac{\beta}{2} (B \cos \theta_b - A \sin \theta_b)]$$

$$f_3^e = \frac{1}{D} \left[ \sin \beta (\beta \sin \theta_a + C) - \frac{\beta}{2} (B \cos \theta_a - A \sin \theta_a) \right]$$

$$f_4^e = \frac{-\beta}{2D} \left[ A \sin \theta_a - B \cos \theta_a \right] - \frac{\sin \beta}{Dr_b} \left[ \beta \sin \theta_b + C \right]$$

The constants  $A, B, C, D$  are given by

$$A = \frac{\sin 2\theta_b - \sin 2\theta_a}{2} + \beta$$

$$B = \sin^2 \theta_b - \sin^2 \theta_a$$

$$C = \cos \theta_b - \cos \theta_a$$

$$D = \frac{\beta(\alpha-1)\sin \beta}{r_b}$$

### Velocity Distribution

The dimensionless tangential perturbation velocity  $u_\theta(1, \theta)$  along the contour of the cylinder is calculated from the potential function. In element  $e$ ,  $\phi^e(r, \theta)$  is given by eq 28

$$\phi^e(r, \theta) = N_i(r, \theta) \phi_i^e \quad (28)$$

Velocity  $u_\theta^e$  in each element is defined from the potential function by

$$u_\theta^e = \frac{1}{r} \phi_{, \theta}^e$$

Along the cylinder surface ( $r=1$ )

$$u_\theta^e(1, \theta) = N_{i, \theta}(1, \theta) \phi_i^e \quad (A-12)$$

Substituting the shape functions eq A-7 into eq A-12 and evaluating at  $r=1$  gives

$$\begin{aligned} u_\theta^e(1, \theta) = \frac{1}{\Delta} & \left[ \beta \cos(\theta_b - \theta) (\phi_2^e - \phi_1^e) \right. \\ & + \sin \beta (\phi_1^e - \phi_2^e + \phi_3^e - \phi_4^e) \\ & \left. + \beta \cos(\theta - \theta_a) (\phi_4^e - \phi_3^e) \right] \end{aligned} \quad (A-13)$$

where

$$\Delta = \frac{\beta(\alpha-1)}{r_b} \sin \beta$$

## Appendix B

### Shape Functions and Elemental Equations for Sector Element (2)

#### Shape Functions

Consider the sector element shown in Fig 3 and trial function (2) given by

$$\phi^e(r, \theta) = a_2 + b_2 r + c_2 \theta + d_2 r \theta \quad (36)$$

From Ref (27) this approximation can be written in the form  $\phi^e = N_j \phi_j^e$   $j = 1, \dots, 4$  where

$$N_1 = \frac{r/r_a - \alpha}{1 - \alpha} \frac{\theta_b - \theta}{\beta} \quad (B-1a)$$

$$N_2 = \frac{r/r_a - 1}{\alpha - 1} \frac{\theta_b - \theta}{\beta} \quad (B-1b)$$

$$N_3 = \frac{r/r_a - 1}{\alpha - 1} \frac{\theta - \theta_a}{\beta} \quad (B-1c)$$

$$N_4 = \frac{r/r_a - \alpha}{1 - \alpha} \frac{\theta - \theta_a}{\beta} \quad (B-1d)$$

The shape functions could also be obtained by the direct procedure described in Appendix A. It is easily demonstrated that the shape functions provide continuity of  $\phi$  across inter-element boundaries. Thus, element (2) is a conforming element for the finite element formulations described in Chapter III.

### Elemental Equations

The elemental equations for incompressible flow over a circular cylinder are expressed by eq 30 as  $K_{ij}^e \phi_j^e = f_i^e$ , ( $i, j = 1, \dots, 4$ ). Stiffness matrix  $K_{ij}^e$  is given by eq 31 as

$$K_{ij}^e = \int_{\theta_a}^{\theta_b} \int_{r_a}^{r_b} (N_{i,r} N_{j,r} + \frac{1}{r^2} N_{i,\theta} N_{j,\theta}) r dr d\theta \quad (31)$$

Each element of  $K_{ij}^e$  is calculated by substituting the corresponding shape functions and integrating. For example, the  $K_{11}^e$  component of  $K_{ij}^e$  is obtained by setting  $i = j = 1$  and substituting eq B-1a into eq 31.

The result is

$$K_{11}^e = \int_{\theta_a}^{\theta_b} \int_{r_a}^{r_b} \left\{ \left[ \frac{\theta_b - \theta}{\beta r_a (1 - \alpha)} \right]^2 + \left[ \frac{1}{r \beta} \frac{r/r_a - \alpha}{1 - \alpha} \right]^2 \right\} r dr d\theta \quad (B-2)$$

Integrating and substituting the limits gives

$$K_{11}^e = \frac{\beta(\alpha+1)}{6(\alpha-1)} + \frac{1-3\alpha}{2\beta(\alpha-1)} + \frac{\alpha^2 \ln \alpha}{\beta(\alpha-1)^2} \quad (B-3)$$

which depends only upon the two elemental geometric parameters  $\alpha$  and  $\beta$ .

The remaining elements of  $K_{ij}^e$  are obtained in a similar manner to give a symmetric stiffness matrix of the form

$$K_{ij}^e = \begin{bmatrix} K_1 & K_2 & K_3 & K_4 \\ & K_5 & K_6 & K_3 \\ & & K_5 & K_2 \\ & & & K_1 \end{bmatrix} \quad (B-4)$$



where

$$\begin{aligned} K_1 &= a + \alpha^2 c - e & K_4 &= a/2 - \alpha^2 c + e \\ K_2 &= -a - \alpha c + d & K_5 &= a + b + c \\ K_3 &= -a/2 - \alpha c + d & K_6 &= a/2 - b - c \end{aligned}$$

The constants  $a, \dots, e$  in the above expressions are given by

$$\begin{aligned} a &= \frac{\beta(\alpha+1)}{6(\alpha-1)} & d &= \frac{\alpha+1}{2\beta(\alpha-1)} \\ b &= \frac{\alpha-3}{2\beta(\alpha-1)} & e &= \frac{3\alpha-1}{2\beta(\alpha-1)} \\ c &= \frac{\ln \alpha}{\beta(\alpha-1)^2} \end{aligned}$$

The force vector  $f_i^e$  is given by eq 39 as

$$f_i^e = \int_{\theta_a}^{\theta_b} N_i \cos \theta \Big|_{r=r_a=1} d\theta \quad (39)$$

Substituting the shape functions, eq B-1, into this expression and integrating gives

$$f_i^e = \left\{ \begin{array}{c} -\sin \theta_a - \frac{\cos \theta_b - \cos \theta_a}{\beta} \\ 0 \\ 0 \\ \sin \theta_b + \frac{\cos \theta_b - \cos \theta_a}{\beta} \end{array} \right\} \quad (B-5)$$

The above expressions define  $f_i^e$  for each element  $e$  which borders the cylinder surface. For all other elements  $f_i^e$  is identically zero.

### Velocity Distribution

The dimensionless tangential perturbation velocity  $u_\theta(1, \theta)$  along the contour of the cylinder is calculated from the potential function. In element  $e$ ,  $\phi^e(r, \theta)$  is given by eq 28

$$\phi^e(r, \theta) = N_i(r, \theta) \phi_i^e \quad (28)$$

Velocity  $u_\theta^e$  in each element is defined from the potential function by

$$u_\theta^e(r, \theta) = N_{i,\theta}(r, \theta) \phi_i^e$$

Along the cylinder surface ( $r = 1$ )

$$u_\theta^e(1, \theta) = N_{i,\theta}(1, \theta) \phi_i^e \quad (B-6)$$

For each of the conformal elements this expression reduces to

$$u_\theta^e(1, \theta) = \frac{1}{\beta} (\phi_4^e - \phi_1^e) \quad (B-7)$$

Within element  $e$  the tangential velocity along the contour is a constant. Thus, between elements there will be a jump in  $u_\theta$ . This implies the velocity distribution is a step function along the contour. The tangential velocity defined by eq B-7 for element (2) is also the tangential velocity for element (3) described in the next appendix.

## Appendix C

### Shape Function and Elemental Equations for Sector Element (3)

#### Shape Functions

Consider the sector element shown in Fig 3 and trial function (3) given by

$$\phi^e(r, \theta) = a_3 + \frac{b_3}{r} + c_3 \theta + \frac{d_3 \theta}{r} \quad (37)$$

This approximation can be written in the form  $\phi^e = N_j \phi_j^e$  for  $(j = 1, \dots, 4)$  where

$$N_1 = \frac{r_a/r + 1/\alpha}{1 - 1/\alpha} \frac{\theta_b - \theta}{\beta} \quad (C-1a)$$

$$N_2 = \frac{r_a/r - 1}{1/\alpha - 1} \frac{\theta_b - \theta}{\beta} \quad (C-1b)$$

$$N_3 = \frac{r_a/r - 1}{1/\alpha - 1} \frac{\theta - \theta_a}{\beta} \quad (C-1c)$$

$$N_4 = \frac{r_a/r - 1/\alpha}{1 - 1/\alpha} \frac{\theta - \theta_a}{\beta} \quad (C-1d)$$

These shape functions are determined from the trial function by the method described in Appendix A. They can also be deduced from the shape functions in Appendix B by inverting  $r$  and  $\alpha$ . This element represents a new element which to the author's knowledge has not been used to solve an aerodynamics problem.

#### Elemental Equations

Incompressible Flow. The elemental equations for incompressible

flow over a circular cylinder are expressed by eq 30 as

$$K_{ij}^e \phi_j^e = f_i^e \quad (i, j = 1, \dots, 4) \quad (30)$$

Stiffness matrix  $K_{ij}^e$  is given by eq 31 as

$$K_{ij}^e = \int_{\theta_a}^{\theta_b} \int_{r_a}^{r_b} \left( N_{i,r} N_{j,r} + \frac{1}{r^2} N_{i,\theta} N_{j,\theta} \right) r dr d\theta \quad (31)$$

Each element of  $K_{ij}^e$  is calculated by substituting the corresponding shape functions and integrating. For example the  $K_{11}^e$  component of  $K_{ij}^e$  is obtained by setting  $i = j = 1$  and substituting eq C-2a into eq 31. The result is

$$K_{11}^e = \int_{\theta_a}^{\theta_b} \int_{r_a}^{r_b} \left\{ \frac{1}{r^3} \left[ \frac{\alpha r_a (\theta_b - \theta)}{\beta (\alpha - 1)} \right]^2 + \frac{1}{r} \left[ \frac{\alpha r_a / r - 1}{\beta (\alpha - 1)} \right] \right\} r dr d\theta$$

Integrating and substituting the limits gives

$$K_{11}^e = \frac{\beta (\alpha + 1)}{6 (\alpha - 1)} + \frac{\alpha - 3}{2 \beta (\alpha - 1)} + \frac{\ln \alpha}{\beta (\alpha - 1)^2} \quad (C-2)$$

which depends only upon the two elemental geometric parameters  $\alpha$  and  $\beta$ .

The remaining elements of  $K_{ij}^e$  are obtained in a similar manner to give a symmetric stiffness matrix of the form

$$K_{ij}^e = \begin{bmatrix} K_1 & K_2 & K_3 & K_4 \\ & K_5 & K_6 & K_3 \\ & & K_5 & K_2 \\ & & & K_1 \end{bmatrix} \quad (C-3)$$

The elements of  $K_{ij}^e$  are given by

$$K_1 = a + b + c$$

$$K_4 = a/2 - b - c$$

$$K_2 = -a - \alpha c + d$$

$$K_5 = a + \alpha^2 - c$$

$$K_3 = -a/2 + \alpha c - d$$

$$K_6 = a/2 - \alpha^2 c + e$$

The constants  $a, \dots, e$  in the above expressions are given by

$$a = \frac{\beta(\alpha+1)}{6(\alpha-1)}$$

$$d = \frac{\alpha+1}{2\beta(\alpha-1)}$$

$$b = \frac{\alpha-3}{2\beta(\alpha-1)}$$

$$e = \frac{3\alpha-1}{2\beta(\alpha-1)}$$

$$c = \frac{\ln \alpha}{\beta(\alpha-1)^2}$$

The force vector  $f_i^e$  is given by eq 39 as

$$f_i^e = \int_{\theta_a}^{\theta_b} N_i \cos \theta \bigg|_{r=r_a=1} d\theta \quad (39)$$

Substituting the shape functions, eqs C-1, into this expression and integrating gives

$$f_i^e = \left\{ \begin{array}{c} -\sin \theta_a - \frac{\cos \theta_b - \cos \theta_a}{\beta} \\ 0 \\ 0 \\ \sin \theta_b + \frac{\cos \theta_b - \cos \theta_a}{\beta} \end{array} \right\} \quad (C-4)$$

The above expression defines  $f_i^e$  for each element  $e$  which borders the cylinder surface. For all other elements  $f_i^e$  is identically zero.

Compressible Flow. For compressible flow over the cylinder the elemental equations are given by eq 44 as

$$[K_{ij} + L_{ij}(\phi^n)] \phi_j^{n+1} = f_i + g_i(\phi^n) \quad (C-5)$$

Matrix  $K_{ij}$  and vector  $f_i$  are the same as defined for the incompressible problem. Matrix  $L_{ij}(\phi^n)$  comes from the nonlinear term in the governing differential equation, and is given by eqs 47 and 48. It can be expressed as

$$L_{ij}(\phi^n) = -M_\infty^2 [1 + K^n(1+\gamma)] (A_{ij} + B_{ij} - C_{ij} + D_{ij}) \quad (C-6)$$

where

$$A_{ij} = \iint_{\Omega_e} \cos^2 \theta N_{i,r} N_{j,r} r dr d\theta$$

$$B_{ij} = \iint_{\Omega_e} \frac{\sin^2 \theta}{r^2} N_{i,\theta} N_{j,\theta} r dr d\theta$$

$$C_{ij} = \iint_{\Omega_e} \frac{\sin \theta \cos \theta}{r} (N_{i,r} N_{j,\theta} + N_{i,\theta} N_{j,r}) r dr d\theta$$

$$D_{ij} = \int_{\partial \Omega_e^c} \frac{\sin \theta \cos \theta}{r} N_i N_{j,\theta} |d\theta|$$

$r = r_a = 1$

Substituting the shape functions, eq C-2, into each of these expressions and integrating gives

$$A_{ij} = \frac{\alpha + 1}{2\beta^2(\alpha - 1)} \begin{bmatrix} a_1 & -a_1 & a_2 & -a_2 \\ & a_1 & -a_2 & a_2 \\ & & a_3 & -a_3 \\ & & & a_3 \end{bmatrix} \quad (C-7)$$

where

$$a_1 = \left[ (\theta^2 - 2\theta_b\theta + \theta_b^2 - 1/2) \frac{\sin 2\theta}{4} + \frac{\theta^3}{6} - \frac{\theta_b\theta^2}{2} + \frac{\theta_b^2\theta}{2} + (\theta - \theta_b) \frac{\cos 2\theta}{4} \right] \bigg|_{\theta_a}^{\theta_b}$$

$$a_2 = \left[ (\theta^2 - (\theta_b + \theta_a)\theta + \theta_a \theta_b - 1/2) \frac{\sin 2\theta}{4} + \left( \theta - \frac{\theta_b + \theta_a}{2} \right) \frac{\cos 2\theta}{4} + \frac{\theta^3}{6} - \left( \frac{\theta_b + \theta_a}{4} \right) \theta^2 + \frac{\theta_a \theta_b}{2} \theta \right] \bigg|_{\theta_a}^{\theta_b}$$

$$a_3 = \left[ (\theta^2 - 2\theta_a \theta + \theta_a^2 - 1/2) \frac{\sin 2\theta}{4} + \frac{\theta^3}{6} - \frac{\theta_a \theta^2}{2} + \frac{\theta_a^2 \theta}{2} + \frac{\theta - \theta_a}{4} \cos 2\theta \right] \bigg|_{\theta_a}^{\theta_b}$$

Matrix  $B_{ij}$  becomes

$$B_{ij} = \begin{bmatrix} b_1 & b_2 & -b_2 & -b_1 \\ & b_3 & -b_3 & -b_2 \\ & & b_3 & b_2 \\ & & & b_1 \end{bmatrix} \quad (C-8)$$

where

$$b_1 = \frac{(\alpha-1) \frac{\alpha-3}{2} + \ln \alpha}{\beta^2 (\alpha-1)^2} \left[ \frac{\theta}{2} - \frac{\sin 2\theta}{4} \right] \bigg|_{\theta_a}^{\theta_b}$$



$$b_2 = \frac{(\alpha^2 - 1) - \alpha \ln \alpha}{\beta^2 (\alpha - 1)^2} \left[ \frac{\theta}{2} - \frac{\sin 2\theta}{4} \right] \bigg|_{\theta_a}^{\theta_b}$$

$$b_3 = \frac{(\alpha - 1) \frac{1 - 3\alpha}{2} + \alpha^2 \ln \alpha}{\beta^2 (\alpha - 1)^2} \left[ \frac{\theta}{2} - \frac{\sin 2\theta}{4} \right] \bigg|_{\theta_a}^{\theta_b}$$

Matrix  $C_{ij}$  becomes

$$C_{ij} = \begin{bmatrix} c_1 & 0 & c_2 & c_3 \\ & -c_1 & -c_3 & -c_2 \\ & & -c_4 & 0 \\ & & & c_4 \end{bmatrix} \quad (C-9)$$

where

$$c_1 = \frac{1}{\beta^2} \left[ \frac{\theta}{4} + \frac{\theta - \theta_b}{4} \cos 2\theta - \frac{\sin 2\theta}{8} \right] \bigg|_{\theta_a}^{\theta_b}$$

$$c_2 = \frac{-1}{8\beta} \left[ 1 - \cos 2\theta \right] \bigg|_{\theta_a}^{\theta_b}$$

$$C_3 = \frac{-1}{\beta^2} \left[ \frac{\theta_b + \theta_a}{8} - \frac{\theta_b + \theta_a - 2\theta}{8} \cos 2\theta - \frac{\sin 2\theta}{8} \right] \bigg|_{\theta_a}^{\theta_b}$$

$$C_4 = \frac{1}{\beta^2} \left[ \frac{\theta_a}{4} + \frac{\theta - \theta_a}{4} \cos 2\theta - \frac{\sin 2\theta}{8} \right] \bigg|_{\theta_a}^{\theta_b}$$

The matrix  $D_{ij}$  comes from the boundary term which becomes

$$D_{ij} = \begin{bmatrix} -C_1 & 0 & 0 & C_1 \\ 0 & 0 & 0 & 0 \\ 0 & 0 & 0 & 0 \\ C_4 & 0 & 0 & C_4 \end{bmatrix} \quad (C-10)$$

The vector  $g_i(\phi'')$  also comes from the nonlinear term in the governing differential equation and is given by eq 49 as

$$g_i(\phi'') = M_\infty^2 [1 + K''(1 + \gamma)] \int_{\Omega_e} \cos^3 \theta N_i \bigg|_{r=r_e=1} d\theta$$

Substituting the shape functions, eq C-2, into eq 49 and integrating gives

$$g_i(\phi'') = M_\infty^2 [1 + K''(1 + \gamma)] \begin{Bmatrix} g_1 \\ 0 \\ 0 \\ g_4 \end{Bmatrix} \quad (C-11)$$

where

$$g_1 = \frac{-1}{\beta} \left[ (\theta_b - \theta) \left( \frac{\sin 3\theta}{12} + \frac{3\sin \theta}{4} \right) - \frac{\cos 3\theta}{36} - \frac{3\cos \theta}{4} \right] \bigg|_{\theta_a}^{\theta_b}$$

$$g_4 = \frac{-1}{\beta} \left[ (\theta - \theta_a) \left( \frac{\sin 3\theta}{12} + \frac{3\sin \theta}{4} \right) + \frac{\cos 3\theta}{36} + \frac{3\cos \theta}{4} \right] \bigg|_{\theta_a}^{\theta_b}$$

#### Velocity Distribution

The tangential perturbation velocity  $u_\theta(1, \theta)$  is derived in Appendix B for element (2), and is given by eq B-7. For element (3) the velocity is given by the same equation.

$$u_\theta^e(1, \theta) = \frac{1}{\beta} (\phi_4^e - \phi_1^e) \quad (C-12)$$

## Appendix D

### Finite Element Equations for Flow Over an Airfoil for a Bilinear, Rectangular Element

#### Shape Functions

The shape functions for the bilinear rectangular element shown in Fig 46 are given by

$$N_i(\xi, \eta) = \frac{1}{4} (1 + \xi_i \xi) (1 + \eta_i \eta) \quad (D-1)$$

where  $i = 1, \dots, 4$ . Coordinates  $(\xi, \eta)_i$  are the local nodal coordinates of node  $i$ .

#### Elemental Equations

The weak solution of the governing differential equation written in elemental form is expressed by eq 58 as

$$\begin{aligned} & \left[ (1 - M_\infty^2) A_{ij} + B_{ij} - M_\infty^2 \frac{1+\gamma}{2} C_{ij}(\phi^n) \right. \\ & \left. + M_\infty^2 D_{ij} + M_\infty^2 \frac{1+\gamma}{2} E_{ij}(\phi^n) \right] \phi_j^{n+1} = f_i \end{aligned} \quad (D-2)$$

where

$$A_{ij} = \iint_{\Omega_e} N_{i,x} N_{j,x} dx dy$$

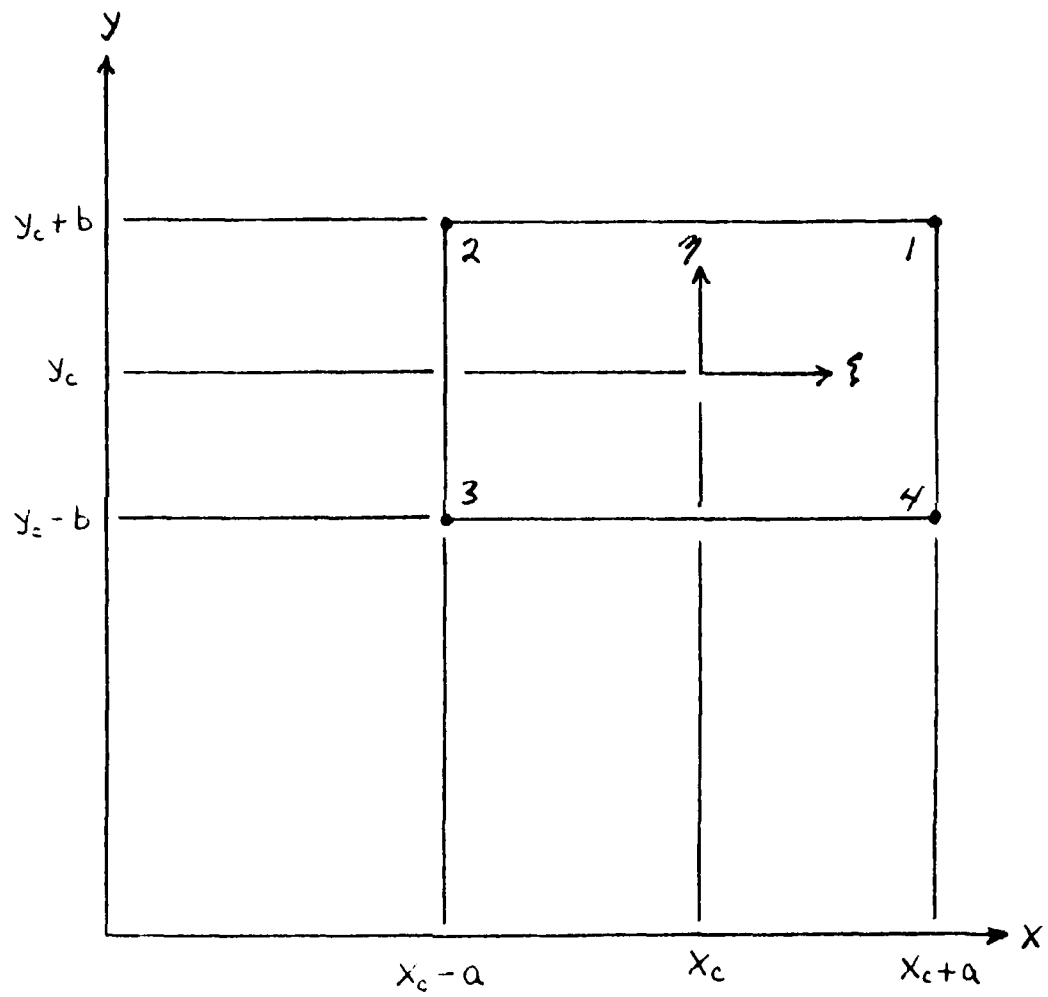


Figure 46 - Rectangular Element

$$B_{ij} = \iint_{\Omega_e} N_{i,y} N_{j,y} dx dy$$

$$C_{ij}(\phi^n) = \phi_K^n \iint_{\Omega_e} N_{K,x} N_{i,x} N_{j,x} dx dy$$

$$D_{ij} = \int_{\partial\Omega_A^*} \frac{df}{dx} N_i N_{j,x} \Big|_{y=0} dx$$

$$E_{ij}(\phi^n) = \phi_K^n \int_{\partial\Omega_A^*} \frac{df}{dx} N_{K,x} N_i N_{j,x} \Big|_{y=0} dx$$

$$f_i = \int_{\partial\Omega_A^*} \frac{df}{dx} N_i \Big|_{y=0} dx$$

The local coordinates  $(\xi, \eta)$  are related to the global coordinates  $(x, y)$  by the transformation equations

$$\xi = \frac{x - x_c}{a} \quad \eta = \frac{y - y_c}{b} \quad (D-3)$$

Using these expressions the elemental equations can be written in local coordinates to give

$$A_{ij} = \frac{b}{a} \int_{-1}^1 \int_{-1}^1 N_{i,\xi} N_{j,\xi} d\xi d\eta$$

$$B_{ij} = \frac{a}{b} \int_{-1}^1 \int_{-1}^1 N_{i,\eta} N_{j,\eta} d\xi d\eta$$

$$C_{ij}(\phi^n) = \frac{b}{a^2} \phi_K^n \int_{-1}^1 \int_{-1}^1 N_{K,\xi} N_{i,\xi} N_{j,\xi} d\xi d\eta$$

$$D_{ij} = \int_{-1}^1 \left. \frac{df}{dx}(\xi) N_i N_{j,\xi} \right|_{\eta=-1} d\xi$$

$$E_{ij}(\phi^n) = \frac{1}{a} \phi_K^n \int_{-1}^1 \left. \frac{df}{dx}(\xi) N_{K,\xi} N_i N_{j,\xi} \right|_{\eta=-1} d\xi$$

$$f_i = a \int_{-1}^1 \left. \frac{df}{dx}(\xi) N_i \right|_{\eta=-1} d\xi$$

The first three matrices are dependent only on the size of the element and are not related directly to any particular airfoil contour. Substituting the shape functions, eq D-1, into these expressions and letting  $i = j = 1$  will produce the following results:

$$A_{ij} = \frac{b}{3a} \begin{bmatrix} 1 & -1 & -1/2 & 1/2 \\ & 1 & 1/2 & -1/2 \\ & & 1 & -1 \\ & & & 1 \end{bmatrix}$$

$$B_{ij} = \frac{a}{3b} \begin{bmatrix} 1 & 1/2 & -1/2 & -1 \\ & 1 & -1 & -1/2 \\ & & 1 & 1/2 \\ & & & 1 \end{bmatrix}$$

$$C_{ij}(\phi^n) = \begin{bmatrix} A & -A & -B & B \\ & A & B & -B \\ & & C & -C \\ & & & C \end{bmatrix}$$

where

$$A = \frac{b}{8a^2} \left[ \phi_1^n - \phi_2^n + \frac{1}{3}(\phi_4^n - \phi_3^n) \right]$$

$$B = \frac{b}{24a^2} \left[ \phi_1^n - \phi_2^n + \phi_4^n - \phi_3^n \right]$$

$$C = \frac{b}{8a^2} \left[ \frac{1}{3}(\phi_1 - \phi_2) + \phi_4 - \phi_3 \right]$$



Matrices  $D_{ij}$  and  $E_{ij}$  and vector  $f_i$  are directly dependent upon the airfoil contour being considered. These quantities are evaluated only for elements that share a common boundary with the contour. Thus for most elements in the domain these quantities are zero.

Symmetric Flow. Consider a parabolic-arc airfoil with thickness distribution given by

$$y = f(x) = \tau(1 - 4x^2) \quad ; \quad |x| \leq 1/2 \quad (D-4)$$

For this airfoil the remaining quantities in eq D-2 become

$$D_{ij} = 8\tau \begin{bmatrix} 0 & 0 & 0 & 0 \\ 0 & 0 & 0 & 0 \\ 0 & 0 & E & -E \\ 0 & 0 & F & -F \end{bmatrix}$$

$$E_{ij} = 8\tau \begin{bmatrix} 0 & 0 & 0 & 0 \\ 0 & 0 & 0 & 0 \\ 0 & 0 & G & -G \\ 0 & 0 & H & -H \end{bmatrix}$$

$$f_i = 8\tau \begin{Bmatrix} 0 \\ 0 \\ 2E \\ 2F \end{Bmatrix}$$

where

$$E = \frac{a}{2} \left[ \frac{x_c}{a} - \frac{1}{3} \right]$$

$$F = \frac{a}{2} \left[ \frac{x_c}{a} + \frac{1}{3} \right]$$

$$G = \frac{1}{4} \left[ (\phi_4 - \phi_3) \left( \frac{x_c}{a} - \frac{1}{3} \right) \right]$$

$$H = \frac{1}{4} \left[ (\phi_4 - \phi_3) \left( \frac{x_c}{a} + \frac{1}{3} \right) \right]$$

### Pressure Distribution

For steady small disturbance theory the coefficient of pressure is given by

$$C_p = -2u$$

The velocity in element  $e$  is calculated from the assumed solution for the potential given by eq 57

$$\phi^e(x, y) = N_j(x, y) \phi_j^e \quad (57)$$

From thin airfoil theory the pressure coefficient is evaluated along  $y = 0^+$ . Thus for element  $e$  which borders the airfoil contour the elemental pressure coefficient becomes

$$C_p^e(x, y = 0^+) = -2 \phi_{,x}^e(x, y = 0^+)$$

Using the transformation equations between the  $(x, y)$  and  $(\xi, \eta)$  coordinates, given by eq D-3, and substituting eq 57 gives

$$C_p^e(x, y = 0^+) = \frac{-2}{a} N_{j,\xi}(\xi, \eta = -1) \phi_j^e$$

or

$$C_p^e(x, y = 0^+) = \frac{-1}{2a} (\phi_4^e - \phi_3^e) \quad (D-5)$$

Within element  $e$  the pressure is a constant value which means there are "jumps" in pressure between elements along the airfoil surface. This implies that the pressure distribution along  $y = 0^+$  is a step function. For most of the distributions of the pressure coefficient given in

Chapter VI the value of pressure coefficient computed from eq D-5 is plotted at the midpoint of the element.

### Mach Number

The local Mach number is defined by  $M = v/a_s$  where  $a_s$  is the local speed of sound given by

$$\left(\frac{a_s}{v_\infty}\right)^2 = \frac{\gamma-1}{2} \left[1 - \left(\frac{v}{v_\infty}\right)^2\right]$$

The Mach number becomes

$$M^2 = \frac{\left(\frac{v}{v_\infty}\right)^2}{\frac{\gamma-1}{2} \left[1 - \left(\frac{v}{v_\infty}\right)^2\right] + \frac{1}{M_\infty^2}} \quad (D-6)$$

The velocity  $\vec{v}$  is given by  $\vec{v} = (1+u, v)$ . In element  $e$

$$(v/v_\infty)^2 = (1 + \phi_x)^2 + (\phi_y)^2$$

Transforming to local coordinates  $(\xi, \eta)$  gives

$$\begin{aligned} (v/v_\infty)^2 = & \left[1 + \frac{1}{4a} \left\{ (1+\eta)(\phi_1^e - \phi_2^e) + (1-\eta)(\phi_4^e - \phi_3^e) \right\}\right]^2 \\ & + \left[ \frac{1}{4b} \left\{ (1+\xi)(\phi_1^e - \phi_4^e) + (1-\xi)(\phi_2^e - \phi_3^e) \right\} \right]^2 \end{aligned}$$

Substituting this expression into eq D-6 will define the Mach number in element  $e$ . For the bilinear element Mach number will be discontinuous across inter-element boundaries.

### Vita

James E. Marsh was born on 5 February 1943 at Red Star, W. Va. He graduated with honors from Man High School, Man, W. Va., in 1961 and enlisted in the United States Air Force. While stationed in Texas, Alaska, and Mississippi he attended night classes at San Antonio College, Alaska University, and the University of Southern Mississippi, respectively. In June of 1967 he was chosen to attend Oklahoma State University through the Airman Education and Commissioning Program. In January 1970 he graduated with a B.S. in Mechanical Engineering. In May 1970 he was commissioned as a 2nd Lieutenant in the United States Air Force and was assigned to the Air Force Institute of Technology (AFIT) to pursue a graduate degree in Aero-mechanical Engineering. In October 1971 he completed the requirements for a M.S. degree and was assigned to the Air Force Flight Dynamics Laboratory. For nearly four years he served as a senior project engineer in the Vibrations Group, of the Vehicle Dynamics Division. During this time he received two Outstanding Scientific Achievement Awards for his work in aircraft vibration prediction methods. In June 1975 he returned to AFIT to pursue a doctorate in Aerospace Engineering. He is currently assigned to the Aeronautics and Astronautics Department, School of Engineering, Air Force Institute of Technology as a member of the faculty.

Permanent Address:

General Delivery  
Earling, W. Va.

**DATE**  
**ILME**